

Sinusoidal Noise Reduction from Eddy Current Data of  
Steam Generator Tubes Using Iterative Weighted  
Multipoint Interpolated DFT (WMIpDFT) Approach

By

Reza Kazemi Kamyab

A thesis submitted to the Faculty of Graduate and Postdoctoral  
Affairs in partial fulfillment of the requirements for the degree of

Master of Applied Science

in

Electrical and Computer Engineering

Carleton University  
Ottawa, Ontario

© 2016, Reza Kazemi Kamyab

## **Abstract**

Eddy current testing is a non-destructive technique, which is widely utilized to detect and monitor degradation and flaws such as cracks in the steam generator tubes located in nuclear power plants. Typically, the analysis of eddy current testing data of steam generator tubes is complex due to the presence of noise sources in the data. These noise sources decrease the signal to noise ratio, and therefore, the detection of flaw signals becomes a difficult task. A signal processing technique has been proposed in this study, which utilizes the Weighted Multipoint Interpolated Discrete Fourier Transform algorithm iteratively, to reduce low frequency sinusoidal noise as a noise source. The performance of the proposed algorithm was assessed based on the noise level, and the flaw signal power. It has been shown that the algorithm effectively estimates the parameters of sinusoidal noise, and improves the signal to noise ratio of the flaw signals.

## **Acknowledgements**

I would like to express my appreciations to all the people who helped me to finish this research to fruition.

First, I would like to thank Professor Mohamed El-Tanany for all the support, guidance, and valuable instructions he has provided me throughout my research. I do not have enough words to express my deep and sincere gratitude. I would also like to thank the department of Systems and Computer Engineering and its staff at Carleton University for giving me the opportunity of taking part in the Master of Applied Science program and helping me throughout my research.

Furthermore, I would like to thank Mr. Vijay Babbar and Mr. Richard Lakhan from Canada Nuclear Laboratories (CNL) for providing me with all the technical knowledge and documents about the test setup, data collection, and analysis of the data. They were also extremely patient and generous with their time meeting with me and answering all my questions. Moreover, I would like to thank Canada Nuclear Laboratories (CNL) for giving me all the necessary data and documents to work with for this research, and for supporting me financially.

I would also like to thank the graduate students, especially the former colleague, Hossein Chahrour, for helping me at the start of this project by sharing their technical knowledge and answering all my questions patiently.

Finally, I would also like to thank my family for providing me with unconditional support and continuous encouragement throughout my studies. The accomplishment of this research would not have been possible without them.

# Table of Contents

<b>Abstract.....</b>	<b>ii</b>
<b>Acknowledgements .....</b>	<b>iii</b>
<b>Table of Contents .....</b>	<b>iv</b>
<b>List of Tables .....</b>	<b>viii</b>
<b>List of Figures.....</b>	<b>xi</b>
<b>List of Appendices.....</b>	<b>xiv</b>
<b>List of Symbols .....</b>	<b>xv</b>
<b>List of Acronyms .....</b>	<b>xviii</b>
<b>Chapter 1: Introduction .....</b>	<b>1</b>
1.1 Problem Statement .....	3
1.2 Overview of Results.....	4
1.3 Contribution of the Thesis.....	5
1.4 Organization of the Thesis .....	5
<b>Chapter 2: Background Information .....</b>	<b>7</b>
2.1 Steam Generators in Nuclear Plants.....	7
2.2 Non-destructive Techniques.....	10
2.3 Eddy Current Testing .....	11
2.3.1 Principles of Eddy Current Testing.....	12
2.3.2 Eddy Current Testing Instrument.....	16
2.3.3 Variables Effecting Eddy Current Testing.....	17
2.3.3.1 Conductivity and Magnetic Permeability .....	17
2.3.3.2 Lift-off.....	18
2.3.3.3 Excitation Frequency.....	18

2.3.3.4	Probes .....	19
2.3.3.4.1	Probe Configuration .....	20
2.3.3.4.2	Operation Mode .....	20
2.3.3.5	Types of Eddy Current Testing .....	21
2.3.3.5.1	Conventional Eddy Current Testing.....	21
2.3.3.5.2	Multi-frequency Eddy Current Testing.....	21
2.3.3.5.3	Pulsed Eddy Current (PEC).....	22
2.4	Eddy Current Testing Procedure for Steam Generator Tubes.....	22
2.5	Noise Sources for ECT in SG Tubes.....	24
2.5.1	Common Sources of Noise .....	24
2.5.2	Types of Noise .....	24
2.5.3	Low Frequency Sinusoidal Noise .....	25
<b>Chapter 3: Literature Review .....</b>		<b>26</b>
3.1	Signal Processing Noise Reduction Techniques .....	27
3.2	Cyclic-Music Algorithm .....	29
<b>Chapter 4: Weighted Multipoint Interpolated DFT (WMIpDFT) Technique.....</b>		<b>32</b>
4.1	Theoretical Background .....	33
4.2	Signal Parameter Estimation using WMIpDFT .....	37
4.2.1	Frequency Estimation .....	37
4.2.2	Amplitude Estimation .....	38
4.2.3	Phase Estimation.....	38
4.3	WMIpDFT Performance Factors .....	39
4.3.1	Frequency and Systematic Errors .....	39
4.3.2	Combined Standard Uncertainty for Normalized Frequency Estimator .....	40
4.3.3	Statistical Efficiency of WMIpDFT.....	40
4.3.4	Choice of the Number of Interpolation Points and Window Order (H).....	41

4.3.4.1	Number of Interpolation Points .....	41
4.3.4.2	Window Order (H) .....	42
<b>Chapter 5:</b>	<b>Proposed Iterative WMIpDFT Algorithm .....</b>	<b>43</b>
5.1	Iterative Approach for Signal Parameter Estimation .....	44
5.2	Minimization to Improve Amplitude and Phase Estimations .....	46
<b>Chapter 6:</b>	<b>Implementation and Results.....</b>	<b>48</b>
6.1	Preprocessing of Collected ECT Data.....	49
6.1.1	Background Noise Reduction .....	49
6.1.2	High Frequency Noise Reduction.....	51
6.1.3	ECT Data Segmentation .....	52
6.2	Implementation of the Proposed Algorithm.....	54
6.2.1	Regions of Interest for Implementation of the Algorithm .....	54
6.2.2	Value Selection for the Parameters of the Algorithm .....	55
6.2.2.1	Variable J for Number of Interpolation Points .....	55
6.2.2.2	Window Order H.....	57
6.2.3	Iteration Effect of Proposed Algorithm on Frequency estimation.....	58
6.3	The Proposed Algorithm's Estimation Results from Simulation.....	59
6.4	The Proposed Algorithm's Results on Free Span Regions .....	61
6.4.1	Estimated Parameters of Sinusoidal Noise .....	61
6.4.2	Peak Removal to Improve Estimation .....	63
6.4.3	Root Mean Square (RMS) Improvement.....	65
6.4.4	Peak To Average Ratio (PAR) Comparison .....	66
6.4.5	Minimization Effect.....	68
6.4.5.1	Using Each Segment's Estimated Sinusoidal Frequencies.....	68
6.4.5.2	Using Similar Estimated Sinusoidal Frequencies for Each Region.....	69
6.4.5.2.1	Segment with Lowest Root Mean Square (RMS) in Each Region .....	69

6.4.5.2.2	Average of Frequencies in Each Region .....	71
6.5	Analysis of Estimated Sinusoidal Noise Reduction on Inserted Flaw Signals .....	72
6.5.1	Analysis of Inserted Flaws in Time Domain .....	73
6.5.2	Analysis of Inserted Flaws in Impedance Plane .....	77
6.6	Comparison with Cyclic-MUSIC Algorithm .....	86
<b>Chapter 7:</b>	<b>Conclusion and Future Work.....</b>	<b>89</b>
7.1	Conclusion.....	89
7.2	Future Work .....	91
Appendix A	.....	93
A.1	Estimated Sinusoidal Noise Parameters of Other Tubes.....	93
<b>Bibliography</b>	<b>.....</b>	<b>97</b>

## List of Tables

Table 6.1 RMS of free span segments in Tube 1 after subtraction of estimated noise signal of 3 sinusoids for H=2 and different values of J. Column 3 shows lower RMS values. ....	56
Table 6.2 RMS of free span segments after subtraction of estimated noise signal of 3 sinusoids for J=1 (i.e. 3 Interpolation Points) and different values of H. Column 3 shows lower RMS values. ....	57
Table 6.3 Comparison of Performance of Iterative and Non-Iterative WMIpDFT Approaches on ECT Data (Frequencies are sorted based on amplitude).....	59
Table 6.4 Estimated parameters of the inserted sinusoids in Equation 6.4 in all FS segments.....	60
Table 6.5 4 sinusoidal components of the noise signal in the free span region of 1000 points with the highest amplitudes in the frequency domain. The table is sorted based on the amplitude.....	62
Table 6.6 2 Estimated sinusoidal components of the noise signal, which are similar mostly among all the segments in Tube 1.....	63
Table 6.7 Parameter estimation of segments in Tube 1 after removal of flaw signal.....	64
Table 6.8 The root mean square (RMS) of each segment in Tube 1 after applying the Iterative WMIpDFT algorithm. This can be seen in Column 4.....	65
Table 6.9 Peak-to-Average ratio (PAR) of the non-flaw & potential flaw peaks in Segments 2 & 17 in Tube 1.....	67

Table 6.10 Peak-to-average ratio (PAR) when 2 and 3 sinusoids used to filter Tube 1 data .....	67
Table 6.11 RMS results for all the segments in Tube 1 before and after the reduction of noise signal of 2 sinusoids as well as after minimization with their improvements with respect to original RMS in percentage. Lower RMS values shown in Column 6 due to minimization. ....	68
Table 6.12 RMS results for the cold region before and after the reduction of noise signal of 2 sinusoids as well as after minimization, using Segment 3's estimated frequencies, with their improvements with respect to original RMS in percentage .....	70
Table 6.13 RMS results for the hot region before and after the reduction of noise signal of 2 sinusoids as well as after minimization, using Segment 15's estimated frequencies, with their improvements (reductions) with respect to original RMS in percentage. ....	71
Table 6.14 RMS before and after sinusoidal noise reduction after averaging estimated frequencies for each region.....	72
Table 6.15 RMS results before and after the reduction of noise signal of 2 sinusoids with minimization from segments containing inserted flaws in both horizontal and vertical components .....	76
Table 6.16 RMS and PAR results before and after the reduction of noise signal of 2 sinusoids with minimization from segments containing inserted flaws in both horizontal and vertical components .....	77
Table 6.17 Frequency component comparison of the two sinusoidal estimation technique in case of non-periodic peaks. It can be seen that the proposed algorithm estimate	

<p>frequencies such as 21.9 and 7.51 that have been similarly observed in other segments  without removing peak in the segment .....</p>	87
<p>Table 6.18 RMS comparison of Cyclic-MUSIC and Iterative WMIpDFT algorithms. The  proposed algorithm in Column 4 shows lower RMS values based on estimated noise of 4  sinusoids.....</p>	88

## List of Figures

Figure 2.1 A nuclear power plant with a steam generator (copied from [4] with written permission).....	7
Figure 2.2 Nuclear plant steam generator with U-shaped tubes (copied from [4] with written permission) .....	9
Figure 2.3 Eddy current testing principle .....	13
Figure 2.4 Flaws, represented by red arrows, in normalized impedance plane .....	14
Figure 2.5 Flaw signals in Ferromagnetic and non-ferromagnetic materials plotted in impedance plane.....	15
Figure 2.6 Block diagram of the eddy current testing (ECT) instrument .....	16
Figure 2.7 Probe insertion in tube to collect data for inspection .....	23
Figure 3.1 TSP response at Frequencies 120 and 240 KHz, which can be used to reduce the support plate response by subtracting one from another, by means of mixing frequency techniques. ....	26
Figure 4.1 3-term maximum side-lobe decay window in time domain (top plot) and its .....	35
Figure 5.1 Flow chart of the proposed iterative WMIpDFT Algorithm where the pre-processed data sequence is fed into the WMIpDFT in an iterative manner until the desired number of sinusoids is estimated. The results are then fed into the minimization algorithm for further parameter optimization.....	44

Figure 5.2 Block diagram of the iterative approach adopted by the proposed Iterative WMIpDFT Algorithm. Indexes $j$ and $k$ are set to 0 and 1 respectively, and the initial value of the residual signal sequence (i.e. $R_0$ ) is $x(n)$ .....	45
Figure 5.3 The flow chart of the minimization algorithm for improvement of estimated phase and amplitude parameters for each frequency component of estimated sinusoidal noise through minimization of the ECT data sequence and estimated sinusoidal noise. .	47
Figure 6.1 The preprocessing stages of the collected ECT data .....	49
Figure 6.2: Horizontal Component of impedance plane before (top plot) and after (bottom plot) removal of background and high frequency noise from Tube 1 .....	50
Figure 6.3 Vertical Component of impedance plane before (top plot) and after (bottom plot) removal of background and high frequency noise from Tube 1 .....	50
Figure 6.4 The high frequency noise riding on the vertical component (top plot) and the vertical component without the high frequency (bottom plot) from Tube 1 .....	51
Figure 6.5 Tubes inside a steam generator with free span and TSP regions indicated adapted from [2] with written permission.....	53
Figure 6.6 Flaw signals from ECT data with outer diameter flaw labeled as OD and inner diameter flaw labeled as ID along with other flaws such hole .....	55
Figure 6.7 Iteration approach of the proposed Iterative WMIpDFT algorithm.....	58
Figure 6.8 The top plot shows the peak removal of Segment 2 along with the original signal, and the bottom plot shows the same for Segment 17 in Tube 1.....	64
Figure 6.9 Potential flaw and non-flaw peaks for Segments 2 and 17 in Tube 1 .....	66
Figure 6.10 Inserted 40% outer diameter (OD) Flaws at different free span (FS) segments in Tube 1 .....	74

Figure 6.11 Estimated sinusoidal noise along with the unfiltered signal for Vertical Component of Segment 3.....	75
Figure 6.12 Estimated sinusoidal noise along with the unfiltered signal for Horizontal Component of Segment 3.....	75
Figure 6.13 40% OD flaw in impedance plane that has been inserted into different segments of the Tube 1 .....	78
Figure 6.14 The inserted flaw in Segment 3 (top) and Segment 9 (bottom) along with the original flaw before insertion.....	79
Figure 6.15 Plots of Impedance plane of Segments 3 and 9 before and after applying the proposed sinusoidal noise reduction algorithm.....	80
Figure 6.16 Horizontal Stretch in Segment 9 which introduces distortion in the flaw.....	81
Figure 6.17 Plot of Impedance plane of Segments 18 before (in blue) and after (in red) applying the proposed sinusoidal noise reduction algorithm.....	82
Figure 6.18 Phase of vertical and horizontal components of Segment 18.....	83
Figure 6.19 The impedance plane of Segment 8 after insertion the flaw in blue, and after phase inversion in red .....	84
Figure 6.20 Impedance plane of the inserted flaw in Segment 3 after phase inversion ...	84
Figure 6.21 The phase of two components after sinusoidal noise reduction for Seg18 ...	85

## List of Appendices

Appendix A.....	92
A.1 Estimated Sinusoidal Noise Parameters of Other Tubes.....	92

## List of Symbols

$\Phi_B$  – Magnetic Flux

$\mathcal{E}$  – Induced voltage

$B$  – Magnetic field

$Z$  – Coil impedance

$R$  – Resistance of the coil impedance

$X_L$  – Reactance of the coil impedance

$\omega$  – Angular Frequency

$R_C$  – Current Resistance

$X_C$  – Current Inductance of the coil

$R_{C+Flaw}$  –Resistance of the coil when a flaw is present

$X_{C+Flaw}$  –Inductance of the coil when a flaw is present

$f_e$  – Excitation frequency

$\mu_0$  – Permeability of free space

$\mu_r$  – Relative permeability of material under test

$\sigma$  – Conductivity of material under test

$P_{XX}^{MUSIC}(f)$  – MUSIC spectrum estimate

$s(f)$  – Complex sinusoidal vector

$V(f)$  – Noise subspace matrix

$k$  – Index of sinusoidal component

$K$  – Number of sinusoidal components

$M$  – Data sequence length

$A_k$  – Amplitude of  $k$ th sinusoidal component  
 $f_k$  – Frequency of  $k$ th sinusoidal component  
 $\varphi_k$  – Phase of  $k$ th sinusoidal component  
 $\lambda_k$  – Number of recorded sine-wave cycles  
 $l_k$  – Integer part of  $\lambda_k$   
 $\delta_k$  – Fractional part of  $\lambda_k$   
 $\alpha_k$  – Ratio used to calculate  $\delta_k$   
 $f_r$  – Resolution frequency  
 $f_s$  – Sampling frequency  
 $m$  – Sample index  
 $x(m)$  – Sampled signal value at time  $m$   
 $w(m)$  – Window signal value at time  $m$   
 $x_w(m)$  – Windowed sample value signal at time  $m$   
 $W(\lambda)$  – Discrete Fourier transform of Window function  
 $H$  – window order for maximum side-lobe decay windows, known as Rife-Vincent windows  
 $J$  – Number of interpolation points  
 $\Delta(l_k)$  – Bias term due to long-term leakage of the spectral image of  $k$ th component  
 $a_h$  – Window coefficients  
 $\sigma^2$  – Variance of white Gaussian noise  
 $\hat{\delta}_H$  – Combined uncertainty of WMIPDFT normalized frequency estimator  
 $ar(\hat{\delta}_k)_{CR}$  – Cramér–Rao (CR) lower bound for frequency  
 $D$  – Number of estimated sinusoidal components

$x(n)$  – Sampled ECT data value at time  $n$  where  $n$  is the sample index

$N$  – Number of ECT data samples

$S_k$  –  $k$ th component of the sinusoidal noise signal obtained from estimated sinusoidal parameters using WMIpDFT algorithm

$j$  – Iteration index

$R_j$  – Residual data sequence obtained from subtracting ECT data sequence from estimated sinusoidal noise signal

$T$  – Signal sampling period

## List of Acronyms

<b>AECL</b>	Atomic Energy Canada Limited
<b>CANDU</b>	CANada Deuterium Uranium
<b>CNL</b>	Canada Nuclear Laboratories
<b>DFT</b>	discrete Fourier transform
<b>DWT</b>	discrete wavelet transform
<b>FFT</b>	fast Fourier transform
<b>FS</b>	free span
<b>ECT</b>	eddy current testing
<b>ID</b>	inside diameter
<b>IpDFT</b>	interpolated DFT
<b>NDT</b>	non-destructive testing
<b>OD</b>	outside diameter
<b>PAR</b>	peak to average ratio
<b>PEC</b>	pulsed eddy current
<b>PWR</b>	pressurized water reactor
<b>RMS</b>	root mean square
<b>SG</b>	steam generator
<b>SNR</b>	signal to noise ratio
<b>TSP</b>	tube support plate
<b>WMIpDFT</b>	Weighted Multipoint Interpolated DFT

## Chapter 1: Introduction

In many industries such as construction, aerospace, petroleum and nuclear, testing plays an important role in verifying and ensuring the integrity of the structures in use. Testing prevents malfunctions, which could potentially lead to disastrous catastrophes. Nuclear power plants such as pressurized water reactors (PWR), which are designed to produce power, are no exceptions to extensive testing.

In a pressurized water reactor, the primary coolant, typically water, which is heated by the reactor core, is transferred to a steam generator where it travels through a large number of tubes. This flow of heated water, in turn, evaporates a secondary coolant located in the steam generator (SG) to pressurize steam. The generated steam can then be used to spin turbines to produce electricity. The tubes transferring the heat from the primary coolant system in the SG endure harsh conditions such as high temperatures and pressure. This can make them susceptible to physical degradation flaws<sup>1</sup> such as wear, cracks, and denting. Therefore, extensive testing must be performed on the tubes to assess and characterize the potential flaws and to safeguard their integrity.

In the nuclear industry, Canada Nuclear Laboratories (CNL)<sup>2</sup> is a leading nuclear technology company in designing and developing technology applications for CANDU (CANada Deuterium Uranium) pressurized water reactors. One of the areas they have been conducting research is non-destructive testing (NDT) methods<sup>3</sup>, such as eddy current testing (ECT), to ensure the integrity and safety of the structures (e.g., SG tubes)

---

<sup>1</sup> Flaw signal is any kind of irregularity on the test material that could potentially cause malfunction, service disruption, and environmental damage in the nuclear industry context.

<sup>2</sup> Canada Nuclear Laboratories (CNL) is formerly known as Atomic Energy Canada Limited (AECL).

<sup>3</sup> NDT methods are analysis techniques to evaluate and inspect the properties of materials, components or systems in science and industry without causing damage.

inside nuclear reactors [1-2]. This project is a continuation of the research by CNL, with the aim of advanced signal processing of collected ECT data for assessment of potential flaws and system condition monitoring [3].

The collected ECT data from the SG tubes contain sources of noise<sup>4</sup>, which hinder the identification and characterization of defects in the SG tubes, and potentially lead to undetected flaws or false positives. The noise sources could be introduced in the ECT data by vibration of test probe<sup>5</sup>, unevenness of tube surface, tube support structures, corrosion products, changes in tube dimensions and geometry, and other sources. These flaws could result in unforeseeable consequences such as environmental disasters or interruption in the operation of the nuclear power plants.

The research in [3], which had been completed prior to this project, focused on developing an algorithm to estimate and reduce low-frequency sinusoidal noise as a noise source contained in the ECT data provided by CNL in order to improve SNR<sup>6</sup>. In this project, another signal processing algorithm has been developed to improve the estimation of the same noise source as in [3] from the same set of ECT data provided by CNL.

The ECT data from a set of SG tubes as well as all the technical information on the ECT operation, data collection, and analysis of data have been provided by CNL. Moreover, the CNL team has offered advice and insight on the analysis of the results obtained in this project.

---

<sup>4</sup> Noise in this research is considered any distortion that hinders the flaw signals of interest.

<sup>5</sup> Test probe contains a coil that is used to navigate over the test surface to detect irregularities such as flaw signals.

<sup>6</sup> Signal to Noise ratio is the ratio of flaw signal strength over the background noise power ratio of finite data length.

## 1.1 Problem Statement

Eddy Current Testing is used widely for in-service inspection of the steam generator (SG) tubes at pressured water reactors to ensure the tubes are free of any defects. However, ECT data has sources of noise that make it difficult for operators to detect and characterize potential flaws in the steam generator tubes. Therefore, it is of high importance to accurately estimate noise sources using signal-processing techniques to improve the detection of flaws as well as to minimize the effect of distortion on the flaw features and characteristics.

One of the noise sources whose removal could potentially lead to detection improvement of steam generator tube flaws is low-frequency sinusoidal noise. Vibration of the testing equipment, probe wobbling, and variation in the tube's surface could be some of the causes of the low-frequency sinusoidal noise.

There have been many proposed signal-processing techniques to reduce noise sources such as lift-off<sup>7</sup> noise, tube support plates (TSP) holding the tubes, and random noise<sup>8</sup>. However, the estimation and reduction of low frequency sinusoidal noise from eddy current testing data of steam generator tubes has not been addressed extensively in the literature.

The short-term objective of this research is to accurately estimate low-frequency noise from the ECT data and consequently reduce the noise from the data in order to enhance the probability of detection of flaws with weak response signals. Moreover, the long-term objective of the CNL project is to design a fully automatic system to detect,

---

<sup>7</sup> Lift-off is impedance changes when there is variation in the distance between the testing coil and the test piece.

<sup>8</sup> Random noise is a noise source that has unpredictable spatial, and frequency distribution.

characterize and classify defects in order to cut costs and analysis time, and improve reliability.

## 1.2 Overview of Results

The proposed algorithm, Iterative Weighted Multipoint Interpolated DFT (WMIpDFT), has been applied to the regions between the TSPs, called free span (FS) regions, to estimate the low-frequency sinusoidal noise and remove it from the collected ECT data.

When the proposed algorithm was applied to the collected ECT data, the results showed that in the time domain for both horizontal and vertical components, the algorithm improved the RMS<sup>9</sup> values by at least 30% with the reduction of noise of two or more sinusoids with highest amplitudes. Moreover, the results showed that flaw signal power in terms of the PAR<sup>10</sup> improved by at least 2% when the estimated sinusoidal noise was reduced.

Additionally, in the impedance plane, the algorithm reduced the horizontal stretch noise, which is mostly caused by lift-off or the presence of magnetite. However, no conclusion in terms of characterization and categorization can be drawn from the effect of applying the algorithm to the flaws in the impedance plane. This is because the changes such as shape<sup>11</sup>, phase, and magnitude in the flaws after applying the algorithm in the impedance plane need to be assessed using techniques including image processing. Therefore, further investigation needs to be performed.

Finally, the proposed algorithm has been compared with another similar algorithm, Cyclic-Music algorithm, which estimates the sinusoidal noise from the ECT

---

<sup>9</sup> RMS (root mean square) is calculated by the square root of the sum of all magnitudes over the length of finite set of data.

<sup>10</sup> PAR (peak to average ratio) is the ratio of the peak magnitude over the RMS value of the data of interest in decibel (dB).

<sup>11</sup> The shape of the flaw is the coil impedance changes which have been plotted in the impedance plane.

data. Results showed that the proposed algorithm can lead to lower RMS values for the FS regions, and performs better in terms of frequency estimation in the presence of flaw peaks.

### **1.3 Contribution of the Thesis**

The contribution of the thesis can be summarized in the following aspects:

- An algorithm was developed to estimate the sinusoidal parameters of the low-frequency noise in the ECT data obtained from the CANDU SG tubes.
- Detection of potential flaws from ECT data was investigated in the time-domain in terms of the RMS and PAR values using the proposed algorithm.
- The proposed algorithm was compared with the existing algorithms for estimation of sinusoidal noise in ECT data.
- Outside diameter (OD) Flaws were inserted into the ECT data, and the effect of the proposed algorithm on the inserted flaws was analyzed in both the time domain and impedance plane.

### **1.4 Organization of the Thesis**

Chapter 1 is an extended summary of the thesis. It defines one of the problems with the collected data from the steam generator tubes by means of eddy current testing, and furthermore, proposes a solution. In addition, it briefly presents the overview of the results as well as the summary of the contributions.

The rest of this thesis is organized as follows:

Chapter 2 presents the background information about the structure of a typical pressurized water reactor, and its components. It describes the testing techniques used in the industry for inspecting SG tubes located in pressurized water reactors, and focuses on

the widely used eddy current testing method. Moreover, it explores the factors affecting the eddy currents.

Chapter 3 provides a review of the literature on the proposed signal processing techniques for minimizing noise signals, and enhancing the flaw signals in the steam generator tubes. Moreover, it discusses the Cyclic-Music algorithm in [3], which estimates and reduces sinusoidal noise from the ECT data for the steam generator tubes.

In Chapter 4, the estimation of sinusoidal parameters using the WMIpDFT technique is discussed. The factors involved in improving parameter estimation in WMIpDFT are also explored.

In chapter 5, the proposed algorithm, Iterative WMIpDFT, is discussed. It explains the components of the algorithm such as the iterative approach and minimization, and how they are derived.

In chapter 6, the steps taken to apply the algorithm to the ECT data collected from the steam generator tubes at a CANDU pressurized water reactor are presented. Additionally, the results of applying the proposed algorithm to the same set of data with the inserted flaws are also presented. Consequently, the results are analyzed in the time domain as well as impedance plane. Moreover, the results obtained from the proposed algorithm are discussed and compared with the results of a similar algorithm (Cyclic-Music algorithm) [3], which estimates the low-frequency sinusoidal noise.

In chapter 7, a conclusion is provided, and suggestions for future research are presented.

## Chapter 2: Background Information

This chapter describes the background information on steam generators located in CANDU pressurized water reactors, which make up a majority of nuclear power plants. Moreover, it discusses different nondestructive testing methods that are used to evaluate the properties of the tubes inside the steam generators. Additionally, the chapter focuses on eddy current testing, which is widely utilized in the industry for testing the integrity of steam generators' tubes. It also explains the principle of eddy current testing, and factors affecting the collected ECT data.

### 2.1 Steam Generators in Nuclear Plants

Steam generators, used in CANDU reactors, are heat exchanger units, which convert water into steam from the heat produced at the nuclear reactor core as shown in Figure 2.1.

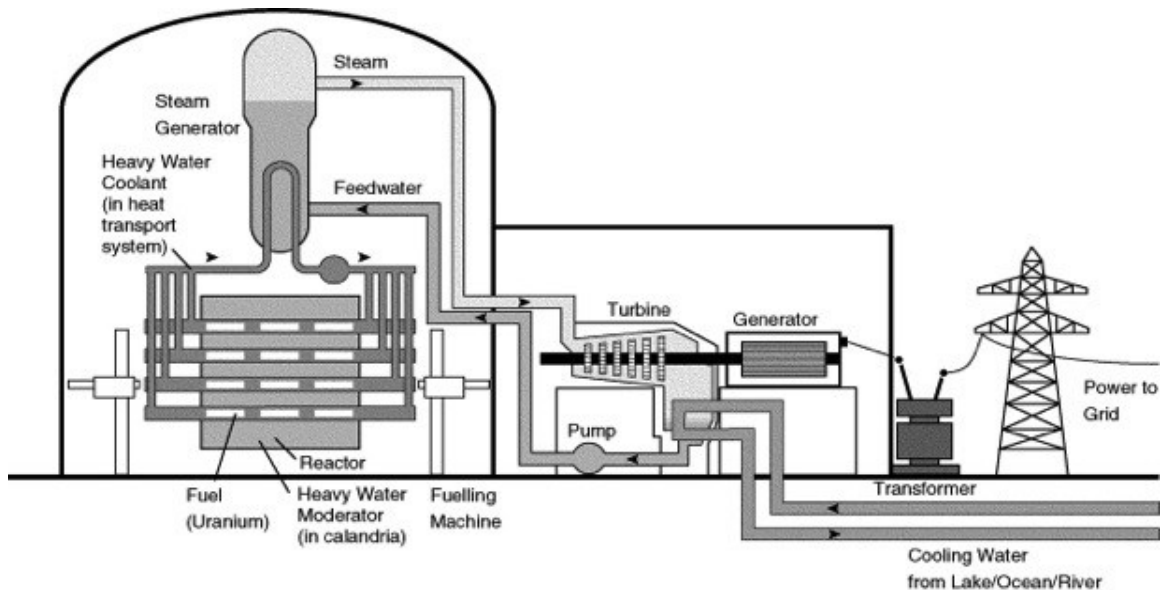


**Figure 2.1:** A nuclear power plant with a steam generator (copied from [4] with written permission)

As shown in Figure 2.1, the heated heavy water coolant from the reactor core is pumped into the steam generator (SG) through the SG tubes, which vaporizes the secondary coolant flowing around the tubes in the steam generators. The produced steam subsequently spins turbine generators to produce electricity. The steam is later condensed through cooling water, and pumped back into the steam generator to be heated again by the heat from the reactor [4].

CANDU nuclear power plants typically have two to twelve steam generators, and each steam generator contains from 2,600 to 4,800 U-shaped tubes of 15-20 mm in diameter, and 12-15 meters in length. Depending on the design and age of the nuclear power plants, there are a variety of SG tubing materials including nickel-based materials such as Alloy 400, Alloy 600 and Alloy 800, which are utilized due to their thermal conductivity, high formability and corrosion resistance, and mechanical strength [2, 5, 6]. The steam generator U-shaped tubes are bundled together at the bottom by the tube sheet, and at intervals by the TSPs as shown in Figure 2.2.

The tubes are the pressure barriers between the radioactive and non-radioactive parts of a pressurized water reactor. Consequently, the tubes are constantly exposed to harsh environmental conditions such as high temperatures, high pressures, high fluid flow rates and material interactions resulting in various types of tube degradations fretting wear<sup>12</sup>, stress corrosion cracking (SCC)<sup>13</sup>, pitting<sup>14</sup>, volumetric degradation, Intergranular corrosion, and denting [2], [7]. Therefore, it is vital that the tubes are well maintained, and free of any major defects for the integrity of the steam generators, and to

---

<sup>12</sup> Fretting wear is caused by the contact between two surfaces experiencing vibration.

<sup>13</sup> Corrosion cracking is a formation of crack induced by in tensile stress in a corrosive environment.

<sup>14</sup> Pitting is an extreme form of corrosion that leads to creation of holes in materials.

prevent any interruptions or malfunctions that could potentially cause radioactive and toxic leaks into the environment.

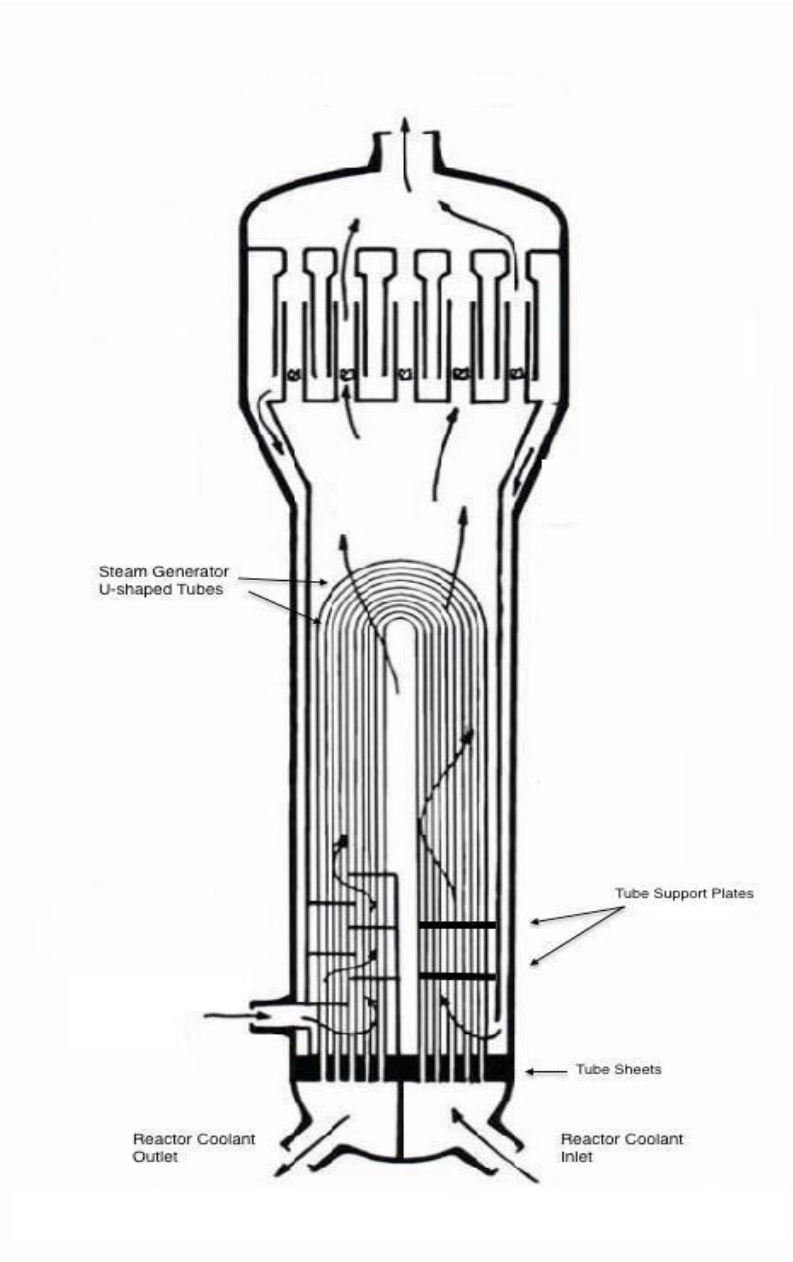


**Figure 2.2:** Nuclear plant steam generator with U-shaped tubes (copied from [4] with written permission)

Moreover, there are different types of in-service NDT techniques in the field to inspect the tubes, and detect, characterize, and monitor any potential defects.

## **2.2 Non-destructive Techniques**

Non-destructive testing methods are widely used in many industries such as aerospace, automotive, and power generation to evaluate the properties of variety of materials without causing damage.

These techniques are commonly utilized for purposes including measuring non-conductive coating thickness and conductivity, determining the hardness of materials after heat treatments, and ensuring the integrity the metallic components of structures such as steam generators in power plants.

There are various NDT testing methods including visual inspection, liquid penetrance, electromagnet, and ultrasound [8]. In liquid penetrant testing, fluorescent or non-fluorescent dyes are used in order to detect cracks on surfaces. In electromagnetic and ultrasonic techniques, magnetic or sound waves are presented to inspect and obtain the properties of materials under test. Moreover, a combination of electromagnetic and ultrasonic methods has also been explored in research using electromagnetic acoustic transducers known as EMATs [9].

Among the NDE techniques, eddy current testing, an electromagnetic technique, has been extensively used to inspect tubes, bars, wires and other products made of conductive materials. ECT is widely utilized in nuclear plants for steam generators' tubes due to allowing high detectability and high speed testing for in-service inspection without requiring any contact between the probes and material under test, and being effective under severe operational conditions [10].

### 2.3 Eddy Current Testing

The eddy current testing is a type of electromagnetic NDE technique whose operation is based on monitoring flow changes of the eddy currents, which are induced by the interaction between a magnetic field source and the material under test. The changes in the eddy currents on conductive materials such as copper, aluminum or steel allow the detection of cracks, and defects on the material under test.

ECT method has advantages over other NDE methods when it comes to inspecting the SG tubes. The eddy current method can be used on a variety of conductive materials ranging from ferromagnetic<sup>15</sup> to non-ferromagnetic<sup>16</sup> materials. In addition, Eddy Current testing can operate at very high speeds. Therefore, it is the best choice for regular in-service inspection of steam generators as they contain many tubes, and timing is an important factor. Also, the eddy current testing can operate under harsh conditions, and the layout restrictions that the tubes in the steam generators have.

The main objective of the utilization of ECT in the steam generators is to correctly detect, and assess any degradation or damages in the tubes, so the tubes can be repaired or removed out of operation. This prevents major incidents and events such as interruptions to the nuclear power plants or toxic leakage into the environment.

The following sections briefly describe the fundamentals of the eddy current testing, the main elements of the eddy current testing equipment, different types of eddy current testing, and probes used to inspect under-test materials.

---

<sup>15</sup> Ferromagnetic materials are strongly magnetized when approaching a magnetic field.

<sup>16</sup> Non-ferromagnetic materials have a small reaction to magnetic field, and therefore do not form permanent magnets.

### 2.3.1 Principles of Eddy Current Testing

Eddy current testing is based on the electromagnetic induction phenomenon where electrical current generated in a conductor by placing the conductor in a time-varying magnetic field.

Faraday's electromagnetic induction law states that a changing magnetic flux in a closed circuit induces a voltage, which results in a current. The magnitude of the induced voltage,  $\mathcal{E}$ , in Equation 2.1 is proportional to the rate of change of the magnetic flux,  $\Phi_B$ , in a closed circuit during a small time,  $t$ . The magnetic flux is defined by integrating the magnetic field,  $B$ , over the area  $A$ . The induced voltage becomes  $N$  greater when a coil with  $N$  turns is used (i.e.  $\mathcal{E} = -N \frac{\partial \Phi_B}{\partial t}$ ).

$$\mathcal{E} = -\frac{\partial \Phi_B}{\partial t} \text{ where } \Phi = \int B \cdot \partial A \quad (2.1)$$

Moreover, according to Lenz's law, the negative sign in Equation 2.1 indicates that the induced voltage creates a current opposing the change of flux, which initially produced the induced voltage [11].

Therefore, in eddy current testing, when an alternating current is applied to a coil, a magnetic field is formed within the coil. As the coil approaches an electrically conductive non-ferromagnetic material, the primary alternating magnetic field in the coil penetrates the test piece. Thus, based on Faraday's law, this penetration generates on the test piece internal circulating currents called eddy currents. The generated eddy currents in turn produce a secondary magnetic field that tends to oppose the primary magnetic field according to Lenz's law as shown in Figure 2.3. When the probe navigates over

irregularities in the test piece, changes occur in the coil impedance<sup>17</sup>, and measuring and plotting these changes in the impedance plane can reveal specific information about the irregularities and discontinuities in the test piece.

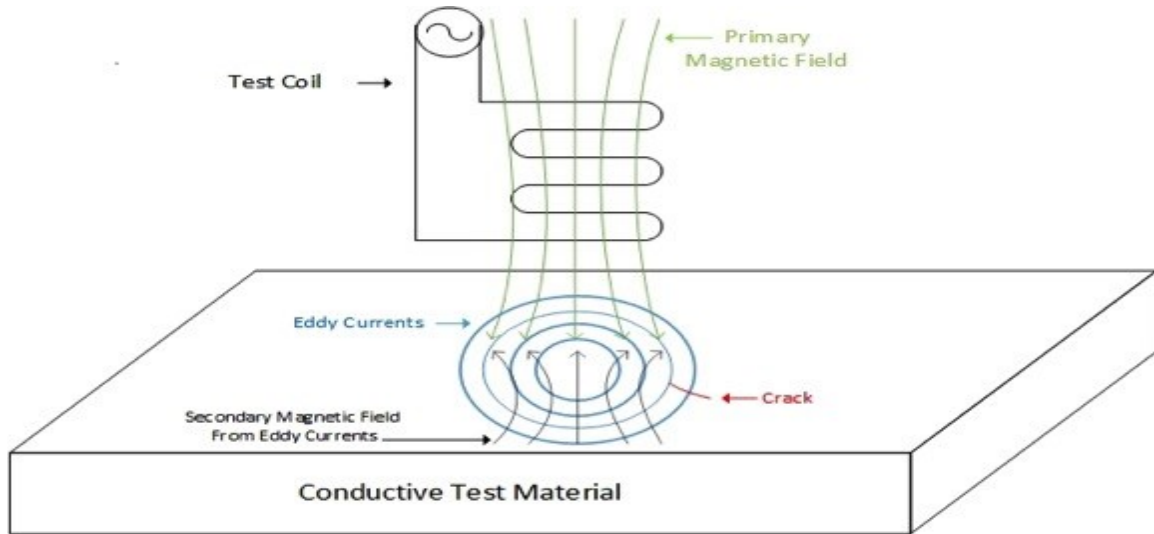


**Figure 2.3:** Eddy current testing principle<sup>18</sup>

The coil impedance ( $Z$ ), represented in the complex form in Equation 2.2, consists of the resistance ( $R$ ) being the real component, and the reactance ( $X_L$ ) being the imaginary component.

$$Z = R + jX_L \quad \text{where} \quad X_L = 2\pi fL \quad (2.2)$$

The frequency ( $f$ ) in Equation 2.2 is the frequency of the alternating current, and  $L$  is the inductance. The changes in the coil impedance are usually represented on a normalized impedance plane by plotting the change in resistance,  $\Delta R$ , against the change in reactance,  $\Delta X_L$  as shown in Figure 2.4. Alternatively, the values for the resistance, and

<sup>17</sup> Impedance is the opposition to current flowing through a coil in an AC circuit.

<sup>18</sup> Figure 2.3 is common knowledge and might be similar to other figures in the literature.

reactance can be normalized to the reactance of the coil when there is no test piece in proximity, i.e.,  $\omega L_0$ .

Since the coil has impedance when no test piece exists in proxy of the coil, this can be used as a reference point from which measurements of impedance can be compared. This reference point is called the air point in which the resistance is zero, and the reactance is one.

As depicted in Figure 2.4, the curves represent conductivity curves, starting from the air point, whose values increase as inductance decreases. Moreover, the distance between the air point,  $P_0$ , and where the flaw signal such as crack exists at  $P_1$  and  $P_2$  are the lift-off lines. The lift-off lines show the proximity of the coil to the test piece. Additionally, the red arrows at  $P_1$  and  $P_2$  are the displacements caused by the flaws.

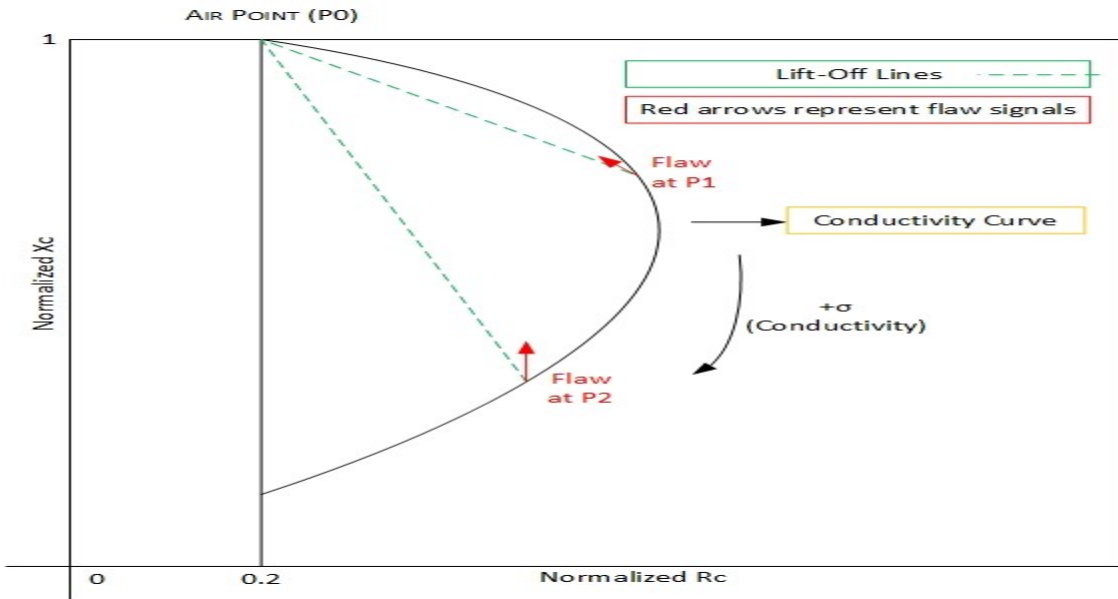


**Figure 2.4:** Flaws, represented by red arrows, in normalized impedance plane<sup>19</sup>

<sup>19</sup> Figure 2.4 is common knowledge and might be similar to other figures in the literature.

When a flaw exists in the test piece at point  $P_1$  in Figure 2.4, the eddy current's path is blocked, and the eddy current path becomes longer. Therefore, the resistance part of the impedance decreases,  $R_C > R_{C+Flaw}$ .  $R_C$  is the resistive part of the coil impedance in proximity of the test piece, and  $R_{C+Flaw}$  is the when a flaw on the test piece changes the resistive part of the impedance. Moreover, With the less current flow, the secondary magnetic field induced by the eddy current becomes smaller which in turn has less effect on the primary field. Therefore, the inductance of the coil impedance becomes larger when a flaw exists on the test piece (i.e.  $X_C < X_{C+Flaw}$ ) [12].

The impedance plane for the coil impedance has two operating areas depending on the material of the test piece as illustrated in Figure 2.5.

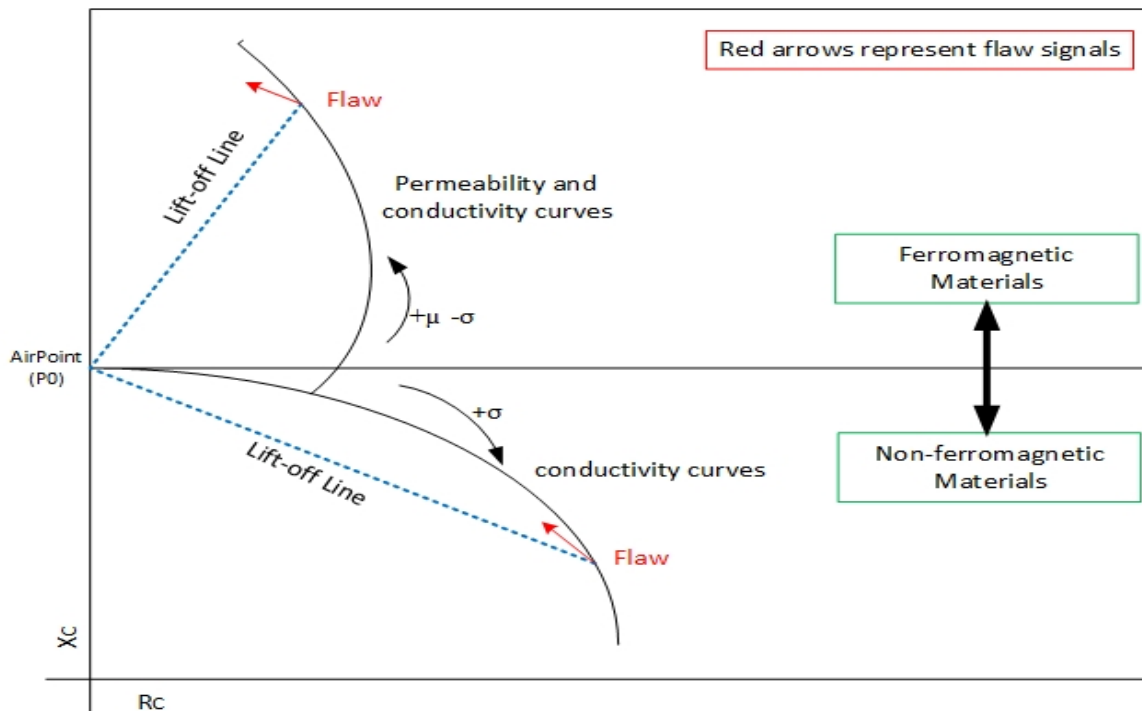


**Figure 2.5:** Flaw signals in Ferromagnetic and non-ferromagnetic materials plotted in impedance plane<sup>20</sup>

<sup>20</sup> Figure 2.5 is common knowledge and might be similar to other figures in the literature.

For ferromagnetic materials such as steel and iron, the imaginary part of the coil impedance (i.e. inductance), is larger than 1, and for non-ferromagnetic materials such as aluminum and copper, the inductance is less than 1. However, the presence of a flaw has the same effects (i.e. decrease in resistance and increase in inductance of the coil impedance) on the coil impedance in both ferromagnetic and non-ferromagnetic materials.

### 2.3.2 Eddy Current Testing Instrument

The functions of the ECT instrument are shown as a block diagram in Figure 2.6. It consists of signal excitation, signal modulation, signal preparation, signal demodulation, and signal display.

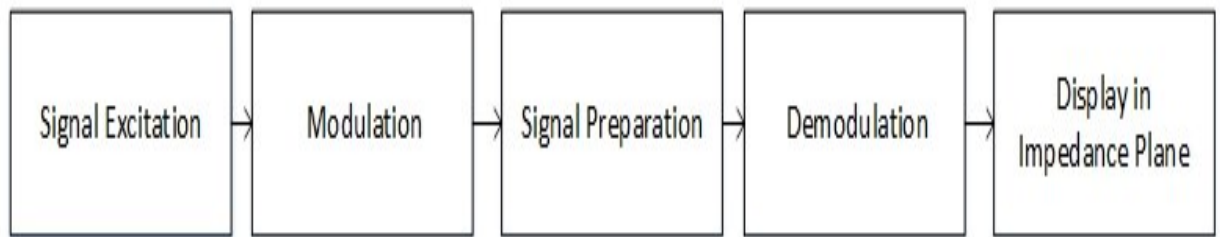


**Figure 2.6:** Block diagram of the eddy current testing (ECT) instrument

When an alternating energized testing coil in the probe navigates over irregularities in the test piece at an excitation frequency, changes occur in the coil impedance. Measuring these changes in the coil impedance by means of current or voltage signal monitoring can reveal specific information about the irregularities and discontinuities in the test piece.

Furthermore, after the impedance changes modulate the tone from the oscillator, the signal is filtered using a bandpass filter for SNR improvement and amplified in the signal preparation stage. It is then demodulated in a phase sensitive detector using a

multiplier. The detector multiplies the modulated signal by two reference signals (in-phase and in-quadrature) of the carrier frequency. The multiplication removes the carrier intermediate frequency, and produces in-phase (I) and quadrature (Q) components as a point in the impedance plane.

These components can then be displayed together as Lissajous patterns or individually on a time plot as inductance and reactance.

### **2.3.3 Variables Effecting Eddy Current Testing**

The value of the coil impedance changes due to variables associated with the test piece as well as the coil in the probe. Test piece associated variables such as the conductivity, permeability, thickness, the presence of a flaw and noise sources, and coil associated variables such as frequency of excitation, coil geometry and proximity to the test piece known as lift off will affect the eddy current response [14]. Since there are many variables affecting the eddy current response, the coil impedance plots are made with some of the variables being constant such as measurement at a fixed excitation frequency with different combinations of conductivity/permeability of the test piece or different lift-off lines.

Some of these variables that affect the eddy current response are described in the following subsections.

#### **2.3.3.1 Conductivity and Magnetic Permeability**

Conductivity ( $\sigma$ ) plays a crucial part in eddy current testing since high conductivity create intense eddy currents on the test piece. With highly conductive materials, the detection of flaws is increasingly improved since higher flaw signal levels are generated as well as the phase lag between the flaws and lift-off line is larger. The

disadvantage of highly conductive materials is that flaws underneath the surface of the test piece are more difficult to detect since the penetration depth is lower at a fixed frequency.

Magnetic permeability ( $\mu$ ), which quantifies the degree of magnetic induction  $B$  of materials when a magnetic field of  $H$  is applied (i.e.  $B = \mu H$ ), can also strongly affect the eddy current response. High permeability in ferromagnetic materials decreases the standard penetration depth, and that makes it difficult to detect flaws under the test piece's surface. Also, ferromagnetic materials have a large variability in magnetic permeability, which have a much greater effect on eddy current response when inspecting eddy current flows [15].

#### 2.3.3.2 **Lift-off**

The lift-off is the changes in the coil impedance when variation in the distance between the testing coil and the test piece exists. This can be caused by the wobbling of the testing coil, unevenness of the surface of the test piece, or the thickness variation in the coating of the test piece. This can negatively affect the eddy current response when detecting flaws on the test piece, and potentially hide the flaw response on the test piece. Therefore, it is desirable to avoid the lift-off by keeping the distance between the coil and the surface of the test piece constant [16].

#### 2.3.3.3 **Excitation Frequency**

The excitation frequency of the coil plays a vital role in detecting flaws appearing on the surface and below the surface of the test-piece. It is the only parameter that can be changed during the inspection of test material. Eddy currents' density decreases exponentially when penetrating through the surface of the test piece at a rate, which

depends on the excitation frequency ( $f_e$ ), the absolute permeability ( $\mu_0$ ), relative permeability ( $\mu_r$ ), and conductivity ( $\sigma$ ) of the test material. The mentioned parameters determine the standard penetration depth ( $\delta$ ) in Equation 2.3, and it can be seen that the penetration depth decreases as conductivity, permeability or test frequency increase [16], [17].

$$\delta = \frac{1}{\sqrt{\sigma\mu_0\mu_rf_e}} \quad (2.3)$$

In eddy current testing, typical inspection frequencies are in the range of 100 Hz–10 MHz. Low frequencies are suitable for subsurface flaws since it penetrates more in the test piece, and high frequencies are used for flaws appearing on the surface. Higher frequencies enables faster inspection speeds, and better sensitivity to defects, however, lift-off noise increases at higher frequencies.

Moreover, non-ferromagnetic materials can be thoroughly inspected for defects at different frequencies due to the fact that the depth of penetration only depends on electrical conductivity of test material and test frequency since relative permeability value is 1. In addition, the depth penetration for ferromagnetic materials is very limited since they have relative and absolute permeability values far larger than 1, and therefore, low excitation frequencies are used to compensate for their high permeability [18].

#### 2.3.3.4 Probes

Coil probes are widely used in eddy current testing, and can be customized for a wide variety of applications. The probes are in eddy current testing classified by the configuration and mode of operation of the coils.

#### **2.3.3.4.1 Probe Configuration**

Configuration refers to how the coils are setup to best serve the test area of interest. The commonly used probes include surface, bobbin, and encircling probes. The surface probes, whose coil axis is perpendicular to the test piece, are commonly used for flat surface inspection to detect surface discontinuities.

The bobbin probes, also known as Inside Diameter (ID) probes, are intended for hollow products such as tubes and pipes to inspect from inside out. The Bobbin probe coils are wound around the probes in order to inspect the entire circumference of the test piece at one time as they travel through. The encircling probes, also known as Outside Diameter (OD) probes, have coils, which encircle solid products such as bars to inspect from outside in [19].

#### **2.3.3.4.2 Operation Mode**

The commonly used operation modes for coil probes include absolute and differential modes. In the absolute mode, probes use a single coil to generate eddy currents on the test piece, and senses the impedance changes. Absolute probes are widely used due to their versatility for flaw detection, and lift-off, thickness and conductivity measurements.

In the differential mode, two active coils are engaged to compare two adjacent parts of the test piece. When the two coils are inspecting the same test area without a flaw, the output voltage of the differential coil probe is zero. However, when one coil is over a defect, a differential signal is produced. The advantage of the differential mode is that probes are very sensitive to defects, but insensitive to gradual temperature and dimensional variations. The disadvantage of this mode is that the produced signals can be

complex to analyze long defects as only the edges of the defects can be detected due to signal cancelation when both the test coils are over the defects. [19].

### **2.3.3.5 Types of Eddy Current Testing**

Eddy current testing can be carried out for a variety of applications such tube inspection using different techniques including conventional eddy current, multi-frequency eddy current, and pulsed eddy current [12]. These methods are discussed briefly below.

#### **2.3.3.5.1 Conventional Eddy Current Testing**

In conventional ECT, a single frequency used to excite the testing coil. The depth of penetration of eddy currents limits this method of ECT since only a single frequency used. Therefore, it is suitable a method of choice for testing surface and near surface flaws such as cracks of depth of a few millimeters.

#### **2.3.3.5.2 Multi-frequency Eddy Current Testing**

The multiple frequency eddy current technique can be implemented using conventional ECT equipment to find discontinuities and cracks located at different depth levels. In this method, multiple frequencies are used to collect data from the test piece simultaneously, and collected data can then be compared or fixed for further noise reduction or flaw detection.

This technique is commonly used for inspection of the steam generator tubes. An example of its application in the SG tube inspection is to reduce the response of the TSPs that are placed on the outside of the tubes. The response of the TSPs can potentially hide the flaw response, and hinder the detection and assessment of flaws.

The effect of the TSPs can be suppressed using mixing data, which is produced by subtracting the data collected at a lower frequency containing a higher resolution of the support plate response [20].

#### **2.3.3.5.3 Pulsed Eddy Current (PEC)**

In PEC testing, a step function voltage is used to excite the probe. Pulsed instruments produce square, triangular or a saw tooth waveforms, which cover a broad spectrum of frequencies. The advantage of using waveforms is that it can provide information at different depths to better detect and characterize the flaws. Also, testing can be performed through coatings and insulation materials since a broad range of frequencies are used.

The frequency content of the generated pulses depending on their lengths can range from less than 100 Hz to 2 kHz. The obtained pulse from the test piece can be plotted in the form of the variation of amplitude or phase with frequency [21].

### **2.4 Eddy Current Testing Procedure for Steam Generator Tubes**

Inspection of steam generators at power nuclear plants is carried out regularly to identify new defects as well as to monitor the growth of the pre-existing flaws to prevent them from causing operation interruption or any potential leakage. Steam generators at power nuclear plants such as CANDU, can contain up to 10,000 U-shaped tubes. Therefore, for fast in-service inspection of steam generator tubes, eddy current testing as a non-destructive technique, is widely used. As mentioned in the previous sections, eddy current testing can unveil flaws on the surface of tubes more effectively.

To inspect, probes are inserted into the tubes as shown in Figure 2.7, and data gets collected as probes are pulled from the tubes to reduce the effect of probe wobbling.

Different probes are used depending on the type of flaws as mentioned in the previous section. Bobbin probes have been used for the collected data in this research [22].

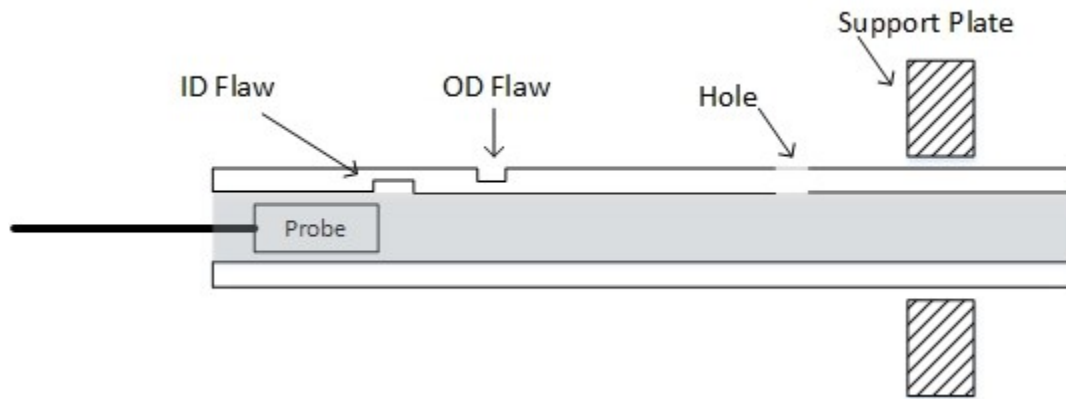


**Figure 2.7:** Probe insertion in tube to collect data for inspection

The multi-frequency eddy current technique is typically utilized in inspection of steam generator tubes to collect data at different frequencies. The typical range of test frequencies in ECT is between 100 Hz and 10 MHz. The frequencies at which the inspection data had been collected for this research are 120kHz and 240 kHz. The higher frequency such as 240 kHz has a better response to flaws in the surface of the tubes, and the lower frequency such as 120 kHz provides a better response to noise sources surrounding the tubes including support plates. These sets of data can then be compared or combined for further analysis of potential flaws.

The collected data contain different noise sources coming from the test tube, test equipment or the surroundings, which hinder detection and characterization of flaw signals. This is where the vital role of signal processing comes into play. In order to reduce the effect of noise sources such as lessening the effect of tube support plates' responses, and to identify, classify and characterize potential new or existing flaws, different signal processing techniques are utilized.

The end goal of eddy current testing (ECT) in steam generator (SG) is to automate

the entire inspection process including detection, classification and characterization of flaw signals using signal processing. This process is currently carried out by human analysts, and can be prone to human errors.

## **2.5 Noise Sources for ECT in SG Tubes**

Flaw signals in eddy current testing for SG tubes are probe responses that are associated with any form of tube degradation. On the other hand, noise in the ECT context refers to any undesirable probe response from any irrelevant source that obscures the detection and analysis of flaw signals.

### **2.5.1 Common Sources of Noise**

Typically, the analysis of ECT data of steam generator tubes is very complex due to the fact that many noise and interference sources present in the surrounding can distort flaw signals. These noise sources decrease the SNR, and therefore, the detection of flaw signals becomes a difficult task. The SG tubes, the testing equipment or the tube surroundings are the common sources for noise.

The noises in the SG tubes can be property variations such as conductivity and permeability, non-uniform surface conditions, and changes in manufactured tube dimensions and geometry. The noise sources associated with the test equipment are probe wobbling, lift-off, and electronic noise. Moreover, the noise sources that come from the surroundings of the SG tubes are the plates supporting the tubes at different intervals, and uniform deposits from corrosion products appearing on the inside or outside of the tubes.

### **2.5.2 Types of Noise**

Common noise sources in ECT of steam generator tubes can be generally divided into two main categories, deterministic and random noise [23].

Deterministic noise is unwanted signals that possess predictability in spatial, and

frequency distribution. Examples of deterministic noise sources include denting, deposits, changes in manufactured tube dimensions and geometry, probe movement in operation, TSPs holding the tubes, gradual changes in the tube surface, and lift-off noise. On the other hand, random noise has spatial and frequency distributions that are not predictable, and therefore, it is non-stationary. Random noise sources are caused by electronic noise from the test equipment, random variations in the electrical conductivity and magnetic permeability of the tubes, and heat treatment in tube manufacturing processes [24].

### **2.5.3 Low Frequency Sinusoidal Noise**

Some of the deterministic noise sources in eddy current testing for the inspection of steam generator tubes produce low-frequency responses that can make interpretation of flaw signals of interest difficult. It is an important step in analyzing and characterizing flaw signals to identify these low frequency sinusoidal noises, and reduce their effect in the ECT collected data.

The periodic variation in the distance between the test coil probe and the test piece due to periodic variations in coating thickness, and irregular tube surface is considered a source of low frequency noise.

Probe wobbling is another source of low frequency noise that is caused by a change in the alignment of the probe in respect to the tube axis. Probe guide, or coil housing can produce the change in the alignment of the probe. Excessive Probe wobbling can significantly distort flaw's amplitude and phase, and therefore, it is desirable to reduce its effect.

The reduction of low-frequency sinusoidal noise from the ECT data collected from the inspection of SG tubes in order to enhance the detection of flaws is the focus of this thesis.

## Chapter 3: Literature Review

There are conventional techniques to distinguish between flaw signals from unwanted noise signals. One of these approaches is to inspect and collect data at different frequencies as flaw and noise signals respond differently to various frequencies. By examining the impedance plane plots at different frequencies, flaw signals can be identified<sup>21</sup>, and further characterized. Also, mixing frequency techniques are commonly used to suppress the support plates' responses from the collected data [22]. Figure 3.1 shows a TSP response at 120 and 240 KHz frequencies, which can be used to reduce the support plate responses by subtracting one from another using mixing frequency techniques.

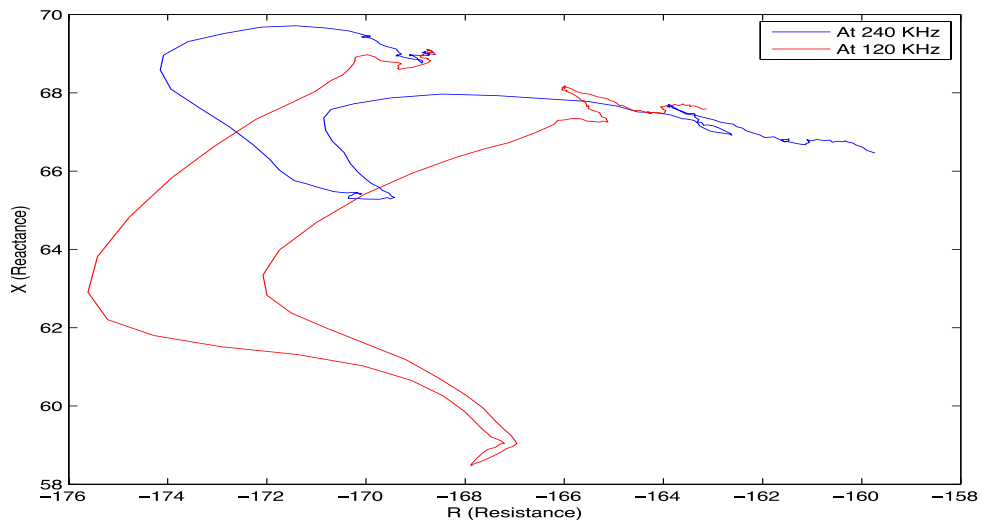


**Figure 3.1:** TSP response at Frequencies 120 and 240 KHz<sup>22</sup>, which can be used to reduce the support plate response by subtracting one from another, by means of mixing frequency techniques.

---

<sup>21</sup> Flaw signals act differently using different frequencies. For example, an ID flaw's phase stays the same at different frequencies. However, magnetite, which is not considered a flaw, has its phase change at different frequencies.

<sup>22</sup> Figure 3.1 is produced from the set of data provided by CNL for this research

However, due to presence of many noise sources in vicinity of flaws, the flaw signals can be significantly distorted, and the conventional techniques might not be sufficient to detect flaws.

There have been various signal processing techniques proposed and developed over the years to address the reduction of the effect of these noise sources in eddy current inspection. The main purpose of these techniques is to improve the SNR in order to detect flaw signals in the presence of noise. Since there are random and deterministic noise sources of different kinds in inspection of SG tubes, a signal processing technique needs to be developed to address each group of these noise sources. Some of these techniques are briefly explained in Section 3.1. However, these signal processing noise reduction techniques in Section 3.1 do not address the low frequency sinusoidal noise, which is the focus of this research. Recently [3] has proposed a technique using Cyclic-Music algorithm, which addresses the reduction of the periodic low frequency noise. The Cyclic-Music algorithm is discussed in Section 3.2.

### **3.1 Signal Processing Noise Reduction Techniques**

To overcome random noise generated by random variations in lift-off due to probe wobble, and variations of surface roughness, signal-processing algorithms have been proposed in [25] and [26] that make use of adaptive filters, which can adapt to the changing signal and noise characteristics.

The algorithm proposed in [25] consists of using an adaptive filter as the initial step followed by a wavelet based de-noising technique. The proposed adaptive filter is a finite impulse response (FIR) filter, which uses a normalized least mean square (NLMS) to estimate the filter's coefficients. The algorithm tends to solve a minimum mean square error (MMSE) problem in Equation 3.1 where  $s$  is the flaw signal sequence,  $\eta$  is the

noise contained in  $s$ , and  $y$  represents the best estimate of the noise vector.

$$\varepsilon = s + \eta - y \quad (3.1)$$

The error signal,  $\varepsilon$ , at the output of the adaptive filter ultimately gives an estimate of the desired flaw signal. The second part of the algorithm is meant to remove any residual random system noise.

Moreover, as a next step, [25] proposed a dynamic thresholding algorithm based on Neyman–Pearson (NP) hypothesis to calculate a variable threshold to mark all signals above the threshold as possible defects. This will reduce the number of data points for analysis. The algorithm decomposes the signal into smaller segments through a sliding window, and a threshold is obtained for each segment of data. The Neyman–Pearson (NP) detector is used to maximize the probability of detection of defect signals by obtaining the variance-based optimal threshold for a given probability of false alarm (PFA).

The method proposed in [26] utilizes a modified version of the adaptive Wiener filter (AWF) called weighted adaptive Wiener filter, which uses a non-rectangular window to process the data. According to [26], adaptive Wiener filters are able to estimate power spectral density (PSD) of signal and noise online, possess fast processing to due low computational complexity, and can adapt to a variety of eddy current data.

There have been other signal processing methods proposed such as [27] and [28] that make use of Discrete Wavelet Transform (DWT) to reduce the effect of probe lift-off noise from ECT data of SG tubes. Discrete Wavelet Transform reduces the noise by decomposing the collected data into wavelet components, and modifying the wavelet coefficients. The modified wavelet coefficients can then be used to construct the defect signals embedded in noise by means of inverse wavelet transform. Even though Discrete

Wavelet provides a better SNR, it is costly to implement, and a right wavelet needs to be selected in order to avoid distorting useful signals.

The techniques in [25], [26], [27] and [28] are intended to reduce random low-frequency noise such as lift-off noise, and do not address other sources of noise such as low-frequency sinusoidal noise which can be caused by periodic probe wobbling or periodic variations in tube surfaces. However, [3] has recently proposed a method using Cyclic-Music algorithm to reduce such low-frequency sinusoidal noise which is contained in steam SG tube data collected by a bobbin probe.

### 3.2 Cyclic-Music Algorithm

The Cyclic-Music algorithm in [3] has two main components. The first component acquires the initial estimation for the frequency by the Multiple Signal Classification (MUSIC) algorithm as shown in Equation 3.2.

$$P_{XX}^{MUSIC}(f) = \frac{1}{s^H(f)V(f)V^H(f)s(f)} \quad (3.2)$$

Where  $s(f) = [1, e^{j2\pi f}, \dots, e^{j2\pi(N-1)f}]$  is the complex sinusoidal vector, and  $V = [v_{p+1}, \dots, v_N]$  is the matrix of the noise subspace. The frequencies sharply peaked in  $P_{XX}^{MUSIC}$  are the estimated frequencies.

Moreover, linear regression with least squares estimates is used to estimate the phase and amplitude sinusoidal components of the signal as shown in Equations 3.3 and 3.4.

$$V_{Amplitude} = \begin{bmatrix} \sqrt{x(2)^2 x(3)^2} \\ \sqrt{x(4)^2 x(5)^2} \\ \vdots \end{bmatrix} \quad (3.3)$$

$$V_{Phase} = \begin{bmatrix} \text{atan}(-x(3), x(2)) \\ \text{atan}(-x(5), x(4)) \\ \vdots \end{bmatrix} \quad (3.4)$$

$X = \begin{bmatrix} x(1) \\ x(2) \\ x(3) \\ \vdots \\ \vdots \end{bmatrix}$  is obtained from the left matrix division of  $X = A \backslash \text{data}$  where  $A =$

$$\begin{bmatrix} 1 & \cos(2\pi f_1) & \sin(2\pi f_1) & \dots \\ \vdots & \vdots & \vdots & \vdots \\ 1 & \cos(2\pi f_1 n) & \sin(2\pi f_1 n) & \dots \end{bmatrix}.$$

The second component applies the initial estimates, obtained in Equations (3.2), (3.3) and (3.4), to a modified version of the Relaxed algorithm. The Relaxed algorithm uses the maximum likelihood estimation and nonlinear least square, and takes the FFT to obtain the improved estimates. In the modified version of the Relaxed algorithm, each sinusoid is estimated by taking the FFT of the residual signal acquired from the subtraction of the ECT data from the summation of other initially estimated sinusoids as shown in Equation 3.5:

$$\hat{y}_l = y - \sum_{k=1}^K \hat{a}_k a(\hat{\theta}_k) \quad (3.5)$$

In Equation 3.5,  $y$  is the collected eddy current testing ECT data,  $K$  is the known number of complex sinusoids,  $\theta_k$  is the frequency estimate, and  $a_k$  is the amplitude and phase estimates as in  $a_k = |a_k| e^{j\phi_k}$ .

In addition, since the existence of non-periodic peak signals such as flaw signals in the ECT data skews the frequency estimation of sinusoidal noise additional steps must be taken such as replacement of the peak by the mean of the segment to improve estimate the frequency [3].

## **Chapter 4: Weighted Multipoint Interpolated DFT (WMIpDFT)**

### **Technique**

As mentioned in the previous sections, removing noise and unwanted signals from the eddy current testing plays an important role in detecting and characterizing flaw signals. The proposed algorithm in this study focuses on removing low frequency sinusoidal noise caused by the periodic probe wobbling and gradual variations in tubes' surface caused in manufacturing processing.

The proposed algorithm in this study takes a different approach by utilizing the WMIpDFT technique in estimating the sinusoidal parameters of low frequency noise. This is different from the Cyclic-Music algorithm, proposed in [3], which incorporates the Music algorithm, a time-domain frequency estimation method, and the FFT, the algorithmic version of DFT. Time-domain methods generally require an accurate signal model and model order to provide good frequency estimate. Moreover, the DFT methods suffer from spectral leakage and picket effects due to incoherent sampling. Therefore, both time-domain and DFT methods do not perform effectively considering the above issues. Additionally, these methods do not perform well when it comes to presence of non-periodic components.

V. K. Jain and et al in [29] proposed a method called interpolated DFT (IpDFT), which encounters the spectral leakage by interpolating between the discrete points of a DFT spectrum. This method was further improved in [30] to address not only the short-leakage from the main-lobe, but also the interference caused by other components of multi-frequency signals. The method in [30] combines the interpolation algorithm with a

tapered time window, such as a Hanning window, which reduces the effect of interference introduced by other components of the signal. Generally, IpDFT methods perform well when they are implemented with Rife-Vincent windows (generalization of the Hanning window) since the parameters can be estimated by analytical formulas.

The estimates from IpDFT are fairly accurate, however, the estimates can still suffer from systematic errors caused by the spectral interference due to the signal imaginary component, and random noise due to quantization noise [31]. A method suggested by D. Belega and D. Dallet [32] addresses the systematic errors using more interpolation points, and therefore, it is called weighted multipoint interpolated DFT (WMIpDFT). The method considers the number of interpolation points to be  $2J+1$ , where  $J$  is greater or equal to one, and the maximum side-lobe decay windows with an order of  $H^{23}$  higher than or equal to two. The random error, mentioned earlier, depends on the number of sample, and therefore, can be reduced by increasing the number of samples.

#### 4.1 Theoretical Background

In the following equation (4.1), the multi-frequency signal sampled at the frequency of  $f_s$  is considered:

$$x(m) = \sum_{k=1}^K A_k \sin\left(2\pi \frac{f_k}{f_s} m + \varphi_k\right), m = 0, 1, 2, \dots, M-1 \quad (4.1)$$

where  $K$ ,  $M$ ,  $A_k$ ,  $f_k$ , and  $\varphi_k$  are the number of frequency components, acquisition length, amplitude, frequency, and phase of the  $k$ th component respectively. The multi-frequency

---

<sup>23</sup>  $H$  is the window order for maximum side-lobe decay windows, known as Rife-Vincent windows. When  $H$  is 2, the window becomes a Hanning window (2-term maximum side-lobe decay window).

signal is assumed to have an additive white Gaussian noise with zero mean and  $\sigma^2$  standard deviation.

It is assumed that the sampling frequency ( $f_s$ ) is greater than twice the highest frequency component ( $f_k$ ) to eliminate the aliasing effects and satisfy the Nyquist criterion. However, the focus is on leakage effects caused by incoherent sampling [32]. The incoherent sampling occurs when the signal frequency is not an integer multiple of  $f_r$ , the resolution frequency. This means that  $\lambda_k$ , the number of recorded sine-wave cycles associated with the  $k$ th component of the multi-frequency signal, has a fractional part ( $\delta_k$ ) in Equation 4.2 [33]:

$$f_k = \lambda_k f_r = (l_k + \delta_k) f_r = (l_k + \delta_k) \frac{f_s}{M} \quad (4.2)$$

where  $l_k$  and  $f_s$  are the integer part of  $\lambda_k$ , and the sampling frequency respectively.

When  $\delta_k$  is equal to 0 the sampling is coherent, and therefore, an individual component of the multi-frequency signal appears as an ideally sharp peak in the spectrum. However, a non-zero  $\delta_k$  leads to non-coherent sampling causing the peak of an individual signal component to leak over to adjacent frequency bins in the spectrum. Since non-coherent sampling is unavoidable, the precision of  $\delta_k$  estimation is of high importance.

To reduce this spillover or spectral leakage effects in non-coherent sampling, and further improve the signal parameter estimation, the signal  $x(m)$  is multiplied by  $w(m)$ , a  $H$ -term maximum side-lobe decay window, where  $H$  is greater or equal to two. Also, the time domain and frequency domain responses of the 3-term window function are depicted

in Figure 4.1.

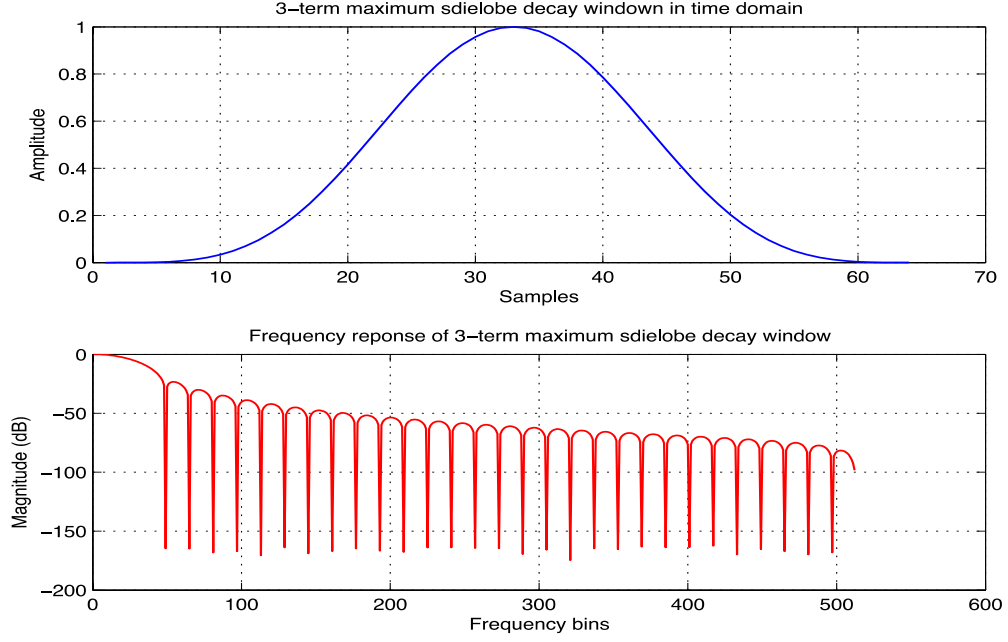


**Figure 4.1:** 3-term maximum side-lobe decay window in time domain (top plot) and its 5 (bottom plot)

The analytical expression of  $w(m)$  is shown in Equation 4.3 [33] where the window coefficients  $a_h$  are given in Equation 4.4:

$$w(m) = \sum_{h=0}^{H-1} (-1)^h a_h \cos\left(2\pi h \frac{m}{M}\right), \quad m = 0, 1, \dots, M-1 \text{ \& } H \geq 2 \quad (4.3)$$

$$a_0 = \frac{C_{2H-2}^{H-1}}{2^{2H-2}}, \quad a_h = \frac{C_{2H-2}^{H-h-1}}{2^{2H-3}}, \quad C_m^p = \frac{m!}{(m-p)!p!}, \quad h = 1, 2, \dots, H-1 \quad (4.4)$$

The discrete Fourier transform  $W(\lambda)$  of the window function can be accurately approximated in the following formula (4.5) [33].

$$W(\lambda) = \frac{M \sin(\pi \lambda)}{2^{2H-2} \pi} e^{-j \frac{\pi(M-1)\lambda}{M}} \frac{(2H-2)!}{\lambda \prod_{h=1}^{H-1} (h^2 - \lambda^2)} \quad (4.5)$$

Moreover, the discrete Fourier transform of  $x_w(m)=x(m)*w(m)$ , where  $x_w(m)$  is the windowed signal, is shown in the following equation (4.6) where  $\lambda$  is the normalized frequency expressed in bin [33]:

$$X_w(\lambda) = A_0W(\lambda) + \sum_{k=1}^K \frac{A_k}{2^j} [W(\lambda - \lambda_k)e^{j\varphi_k} - W(\lambda + \lambda_k)e^{-j\varphi_k}], \quad \lambda \in [0, M) \quad (4.6)$$

By using the H-term maximum side-lobe decay window, the magnitudes of the largest component and its adjacent components, obtained from Equation 4.6, can be expressed in the analytical form as shown in Equation 4.7. The magnitude of the largest component of the spectrum  $|X_w(l_k)|$  in Equation 4.7 comprises of two components; short-range spectral leakage (i.e.  $W(\delta_k)$ ) being the first term weighted by  $\frac{A}{2}$ , and long-range spectral leakage (i.e.  $\Delta(l_k)$ ) resulted from the imaginary part of the  $k$ th signal component and from other multi-frequency signal components, being the second term  $\Delta(l_k)$  [33-34].

$$\begin{aligned} |X_w(l_k - 1)| &= \frac{A_k}{2} |[W(1 + \delta_k)e^{j\varphi_k} - W(2l_k - 1 + \delta_k)e^{-j\varphi_k}]| + \sum_{i=0, i \neq k}^K |\Delta(l_i)| \\ &= \frac{A_k}{2} |(W(1 + \delta_k)| \mp \Delta(l_k - 1) \\ |X_w(l_k)| &= \frac{A_k}{2} |[W(\delta_k)e^{j\varphi_k} - W(2l_k + \delta_k)e^{-j\varphi_k}]| + \sum_{i=0, i \neq k}^K |\Delta(l_i)| \\ &= \frac{A_k}{2} |(W(\delta_k)| \pm \Delta(l_k) \\ |X_w(l_k + 1)| &= \frac{A_k}{2} |[W(1 - \delta_k)e^{j\varphi_k} - W(2l_k + 1 + \delta_k)e^{-j\varphi_k}]| + \sum_{i=0, i \neq k}^K |\Delta(l_i)| \\ &= \frac{A_k}{2} |(W(1 - \delta_k)| \mp \Delta(l_k - 1) \end{aligned} \quad (4.7)$$

As  $\lambda_k$  gets larger, the  $\Delta(l_k)$  in the largest component and the term in adjacent

frequency bins  $\Delta(l_k \pm i)$  become very close to each other.

## 4.2 Signal Parameter Estimation using WMIpDFT

In the following sections, the estimation of the frequency, amplitude and phase of a signal component is shown using WMIpDFT.

### 4.2.1 Frequency Estimation

As mentioned in the previous section, in order to estimate the  $f_k$ , the normalized frequency  $\lambda_k$ , expressed in bins, needs to be calculated. The accurate estimation of  $\lambda_k$  depends on  $l_k$  which corresponds to the largest component of the  $k$ th component in the spectrum, and importantly the fractional part  $\delta_k$ .  $\delta_k$ , for the number of interpolation points  $2J+1$ , is acquired by first calculating the following ratio  $\alpha_k$  [32]:

$$\frac{\sum_{i=1}^J C_{2J-2}^{J-i} [|X_w(l_k + i)| - |X_w(l_k - i)|] - \sum_{i=1}^{J-2} C_{2J-2}^{J-i-2} [|X_w(l_k + i)| - |X_w(l_k - i)|]}{\sum_{i=1}^J C_{2J}^{J-i} [|X_w(l_k - i)| + |X_w(l_k + i)|] + C_{2J}^J |X_w(l_k)|} \quad (4.8)$$

From the above ratio in 4.8, it is assumed that the interpolation points fall within the spectrum main-lobe. Moreover, the terms associated with the long-range leakage in Equation 4.7 become small and very close (i.e.  $|\Delta(l_k - i)| \approx |\Delta(l_k)| \approx |\Delta(l_k + i)|$  as  $\lambda_k$  increases, and they take different signs. Therefore, when the magnitudes are added together, the effect of the long-range leakage become neglected. The weights (in the form of binomial coefficients) for the magnitudes come from the  $2J$ -order finite difference of  $|\Delta_{2J}(l_k - J)|$ .  $2J$ -order finite difference is utilized to take into account the contributions from all the terms  $\Delta(l_k \pm i)$ ,  $i=0,1 \dots J$ , involved in the interpolation.

$\delta_k$  can be estimated by substituting the magnitude equations from 4.7 into Equation 4.8 to get the ratio  $\alpha_k$ , and using the equation in 4.9 below.

$${}_{2J+1}\delta_k = (H + J - 1)\alpha_k \quad (4.9)$$

Having the fractional part  $\delta_k$  of  $\lambda_k$  estimated, the integer part  $l_k$  can be easily determined by searching for the maximum magnitude associated with the  $k$ th component in the spectrum. The frequency of the signal's  $k$ th component ultimately is estimated from 4.2 by multiplying  $\lambda_k$  with the frequency resolution [32].

#### 4.2.2 Amplitude Estimation

Similar to the estimation of  $\delta_k$  where an analytical formula was used due to the utilization of the maximum side-lobe decay windows, the amplitude of each signal component  $A_k$  can also be obtained with means of an analytical formula. Using the equations 4.5, 4.6 and 4.7, and taking into account the effects of long-range leakage, the  $A_k$  for any number of interpolation points becomes Equation 4.10 [35].

$${}_{2J+1}A_k = \frac{2^{2H-1}\pi\delta_k \prod_{h=1}^{H+J-1}(h^2 - \delta_k^2)}{M \sin(\pi\delta_k)(2H+2J-2)!} \times \left[ \sum_{i=1}^J C_{2J}^{J-i} [|X_w(l_k - i)| + |X_w(l_k + i)| + |X_w(l_k)|] \right] \quad (4.10)$$

#### 4.2.3 Phase Estimation

The phase  $\varphi_k$  of the  $k$ th component of the multi-frequency signal can be accurately estimated using the following formula in 4.11 [36]. The formula is derived from the main component  $X_w(l_k)$  in Equation 4.7, and the DFT of the window function.

$$\varphi_k = Phase\{X_w(l_k)\} - \pi\delta_k + \pi \frac{\delta_k}{M} - \frac{\pi}{2} sign(\delta_k) - Phase\{W_o(-\delta_k)\} \quad (4.11)$$

In Equation 4.7,  $\delta_k$  is the fractional part of  $\lambda_k$ , which is calculated in the frequency estimation, and  $W_0$  is obtained using Equation 4.12. Moreover, the sign () is the sign function that changes as shown in 4.13.

$$W_o(\lambda) = \sum_{h=0}^{H-1} (-1)^h 0.5 a_h \left[ \frac{e^{-j\frac{\pi}{M}h}}{\sin \frac{\pi}{M}(\lambda - h)} + \frac{e^{j\frac{\pi}{M}h}}{\sin \frac{\pi}{M}(\lambda + h)} \right] \quad (4.12)$$

$$\text{sign}(\delta_k) = \begin{cases} -1, & \text{if } -0.5 \leq \delta_k < 0 \\ 1, & \text{if } 0 < \delta_k < 0.5 \end{cases} \quad (4.13)$$

The above phase estimation equation can be reduced to a simpler equation whose result is comparable with that of the above equation. The formula for this phase estimate approach given in 4.14 [29]:

$$\varphi_k = \text{Phase}\{X_w(l_k)\} - \pi \frac{(M-1)}{M} \delta_k + \frac{\pi}{2} \quad (4.14)$$

### 4.3 WMIPDFT Performance Factors

#### 4.3.1 Frequency and Systematic Errors

As the value of  $l_k$  increases, the systematic errors, stemmed from the imaginary part of the signal components, become smaller than errors due to the noise, and therefore, the accuracy of  $\delta_k$  and  $A_k$  estimates does not practically change [33-36]. This means that estimates obtained by WMIPDFT methods will not improve if the frequency increases. Consequently, the WMIPDFT methods are highly suitable to be utilized when the frequency is not very large, and the signal is not corrupted by high power noise (meaning greater signal to noise ratio).

### 4.3.2 Combined Standard Uncertainty for Normalized Frequency Estimator

Standard uncertainty of the normalized frequency estimate is used to obtain the efficiency of the WMIpDFT. Due to real-life situations, a white Gaussian noise with zero mean and variance  $\sigma^2$  is added to the signal. Moreover, Standard uncertainty is calculated by considering systematic errors, which are caused by the spectral interference from the imaginary part of the signal component, and random errors stemming from wideband noise. The uncertainty is defined as the square root of the sum of square of effective value of systematic errors and the variance of the frequency estimate affected by random noise. The following equation (4.15) is the combined uncertainty of frequency estimator for  $2J+1$  interpolation points and H-term maximum side-lobe decay window [36] where  $\Delta_{2J+1\delta_H}$  is the interference error, and  $\sigma_{2J+1\delta_H}^2$  is the standard uncertainty of wideband noise.

$$u_{2J+1\delta_H} = \sqrt{\frac{(|\Delta_{2J+1\delta_H}|_{max})^2}{2} + \sigma_{2J+1\delta_H}^2} \quad (4.15)$$

The combined uncertainty has been used for frequency estimator in [37] to compare the performance of IpDFT (i.e. using only two interpolation points) and WMIpDFT methods as a function of fundamental frequency ( $\lambda$ ), and to find the optimal values for the number of interpolation points.

### 4.3.3 Statistical Efficiency of WMIpDFT

In order to obtain the statistical efficiency of WMIpDFT methods with maximum side-lobe decay windows, the ratio between the variance from fractional frequency estimate and the corresponding unbiased Cramér–Rao (CR) lower bound is calculated. Assuming that the signal is corrupted by white Gaussian noise, the CR lower bound for

the fractional frequency is expressed as shown in Equations 4.16 respectively [32]:

$$var(\hat{\delta}_k)_{CR} = \frac{6}{\pi^2} \frac{\sigma_n^2}{MA_k^2} \quad (4.16)$$

[31] and [33] have shown that the statistical efficiency of WMIPDFT decreases as the number of interpolation points increases. However, increase in the number of interpolation points leads to decrease in systematic errors.

#### 4.3.4 Choice of the Number of Interpolation Points and Window Order (H)

##### 4.3.4.1 Number of Interpolation Points

In order to determine the optimal number of interpolation points, the frequency estimator must lead to minimum combined standard uncertainty. Therefore, one can find the optimal number of interpolation points for the frequency range of interest by using the combined standard uncertainty expression (4.15) that returns the minimum combined standard.

In [37], different number of interpolation points are used to compute the combined standard uncertainty using Equation 4.15 for a signal corrupted by an additive Gaussian noise with zero mean and standard deviation  $\sigma_n^2$ . It has been shown that high numbers of interpolation points (i.e. 5 and 7) are suitable for lower frequency bins such as under 6-7 Hz. For higher frequency bins lower number of interpolation points such as 3 will perform better.

It is important to note that as the number of interpolation increases the systematic error effect on parameter estimations (i.e. spectral interference contribution) decreases. However, as mentioned earlier, this will lead to poor statistical efficiency. The decrease in systematic errors is also true for large values of frequency bins [38]. This means higher

number of interpolation points will not lead to more accurate estimates when  $\lambda_k$  is large. Therefore, in order to choose  $J$  to obtain accurate estimates, besides combined standard uncertainty for frequency estimate, it is vital to take into account the effect of systematic errors, frequency range and statistical efficiency.

#### 4.3.4.2 **Window Order (H)**

In WMIPDFT, the maximum side-lobe decay windows, known as Rife-Vincent windows, are employed in order to reduce the effect of both long-range leakage due to other components in the multi-frequency signal, and the imaginary part of the signal component. Moreover, by increasing the order  $H$  of the window, the long-range leakage due to the imaginary part of the signal component becomes smaller than random errors. However, similar to the number of interpolation points, the increase in  $H$  will lead to increase in uncertainties of the parameter estimates [39]. Thus,  $H$  must be chosen low enough such as 2 to ensure that systematic errors fall just below the random noise.

## Chapter 5: Proposed Iterative WMIpDFT Algorithm

The proposed algorithm makes use of the WMIpDFT method to estimate the parameters of the sinusoidal noise existing on the ECT data. As opposed to time domain and DFT approaches, interpolated DFT methods are more robust to non-periodic noise. Moreover, unlike windowed interpolated DFT approaches that utilize only two interpolation points, WMIpDFT improves the accuracy of parameter estimates by using more interpolation points, which leads to reduction in systematic errors caused by the imaginary part of the signal component. The overall operation of the Iterative WMIpDFT algorithm for the  $k$ -component noise signal, as shown in Figure 5.1, is as follows.

- The algorithm estimates the parameters  $(f_1, A_1, \varphi_1)$  of the first component  $k_1$  of the noise signal.
- Noise signal  $S_1$  (i.e.  $A_1 \cos(2\pi f_1 nT + \varphi_1)$ ) is subtracted from the original data,  $x(n)$ , to get the residual signal ( $R_1$ ).
- The residual signal is fed back into the algorithm for the estimation of the noise signal's  $k_{th}$  sinusoidal component's parameters  $(f_2, A_2, \varphi_2)$ .
- Again, Signal  $S_2$  (i.e.  $A_2 \cos(2\pi f_2 nT + \varphi_2)$ ) is subtracted from the previous residual signal ( $R_1$ ) to get the residual signal ( $R_2$ ).
- This process continues until the desired number of sinusoids,  $D$ , has been reached.
- In order to recalculate values for amplitudes and phases of the noise sinusoids the summation of the estimated noise signals (with  $A_k, \varphi_k$  as initial values) are fit into the minimization algorithm. This algorithm ensures minimization between the estimated noise signal components and the original data.

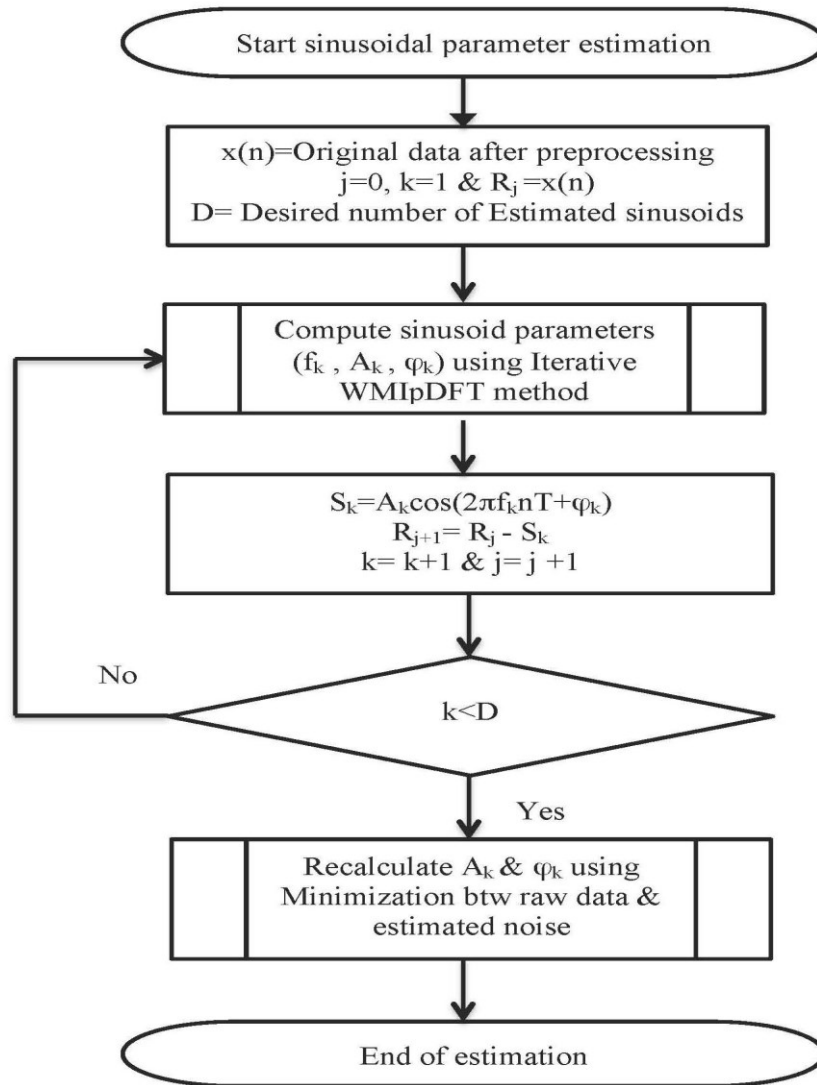


**Figure 5.1:** Flow chart of the proposed iterative WMIpDFT Algorithm where the pre-processed<sup>24</sup> data sequence is fed into the WMIpDFT in an iterative<sup>25</sup> manner until the desired number of sinusoids is estimated. The results are then fed into the minimization algorithm for further parameter optimization.

## 5.1 Iterative Approach for Signal Parameter Estimation

To estimate the parameters of low frequency sinusoidal noise signal components of ECT data, a WMIpDFT approach is adopted which utilizes the analytical formulas to

<sup>24</sup> Pre-processing stage include the removal of background and high frequency noises present in the collected ECT data

<sup>25</sup> Iteration is when each estimated sinusoid is subtracted from the residual data, which is initially set to the preprocessed data.

obtain the frequency, amplitude and phase of the signal component. However, the algorithm uses an iterative approach where each signal component's parameters (i.e. frequency, amplitude and phase) are estimated, and then the estimated signal is subtracted from residual data to compute the estimation of other consecutive signal components' parameters through an iterative approach.

The following block diagram in figure 5.2 shows the iterative approach of the proposed algorithm. The preprocessed data sequence,  $x(n)$ , for the first iteration, is passed through the WMlpDFT algorithm for sinusoidal parameter estimation. The estimated sinusoid sequence,  $S_k$ , where  $k$  is the sinusoidal component index, is subtracted from  $x(n)$  to get the residual data sequence,  $R_j$ , where  $j$  is the iteration index.  $x(n)$  becomes the obtained  $R_j$ , and is fed back into the WMlpDFT algorithm to estimate the subsequent sinusoidal components as desired.

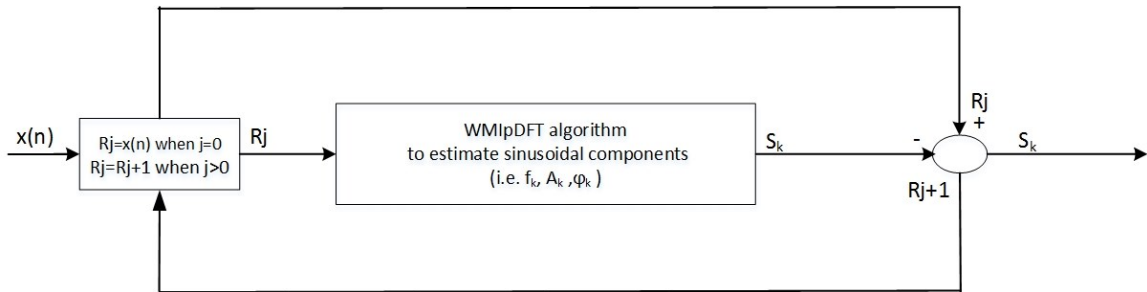


**Figure 5.2:** Block diagram of the iterative approach adopted by the proposed Iterative WMlpDFT Algorithm. Indexes  $j$  and  $k$  are set to 0 and 1 respectively, and the initial value of the residual signal sequence (i.e.  $R_0$ ) is  $x(n)$ .

The iteration approach will ensure less interference in the frequency spectrum by removing every estimated sinusoid. This will also lead to more estimation accuracy as frequency peaks, which have been effected by the spectrum interference, can be detected on the frequency spectrum.

## 5.2 Minimization to Improve Amplitude and Phase Estimations

The purpose of the proposed algorithm is to estimate the sinusoidal noise, and reduce its effect on the ECT data by subtracting it from the data. Therefore, in order to reduce the signal noise effect, it is vital to minimize, at the estimated frequencies, the residual signal obtained from the subtraction of the estimated noise signal components and the ECT data sequence. Consequently, solving the following least squares problem in Equation 5.1 for amplitude and phases of the estimated noise signal component can minimize the residual signal.

$$Residual(\hat{A}_k, \hat{\varphi}_k) = \arg \min \left| x(n) - \sum_{k=1}^K A_k \cos(2\pi f_k nT + \varphi_k) \right|^2 \quad (5.1)$$

In Equation 5.1,  $x(n)$  is the preprocessed ECT data sequence, and  $n$  is sample index, which is from 0 to  $N$  (number of samples). In addition, previously estimated  $A_k$  and  $\varphi_k$  are used as initial values to the algorithm. The above equation can be solved by means of a gradient algorithm where the local minimum of the function is searched with directions provided by the gradient of the function from the initial point. The important condition for minimization of the Residual ( $A_k, \varphi_k$ ) is to set the gradient vector of the function to 0 in Equation 5.2. Figure 5.3 shows the flow chart for the minimization algorithm.

$$\nabla Residual(A_k, \varphi_k) = 0 \quad (5.2)$$

The expressions for  $\frac{\partial Residual}{\partial A_k}$  and  $\frac{\partial Residual}{\partial \varphi_k}$  are given in Equations 5.3 and 5.4 as:

$$\begin{aligned} \frac{\partial Residual}{\partial A_k} &= \sum_{n=0}^{N-1} -2x(n) \cos(2\pi f_k nT + \varphi_k) \\ &\quad * \left( \sum_{n=0}^{N-1} (x(n) - \sum_{\substack{l=1 \\ l \neq k}}^L \cos(2\pi f_l nT + \varphi_l)) \right) \end{aligned} \quad (5.3)$$

$$\begin{aligned} \frac{\partial Residual}{\partial \varphi_k} &= \sum_{n=0}^{N-1} 2A_k x(n) \sin(2\pi f_k nT + \varphi_k) \\ &\quad * \left( \sum_{n=0}^{N-1} (x(n) - \sum_{\substack{l=1 \\ l \neq k}}^L \cos(2\pi f_l nT + \varphi_l)) \right) \end{aligned} \quad (5.4)$$

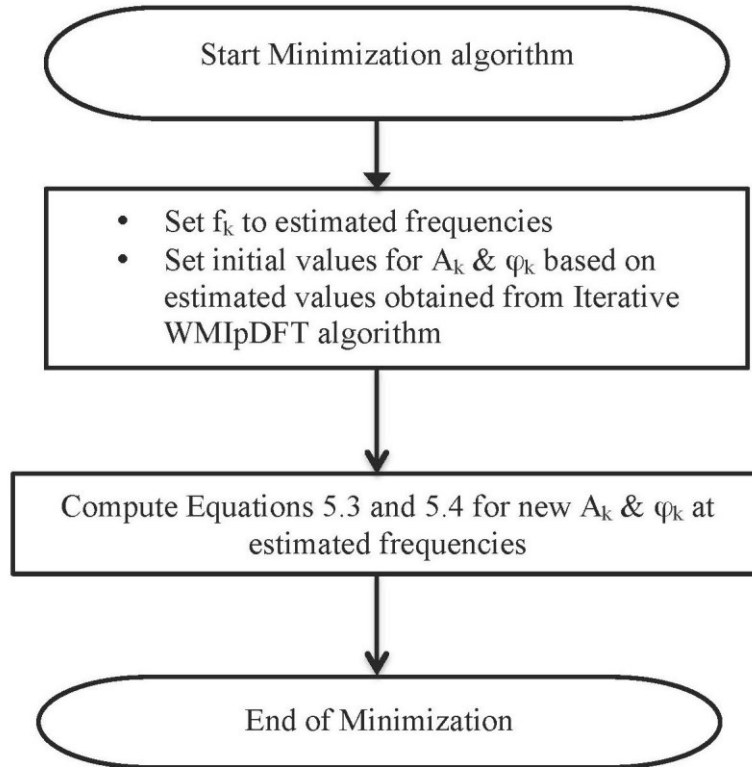


Figure 5.3: The flow chart of the minimization algorithm for improvement of estimated phase and amplitude parameters for each frequency component of estimated sinusoidal noise through minimization of the ECT data sequence and estimated sinusoidal noise.

## Chapter 6: Implementation and Results

The proposed Iterative WMIpDFT algorithm is implemented using MATLAB. The algorithm is applied to the ECT data collected from the steam generator tubes of a CANDU nuclear plant to estimate and reduce low frequency sinusoidal noise. It is assumed that there are a static number of sinusoidal components in the collected data, and the multi-frequency ECT data is corrupted by random additive white Gaussian noise with zero mean and  $\sigma^2$  standard deviation.

To collect data during the inspection of steam generator tubes, Frequencies 120kHz and 240 kHz were used, and the data was sampled at 1000 per second. Moreover, the test probe is moved at 18 inches/sec, which gives 55-56 samples per inch. Therefore, the data corresponding to each tube with the length of approximately 496-497 inches has 27500 to 27700 samples. It has been assumed that the data is collected at a constant speed by the probe throughout the inspection of the tubes.

The algorithm is only applied to the regions where the support plate responses are not present. The algorithm is used to estimate two, three, and four frequencies from the collected data. Furthermore, the reduction of only similar frequencies throughout the data is considered. Moreover, the reduction of the estimated low frequency sinusoidal noise is analyzed based on root mean square (RMS) and peak to average (PAR).

The preprocessing of the collected data, implementation of the proposed algorithm, presentation, analysis, and comparison of the results are exhibited in the following sections.

## 6.1 Preprocessing of Collected ECT Data

Before estimating the parameters of the sinusoidal noise from the horizontal and vertical components of the collected data using the Iterative WMIPDFT algorithm, the collected data needs to be removed of any background and high frequency noise sources, and gets segmented into the regions of interest for sinusoidal noise estimation. The preprocessing stages are depicted in Figure 6.1. The pre-processing has been designed by CNL to extract important information. Furthermore, the preprocessing steps prepare the data for the estimation of sinusoidal noise.

All the ECT data used in this research have been collected by CNL during the inspection of the SG tubes. Moreover, the results presented in this thesis are all obtained from the data for Tube 1.

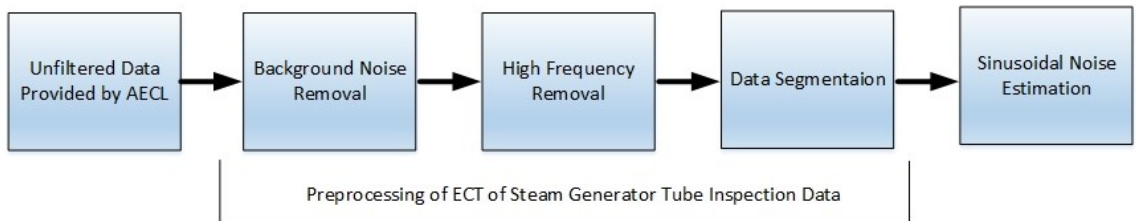


**Figure 6.1:** The preprocessing stages of the collected ECT data

### 6.1.1 Background Noise Reduction

The collected ECT data contains unimportant background variation in the time domain of the horizontal and vertical components as shown in the top plots in Figures 6.2 and 6.3. This variation has a negative effect on the estimation of the sinusoidal noise, and therefore, needs to be addressed. In order to remove the low-frequency background signal from the data, the data is fitted using a second order polynomial in Equation 6.1 by means of least squares techniques at every 256 data points to keep the linear relationship

between the data points. In Equation 6.1,  $n$  is the degree of the polynomial, and  $p_n$  is the coefficient [40].

$$p(x) = p_1x^n + p_2x^{n-1} + \dots + p_nx + p_{n+1} \quad (6.1)$$

The fitted background signal is subtracted from the eddy current testing (ECT) data to reduce the background noise. The results of the vertical and horizontal components in the time domain are shown in the bottom plots in Figures 6.2 and 6.3 respectively.

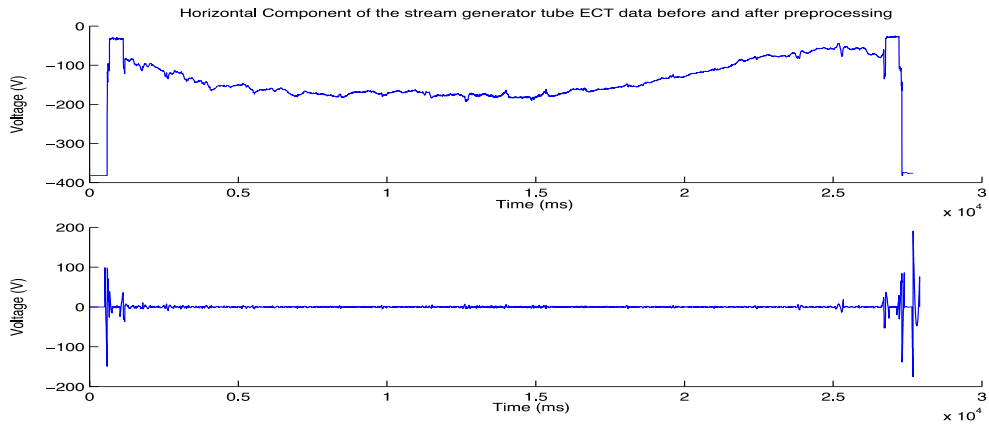


**Figure 6.2:** Horizontal Component of impedance plane before (top plot) and after (bottom plot) removal of background and high frequency noise from Tube 1

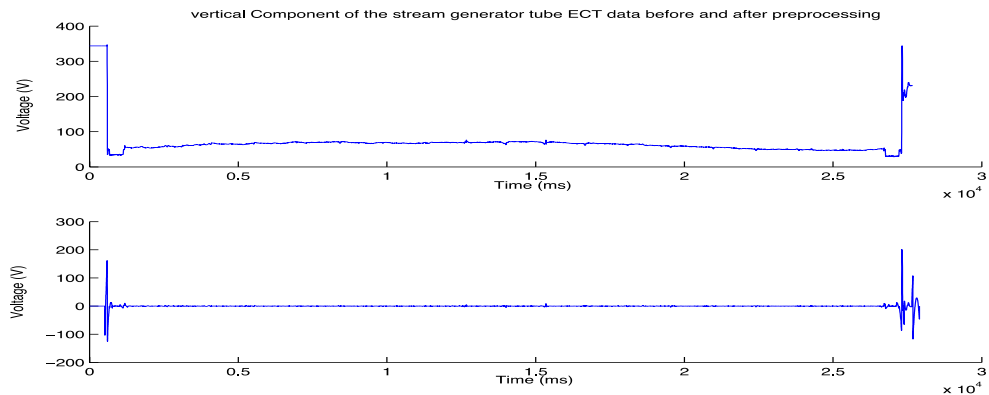


**Figure 6.3:** Vertical Component of impedance plane before (top plot) and after (bottom plot) removal of background and high frequency noise from Tube 1

### 6.1.2 High Frequency Noise Reduction

The ECT data has also high frequency noise that appears over the data as shown in the top plot of Figure 6.4. The high frequency noise can be removed using the average moving filter as shown in Equation 6.2 where  $x[i]$  is the input,  $y[i]$  is the output, and  $M$  is the number of points in the moving average [40].

$$y[i] = \frac{1}{M} \sum_{j=0}^{M-1} x[i + j] \quad (6.2)$$

The number of points is chosen to be 3 points to avoid any distortion to the flaw signals. The bottom plot in Figure 6.4 shows the high frequency noise over the vertical component of the data before and after the removal.

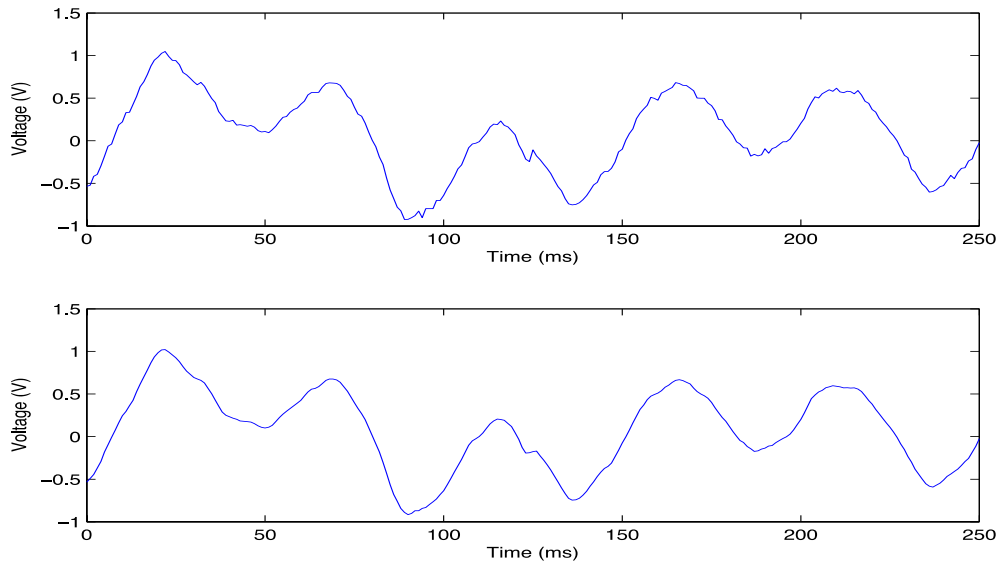


**Figure 6.4:** The high frequency noise riding on the vertical component (top plot) and the vertical component without the high frequency (bottom plot) from Tube 1

### 6.1.3 ECT Data Segmentation

After removing the background and high frequency noises on the collected ECT data, the data needs to be segmented into the regions that the proposed algorithm will be applied to.

The tubes, as shown in Figure 6.5, consist of three main regions: Cold, U-Bend, and Hot regions. The tubes are further segmented into 18 FS regions of 1000 points each. These free span regions are the regions of interest where the sinusoidal noise is estimated. The free span regions are between the tube TSPs that hold the tubes as shown in Figure 6.5. The length of the FS regions, i.e. 1000 points, are chosen to avoid the TSPs in order to get more accurate sinusoidal noise estimation. As a result, the free span regions are between the TSP regions where the TSPs reside.

The proposed algorithm can also be applied to the support plate regions; however, the TSP response must be suppressed by means of frequency mixing techniques so it does not impact the accuracy of the sinusoidal noise estimation.

Moreover, the regions at both ends of the tubes are also removed, and not considered for sinusoidal noise estimation as these regions contain high amplitude signals due to entry and exit of the test probes into the tubes as well as the tube sheets at the bottom of the steam generator.

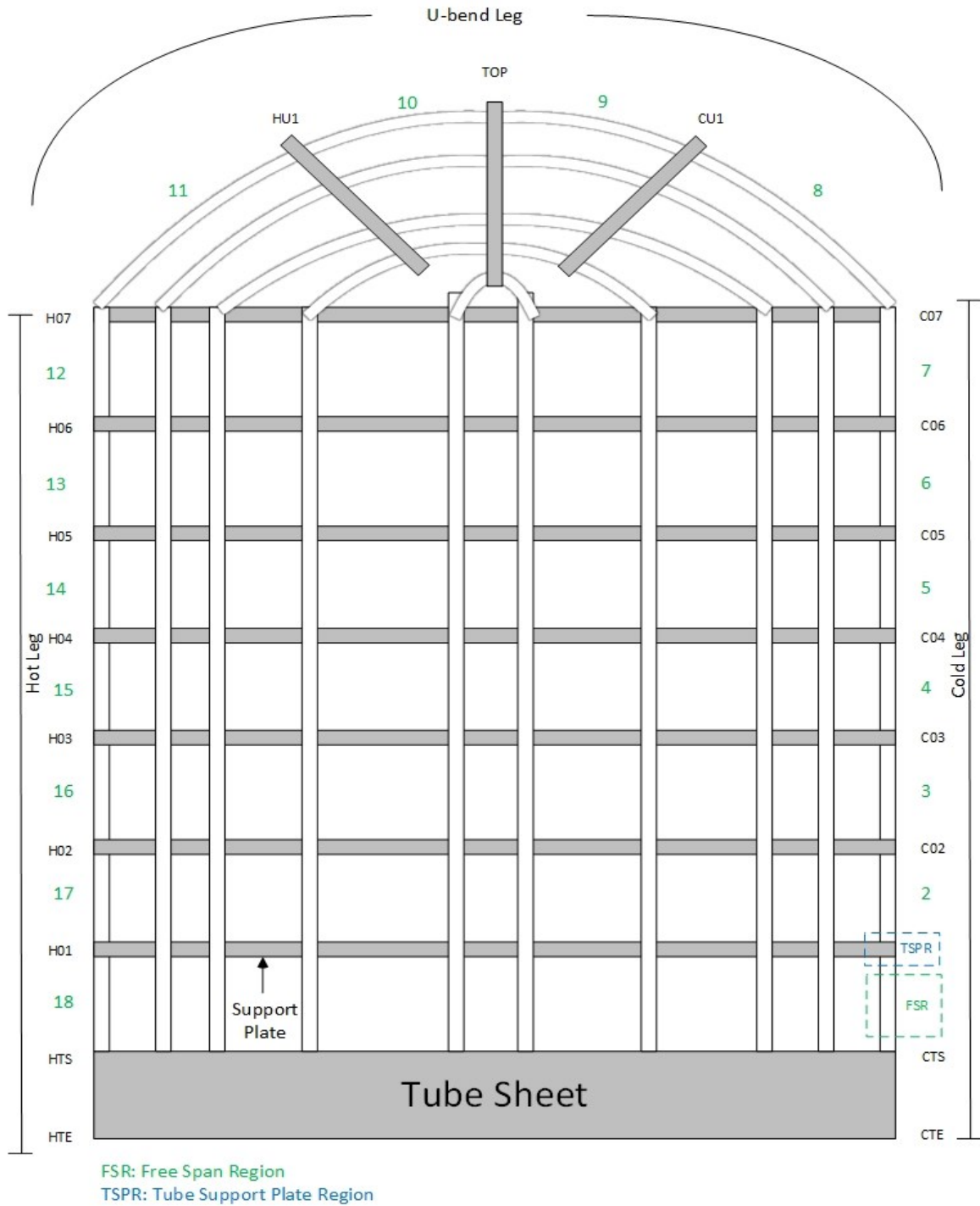


**Figure 6.5:** Tubes inside a steam generator with free span and TSP regions indicated adapted from [2]<sup>26</sup> with written permission.

<sup>26</sup> The figure has been reproduced from the presentation given by Richard Lakhan from CNL at Carleton University in 2012

## 6.2 Implementation of the Proposed Algorithm

### 6.2.1 Regions of Interest for Implementation of the Algorithm

The proposed algorithm is applied to the span free regions between the tube support plates (TSP) in this study where there is less distortion and noises from the TSPs. The algorithm could potentially be applied to the TSP regions where the TSP response is suppressed. However, in this study, the TSP regions were not considered and the sinusoidal noise was not estimated in that region due to the presence of TSPs.

The flaws in the tubes of the steam generator in question are mostly outer diameter (OD) flaws, which appear as peaks on the vertical component in the time domain. Therefore, it is important to reduce the sinusoidal noise from the vertical component data by applying the Iterative WMIpDFT algorithm. By examining peaks on the horizontal component, inner diameter (ID) flaws can be detected if any exists.

Moreover, since the OD flaws are of concern, the algorithm is only applied to the vertical component to be examined in the time domain.

Figure 6.6 shows ideal outer and inner flaws in the impedance plane for the absolute test mode at an excitation frequency where shallow ID and OD flaws are separated by 90 degrees. The flaw in the middle is a wall-through hole. In general, dent and external magnetic signals appear to the left side of the balance point, and ID flaw and defect signals appear to the right of the balance point.<sup>27</sup>

---

<sup>27</sup> Balance point is where the probe is in proximity of the defect free test material.

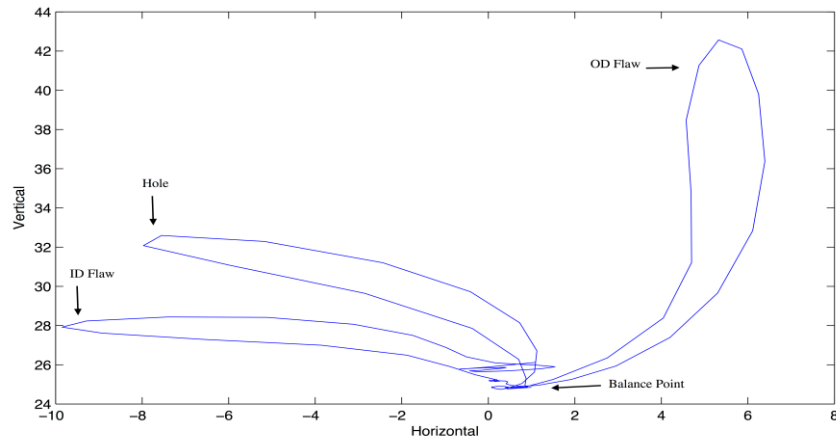


**Figure 6.6:** Flaw signals from ECT data with outer diameter flaw labeled as OD and inner diameter flaw labeled as ID along with other flaws such hole<sup>28</sup>

## 6.2.2 Value Selection for the Parameters of the Algorithm

### 6.2.2.1 Variable J for Number of Interpolation Points

At very low frequencies, the algorithm with higher number of interpolation points such as 7 points performs better since spectral interference contribution is great. However, with a higher number of interpolation points, as the frequency increases the spectral interference contribution lowers, and uncertainty in estimation increases. Therefore, lower number of interpolation points need to be used, and based on the observation of number of interpolation points in [37], the most suitable values for J are 1 and 2, which correspond to 3 and 5 interpolation points.

In order to choose the suitable interpolation points for the proposed algorithm, the algorithm has been applied to the span free regions of Tube 1. The comparison between the two number of interpolation points has been performed by means of root mean square (RMS) values, given in Equation 6.3, of the residual data obtained by subtracting the

---

<sup>28</sup> The plot is generated from the data provided by CNL

ECT data of each segment from the noise signal of 3 sinusoids estimated by the proposed algorithm from each segment. Table 6.1 shows the result of the comparison. In Equation 6.3,  $X(i)$  is the data point,  $m$  is the average of the segment, and  $N$  is the segment length.

$$RMS = \sqrt{\frac{\sum_{i=1}^N (X(i) - m)^2}{N}} \quad (6.3)$$

**Table 6.1:** RMS of free span segments in Tube 1 after subtraction of estimated noise signal of 3 sinusoids for H=2 and different values of J. Column 3 shows lower RMS values.

Region	Segment	J=1	J=2
<i>Cold</i>	<b>1</b>	0.2018	0.272
	<b>2</b>	0.3726	0.4211
	<b>3</b>	0.1302	0.1684
	<b>4</b>	0.1563	0.2107
	<b>5</b>	0.1488	0.2089
	<b>6</b>	0.358	0.4939
	<b>7</b>	0.2448	0.275
<i>U-Bend</i>	<b>8</b>	0.193	0.221
	<b>9</b>	0.2642	0.3066
	<b>10</b>	0.24	0.324
	<b>11</b>	0.2383	0.3003
<i>Hot</i>	<b>12</b>	0.2109	0.2688
	<b>13</b>	0.2537	0.2744
	<b>14</b>	0.237	0.2899
	<b>15</b>	0.2341	0.3279
	<b>16</b>	0.3236	0.3979
	<b>17</b>	0.5118	0.595
	<b>18</b>	0.3774	0.6366

The comparison shows that 3 interpolation points leads to a better root mean square on the ECT data than the 5-point interpolation.

### 6.2.2.2 Window Order H

As mentioned in Section 4.3.4.2, the window order H must be chosen low enough to avoid uncertainty in parameter estimation. Therefore, a value of 2 has been chosen for H. The effectiveness of this choice is evident when the noise signal of 2 or 3 sinusoids, estimated using the proposed algorithm, is subtracted from the FS segments of the ECT data. By taking the RMS of the residual data from the above subtraction, Table 6.2 shows that H=2 leads to a better RMS for almost all segments in Tube 1 compared to H=3 or 4.

**Table 6.2:** RMS of free span segments after subtraction of estimated noise signal of 3 sinusoids for J=1 (i.e. 3 Interpolation Points) and different values of H. Column 3 shows lower RMS values.

Region	Segment	H=2	H=3	H=4
<i>Cold</i>	<b>1</b>	0.2018	0.2281	0.2417
	<b>2</b>	0.3726	0.3824	0.4025
	<b>3</b>	0.1302	0.1334	0.1362
	<b>4</b>	0.1563	0.161	0.1743
	<b>5</b>	0.1488	0.1487	0.1543
	<b>6</b>	0.358	0.3455	0.348
	<b>7</b>	0.2448	0.2508	0.2521
<i>U-Bend</i>	<b>8</b>	0.193	0.2061	0.2305
	<b>9</b>	0.2642	0.3046	0.3004
	<b>10</b>	0.24	0.2511	0.2738
	<b>11</b>	0.2383	0.234	0.2281
<i>Hot</i>	<b>12</b>	0.2109	0.2267	0.2381
	<b>13</b>	0.2537	0.2948	0.2895
	<b>14</b>	0.237	0.2422	0.2447
	<b>15</b>	0.2341	0.2535	0.3023
	<b>16</b>	0.3236	0.3513	0.3998
	<b>17</b>	0.5118	0.5929	0.5968
	<b>18</b>	0.3774	0.3959	0.464

### 6.2.3 Iteration Effect of Proposed Algorithm on Frequency estimation

The proposed Iterative WMIpDFT algorithm is implemented to estimate sinusoidal parameters (frequency, amplitude and phase) in an iterative manner. The iterative approach is depicted in Figure 6.7 below.

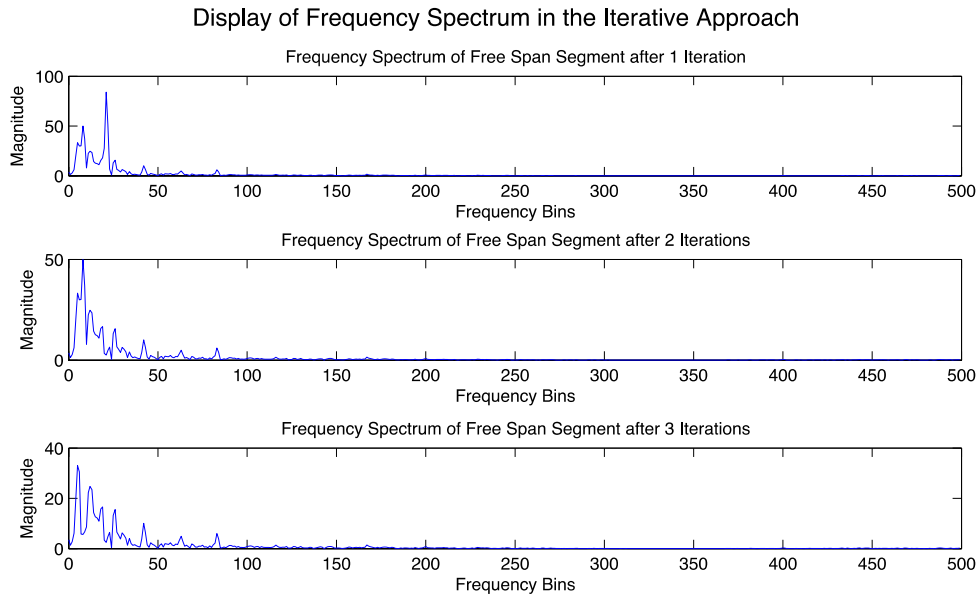


**Figure 6.7:** Iteration approach of the proposed Iterative WMIpDFT algorithm

Even though the performance of the non-iterative WMIpDFT algorithm is similar to that of the iterative approach in most segments, in two segments of Tube 1, the iterative WMIpDFT algorithm leads to better estimation of parameters. The comparison of the non-iterative and iterative approach for Segments 13 and 15 is shown in Table 6.3 by means of RMS, where the noise signal of 4 sinusoids are estimated by the proposed algorithm.

Table 6.3 shows that for Segment 13, the two approaches estimated different values for the fourth frequency in blue. It shows that the iterative approach leads to a lower RMS even though the improvement is not striking. However, in Segment 15, where

the two algorithms estimate the third and fourth frequencies in grey differently, the improvement in RMS is more evident.

**Table 6.3:** Comparison of Performance of Iterative and Non-Iterative WMIpDFT Approaches on ECT Data (Frequencies are sorted based on amplitude)

		Segment 13		Segment 15	
		Non-Iterative	Iterative	Non-Iterative	Iterative
<b>Frequency</b>	1	21.0054	21.0054	20.9724	20.9724
	2	12.4115	12.4115	5.9261	5.9261
	3	7.9479	7.9479	7.8664	8.1314
	4	17.0021	5.8896	12.6252	3.8325
<b>Amplitude</b>	1	0.3653	0.3653	0.3406	0.3406
	2	0.1231	0.1231	0.2492	0.2492
	3	0.1773	0.1773	0.1945	0.1700
	4	0.0857	0.1467	0.0870	0.1369
<b>Phase</b>	1	2.1803	2.1803	-2.7560	-2.7560
	2	-4.0495	-4.0495	0.4723	0.4723
	3	0.0626	0.0626	-1.2505	-2.0664
	4	1.2674	-0.5453	3.5678	0.5146
<b>RMS</b>		<b>0.2377</b>	<b>0.2365</b>	<b>0.2529</b>	<b>0.2321</b>

It can be concluded that aside from the factors such as the window order and number of interpolation points, the iterative nature could help with better parameter estimation since it could reveal frequencies that might be hidden by spectral leakage from adjacent frequency bins in the frequency domain.

### 6.3 The Proposed Algorithm's Estimation Results from Simulation

Before the proposed algorithm is applied to the experimental ECT collected data, a simulation was run to evaluate the accuracy of the estimation of the proposed algorithm. Two sinusoidal waveforms were inserted into the FS regions of the ECT data

of Tube 1 after removing three estimated sinusoids with highest amplitudes. Next, the proposed algorithm was applied to estimate the parameters of the inserted sinusoidal waveforms. The inserted discrete multi-frequency signal can be seen in Equation 6.4. The estimated parameters of the inserted sinusoids can be seen in Table 6.4.

$$x(m) = 5 \sin\left(2\pi(10.7)\frac{m}{M} + 2.2\right) + 3 \sin\left(2\pi(5.2)\frac{m}{M} + 1.7\right) \quad (6.4)$$

**Table 6.4:** Estimated parameters of the inserted sinusoids in Equation 6.4 in all FS segments.

Segment	Frequency (Hz)		Amplitude (V)		Phase (Radian)	
	F1	F2	A1	A2	P1	P2
1	10.688	5.123	5.004	2.979	2.254	1.780
2	10.688	5.117	4.958	2.960	2.259	1.742
3	10.705	5.124	4.973	2.992	2.183	1.741
4	10.701	5.113	5.019	3.008	2.199	1.784
5	10.701	5.113	4.962	2.962	2.194	1.780
6	10.687	5.091	5.042	3.053	2.236	1.861
7	10.710	5.119	4.938	2.932	2.168	1.759
8	10.691	5.118	5.030	2.967	2.229	1.771
9	10.718	5.122	5.000	2.872	2.159	1.742
10	10.702	5.109	5.040	3.034	2.187	1.794
11	10.700	5.130	5.031	3.085	2.203	1.728
12	10.701	5.122	4.947	2.898	2.203	1.742
13	10.709	5.119	4.916	2.785	2.180	1.746
14	10.703	5.117	4.942	3.040	2.185	1.752
15	10.703	5.115	4.951	2.930	2.181	1.764
16	10.700	5.110	4.993	2.842	2.179	1.806
17	10.678	5.113	4.848	3.073	2.278	1.759
18	10.705	5.122	4.977	2.992	2.203	1.833

The estimated parameters of the inserted sinusoids lead to very small residuals between the actual values of the parameters, and those of the estimated parameters. The residual can be calculated by the root mean square error (RMSE) is defined as the average of the squares of the deviations which are the difference between the actual value and what is estimated. In particular, the RMSE values for Frequencies 1 and 2 are 0.0097 and 0.0863 respectively.

The low RMSE values are good indications of good estimations that the proposed algorithm performs when the signal is assumingly corrupted by a random noise with zero mean and variance  $\sigma^2$  is added to the signal.

In the following sections, the proposed algorithm is applied to FS regions of the experimental ECT collected from SG tubes.

## **6.4 The Proposed Algorithm's Results on Free Span Regions**

### **6.4.1 Estimated Parameters of Sinusoidal Noise**

The sinusoidal noise signals from the vertical component of the eddy current data for Tube 1 in the steam generator have been obtained from the parameters estimated by the proposed algorithm in the following tables. The following Tables 6.5 and 6.6 show the estimation of parameters acquired from the vertical component of the eddy ECT in the span-free region of 1000 when  $H=2$  and  $J=1$  (i.e. three interpolation points) are used for the Iterative WMIpDFT algorithm. Again, the algorithm is only applied to the vertical component where most of the flaws reside.

**Table 6.5:** 4 sinusoidal components of the noise signal in the free span region of 1000 points with the highest amplitudes in the frequency domain. The table is sorted based on the amplitude.

Segment	Frequency (Hz)				Amplitude (V)				Phase (Radian)			
	F1	F2	F3	F4	A1	A2	A3	A4	P1	P2	P3	P4
1	21.19	8.08	5.19	12.02	0.33	0.22	0.16	0.13	2.75	3.15	0.56	2.75
2	21.33	8.28	25.02	9.47	0.33	0.31	0.16	0.12	0.77	1.10	0.23	0.75
3	21.09	8.41	16.92	4.44	0.26	0.13	0.08	0.08	0.59	0.87	2.68	3.85
4	21.03	8.24	12.30	4.33	0.29	0.17	0.14	0.12	2.74	1.03	1.93	2.07
5	21.12	12.26	8.51	16.89	0.31	0.15	0.10	0.07	1.57	0.90	4.39	0.16
6	8.24	12.30	21.03	4.33	0.42	0.34	0.30	0.28	3.03	2.49	1.53	1.90
7	20.98	8.32	4.09	24.05	0.27	0.18	0.17	0.15	2.27	2.72	3.19	0.57
8	21.13	7.02	24.17	3.57	0.16	0.11	0.09	0.08	1.10	0.88	0.93	1.65
9	21.35	25.62	7.78	12.31	0.27	0.19	0.18	0.12	2.15	0.87	0.16	3.02
10	21.33	25.78	7.11	8.98	0.29	0.25	0.22	0.15	0.30	1.46	2.03	0.53
11	8.21	21.05	4.27	25.53	0.34	0.29	0.22	0.17	3.43	1.75	0.13	1.21
12	21.11	8.91	3.72	11.17	0.25	0.18	0.12	0.10	2.31	3.39	2.48	1.11
13	21.01	7.95	5.89	12.41	0.37	0.18	0.15	0.12	2.18	0.06	0.55	4.05
14	20.96	12.19	4.22	6.19	0.39	0.22	0.14	0.11	0.10	0.09	0.83	2.43
15	20.97	5.93	8.13	3.83	0.34	0.25	0.17	0.14	2.76	0.47	2.07	0.52
16	21.06	8.82	12.12	16.25	0.22	0.21	0.19	0.17	1.39	0.49	2.79	2.11
17	7.51	17.14	21.90	14.23	0.36	0.33	0.31	1.06	3.84	2.92	1.06	3.09
18	4.95	8.10	20.86	17.15	0.53	0.46	0.43	0.21	0.83	2.19	0.64	1.13

In Table 6.5, the estimated parameters for 4 sinusoidal components are presented.

It can be seen that there are two frequency estimations that are similar among most of the free span segments. This is more evident in Table 6.6 where the two frequency estimations are shown. The similar frequencies indicate that the segments suffer from one or two sinusoidal noise sources.

**Table 6.6:** 2 Estimated sinusoidal components of the noise signal, which are similar mostly among all the segments in Tube 1

Region	Segment	Frequency (Hz)		Amplitude (V)		Phase (Radian)	
		F1	F2	A1	A2	P1	P2
Cold	1	21.190	8.082	0.334	0.223	-2.748	-3.153
	2	21.330	8.279	0.331	0.312	0.766	1.096
	3	21.087	8.407	0.256	0.132	-0.587	0.874
	4	21.032	8.240	0.286	0.165	-2.743	-1.034
	5	21.124	8.506	0.308	0.097	1.568	4.387
	6	21.298	8.249	0.297	0.416	-1.530	-3.030
	7	20.976	8.324	0.266	0.179	-2.269	-2.724
U-Bend	8	21.129	7.018	0.159	0.111	1.102	-0.881
	9	21.349	7.780	0.265	0.177	-2.153	0.161
	10	21.329	8.978	0.287	0.145	-0.299	-0.533
	11	21.046	8.212	0.292	0.337	-1.753	-3.425
Hot	12	21.107	8.910	0.247	0.180	-2.312	3.393
	13	21.005	7.948	0.365	0.177	2.180	0.063
	14	20.958	0.000	0.387	0.000	0.098	0.000
	15	20.972	8.131	0.341	0.170	-2.756	-2.066
	16	21.057	8.820	0.220	0.211	1.394	0.493
	17	21.904	7.509	0.316	0.363	1.064	3.836
	18	20.861	8.102	0.431	0.463	0.639	2.194

#### 6.4.2 Peak Removal to Improve Estimation

Peak removal is applied to improve sinusoidal noise estimation by replacing the peak with the average of the segment data points. After the peak removal the sinusoidal noise parameters are estimated. In the study, the peaks whose the PAR value is above 6 dB are considered flaws.

As shown in Figure 6.8, in Segments 2 and 17 of the free span regions, the potential flaw peaks have been removed, and the estimation of parameters and improvement in terms of RMS are shown in the Table 6.7.

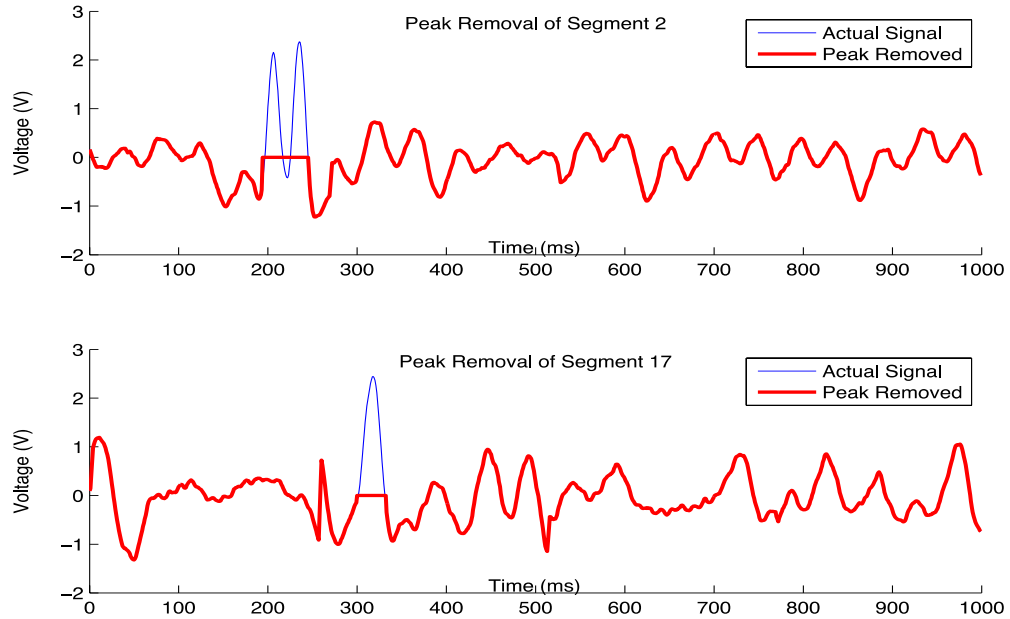


**Figure 6.8:** The top plot shows the peak removal of Segment 2 along with the original signal, and the bottom plot shows the same for Segment 17 in Tube 1

**Table 6.7:** Parameter estimation of segments in Tube 1 after removal of flaw signal

Segment	Flaw Removal	Frequency (Hz)		Amplitude (V)		Phase (Radian)		RMS
		F1	F2	A1	A2	P1	P2	
2	Before	21.330	8.279	0.331	0.312	0.766	1.096	0.385
	After	21.238	8.197	0.331	0.259	1.127	1.497	0.384
17	Before	21.904	7.509	0.316	0.363	1.064	3.836	0.562
	After	20.989	7.764	0.301	0.258	-2.173	2.763	0.486

### 6.4.3 Root Mean Square (RMS) Improvement

One of the parameters to assess the improvement of the filtered segment data after applying the proposed Iterative WMIpDFT algorithm is to use the RMS of the data before and after the filtering. RMS shows how the noise level before and after the reduction of sinusoidal noise. It is clearly shown in Table 6.8 that there is improvement in RMS after the algorithm applied.

**Table 6.8:** The root mean square (RMS) of each segment in Tube 1 after applying the Iterative WMIpDFT algorithm. This can be seen in Column 4.

<i>Segment</i>	<b>Before Sinusoidal noise reduction</b>	<b>After Sinusoidal Noise Reduction</b>	
	<i>Original RMS</i>	<i>RMS</i>	<i>RMS Improvement in Percentage</i>
<b>1</b>	0.3261	0.1998	38.73%
<b>2</b>	0.4846	0.3836	20.84%
<b>3</b>	0.2474	0.1383	44.10%
<b>4</b>	0.2720	0.1851	31.95%
<b>5</b>	0.2945	0.1669	43.33%
<b>6</b>	0.4892	0.3874	20.81%
<b>7</b>	0.3386	0.2637	22.12%
<b>8</b>	0.2449	0.1998	18.42%
<b>9</b>	0.3402	0.2856	16.05%
<b>10</b>	0.3665	0.3028	17.38%
<b>11</b>	0.3658	0.2625	28.24%
<b>12</b>	0.3028	0.2279	24.74%
<b>13</b>	0.3613	0.2538	29.75%
<b>14</b>	0.3840	0.2645	31.12%
<b>15</b>	0.3228	0.2238	30.67%
<b>16</b>	0.3791	0.3448	9.05%
<b>17</b>	0.5439	0.4857	10.70%
<b>18</b>	0.5350	0.4261	20.36%

Applying minimization, which is discussed in Section 6.3.5, can further reduce the RMS. Appendix A shows the estimated sinusoidal noise parameters with 2 sinusoids and corresponding RMS improvement for other investigated tubes. Moreover, the more estimated sinusoidal noise is removed from the segment data the RMS values of the segments become lower.

#### 6.4.4 Peak To Average Ratio (PAR) Comparison

Another parameter for evaluating the improvement of the filtered data and minimal effect of reducing the sinusoidal noise on the potential peak flaws is the PAR. PAR shows how extreme flaw peaks are in the segment. The peak-to-average ratio is calculated by dividing the peak height in the segment of interest to the RMS of the same segment (i.e.  $\frac{Peak\ Value}{RMS}$ ).

Table 6.9 shows the effect of sinusoidal noise reduction on the non-flaw and potential flaw peaks in Segments 2 and 17. Figures 6.9 show the peak locations in Segments 2 and 17.

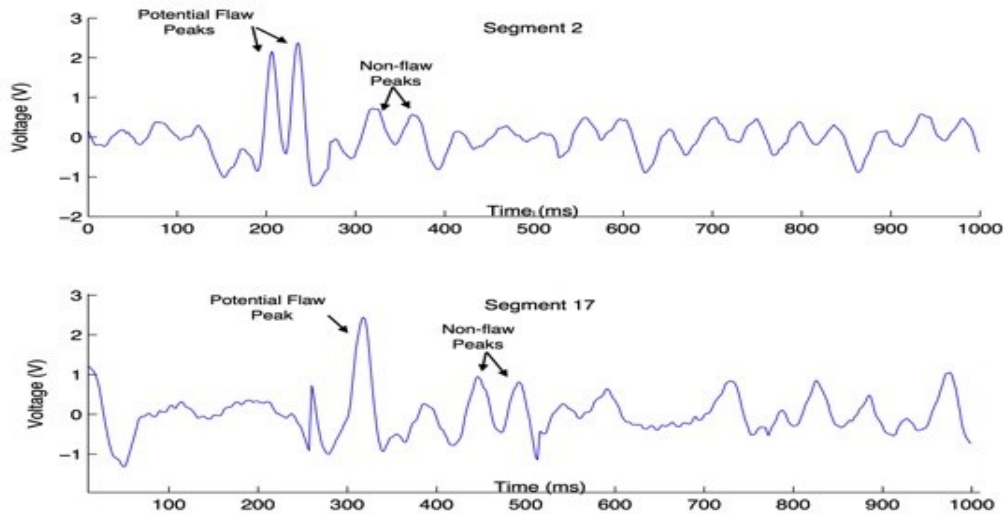


**Figure 6.9:** Potential flaw and non-flaw peaks for Segments 2 and 17 in Tube 1

**Table 6.9:** Peak-to-Average ratio (PAR) of the non-flaw & potential flaw peaks in Segments 2 & 17 in Tube 1

Segment	Peak to Average Ratio (dB) Before Sinusoidal Noise Reduction				Peak to Average Ratio (dB) After Sinusoidal Noise Reduction			
	<i>Potential Flaw Peaks</i>		<i>Non-flaw Peaks</i>		<i>Potential Flaw Peaks</i>		<i>Non-flaw Peaks</i>	
	1	2	3	4	1	2	3	4
<b>2</b>	6.485	6.901	1.744	0.732	7.546	7.384	0.229	-2.445
<b>17</b>	6.524	N/A	2.417	1.750	6.764	N/A	0.018	0.940

From Table 6.9, it can be seen that the PAR has increased in all the potential flaw peaks, which can effectively increase detection of flaws. On the other hand, the peaks that are not considered flaws have their PAR decreased drastically. This again shows the reduction of noise in the segment.

Additionally, the reduction of more estimated sinusoidal noise does not lead to the improvement in PAR values. This is because the estimated noise signal with more sinusoids such as 3 or more leads to distortion and loss of information in flaw signals. This has been shown in Table 6.10 for Segments 2 and 7.

**Table 6.10:** Peak-to-average ratio (PAR) when 2 and 3 sinusoids used to filter Tube 1 data

Segment	Peak to Average Ratio (PAR) Before Applying Proposed Algorithm		Peak to Average Ratio (dB) After Applying Proposed Algorithm			
			<i>2 Sinusoids</i>		<i>3 Sinusoids</i>	
	Peak 1	Peak 2	Peak 1	Peak 2	Peak 1	Peak 2
<b>2</b>	6.486	6.902	7.658	7.437	7.592	6.969
<b>17</b>	6.525	N/A	5.312	N/A	4.536	N/A

## 6.4.5 Minimization Effect

### 6.4.5.1 Using Each Segment's Estimated Sinusoidal Frequencies

The minimization part of the algorithm is to re-estimate the amplitude and phase of the already estimated frequency of the sinusoidal noise signal. This will lead to better estimation of amplitude and phase parameters, and in turn improve noise reduction of the ECT data in terms of RMS. The following table 6.11 shows how the minimization can improve the RMS of the signal from the subtraction of the estimated noise signal of 2 sinusoids from the eddy current testing data.

**Table 6.11:** RMS results for all the segments in Tube 1 before and after the reduction of noise signal of 2 sinusoids as well as after minimization with their improvements with respect to original RMS in percentage. Lower RMS values shown in Column 6 due to minimization.

Segment	Before Sinusoidal noise reduction	After Sinusoidal Noise Reduction		After Minimization & Sinusoidal Noise Reduction	
	<i>Original RMS</i>	<i>RMS</i>	<i>RMS Improvement in Percentage</i>	<i>RMS</i>	<i>RMS Improvement in Percentage</i>
1	0.3261	0.1998	38.73%	0.1911	41.40%
2	0.4846	0.3836	20.84%	0.3808	21.42%
3	0.2474	0.1383	44.10%	0.1361	44.99%
4	0.2720	0.1851	31.95%	0.1805	33.64%
5	0.2945	0.1669	43.33%	0.1647	44.07%
6	0.4892	0.3874	20.81%	0.3772	22.89%
7	0.3386	0.2637	22.12%	0.2594	23.39%
8	0.2449	0.1998	18.42%	0.1885	23.03%
9	0.3402	0.2856	16.05%	0.2814	17.28%
10	0.3665	0.3028	17.38%	0.3005	18.01%
11	0.3658	0.2625	28.24%	0.2547	30.37%
12	0.3028	0.2279	24.74%	0.2236	26.16%
13	0.3613	0.2538	29.75%	0.2437	32.55%
14	0.3840	0.2645	31.12%	0.2637	31.33%
15	0.3228	0.2238	30.67%	0.2162	33.02%
16	0.3791	0.3448	9.05%	0.3315	12.56%
17	0.5439	0.4857	10.70%	0.5180	4.76%
18	0.5350	0.4261	20.36%	0.4048	24.34%

From Table 6.11, it can be realized that there is reduction in RMS in every segment except segment 17 since the peak is not removed for the estimation of the frequency parameter.

#### **6.4.5.2 Using Similar Estimated Sinusoidal Frequencies for Each Region**

Minimization can also be used when a similar estimated frequency parameter is reached among all the segments of Tube 1. By using minimization, the amplitude and phase parameters of the noise signal can be estimated for all the segments where the similar frequency is applied.

##### **6.4.5.2.1 Segment with Lowest Root Mean Square (RMS) in Each Region**

Since each region: hot, cold and U-bend, have different characteristics, a similar estimated frequency parameter could be selected for all the segments in each region. The selection is based on the frequency estimated from the segment where the initial RMS is the lowest. This is a good indication that the segment is less noisy, and therefore, the frequency estimation is more accurate.

Table 6.12 shows the result after using Segment 3's estimated frequencies on other segments in the same region to re-estimate the amplitude and phase of the sinusoidal noise signal from each segment to further improve the RMS value. Segment 3 for the cold region is chosen due to having the lowest RMS value.

**Table 6.12:** RMS results for the cold region before and after the reduction of noise signal of 2 sinusoids as well as after minimization, using Segment 3’s estimated frequencies, with their improvements with respect to original RMS in percentage

Region	Segment	<i>Before Sinusoidal noise reduction</i>	<i>After Sinusoidal Noise Reduction</i>		<i>Using Segment 13 Estimated Frequencies for Minimization &amp; Reduction</i>	
		Original RMS	RMS	RMS Improvement in Percentage	RMS	RMS Improvement in Percentage
Cold	1	0.3261	0.1998	38.73%	0.1832	43.82%
	2	0.4846	0.3836	20.84%	0.3811	21.36%
	3	0.2474	0.1383	44.10%	0.1361	44.99%
	4	0.272	0.1851	31.95%	0.1753	35.55%
	5	0.2945	0.1669	43.33%	0.1639	44.35%
	6	0.4892	0.3874	20.81%	0.3665	25.08%
	7	0.3386	0.2637	22.12%	0.2527	25.37%

Also, the same procedure, which was applied to the cold region, is applied to the hot region of the tube to try to improve the RMS value of the data with sinusoidal noise reduced. In this region, the estimated sinusoidal frequencies of Segment 15 are selected as similar sinusoidal frequencies among other segments in the region. Using Segment 15’s estimated sinusoidal frequencies through minimization, further RMS reduction can be achieved in all segments in the region except for Segment 12, as it is obvious in Table 6.13.

**Table 6.13:** RMS results for the hot region before and after the reduction of noise signal of 2 sinusoids as well as after minimization, using Segment 15’s estimated frequencies, with their improvements (reductions) with respect to original RMS in percentage.

Region	Segment	<i>Before Sinusoidal noise reduction</i>	<i>After Sinusoidal Noise Reduction</i>		<i>Using Segment 15 Estimated Frequencies for Minimization &amp; Reduction</i>	
		Original RMS	RMS	RMS Improvement in Percentage	RMS	RMS Improvement in Percentage
Hot	12	0.3028	0.2279	24.74%	0.2382	21.33%
	13	0.3613	0.2538	29.75%	0.2344	35.12%
	14	0.3840	0.2645	31.12%	0.2638	31.30%
	15	0.3228	0.2238	30.67%	0.2162	33.02%
	16	0.3791	0.3448	9.05%	0.3159	16.67%
	17	0.5439	0.4857	10.70%	0.4746	12.74%
	18	0.5350	0.4261	20.36%	0.4069	23.94%

#### 6.4.5.2.2 Average of Frequencies in Each Region

Another way to find similar sinusoidal estimated frequencies among other segments in the region is to average the frequencies estimated from all the segments in the same region. Averaging could also lead to further reduction in RMS, compared to the RMS after the reduction of the sinusoidal noise signal from the segment’s data. The following Table 6.14 shows the RMS results after applying the averaged estimated sinusoidal frequencies of each region to all the segments of the same region.

As shown in Table 6.14, there exists reduction in most of the segments of Tube 1 after re-estimating amplitude and phase of the sinusoidal noise signal using the averaged estimated sinusoidal frequencies through minimization. However, in the U-bend region, improvement (reduction) is not evident. This might be due to the characteristics of the U-bend region, and these characteristics make it difficult to find similar estimated frequencies among the region’s segments for further reduction.

**Table 6.14:** RMS before and after sinusoidal noise reduction after averaging estimated frequencies for each region

Region	Segment	Before Sinusoidal noise reduction	After Sinusoidal Noise Reduction		Averaging Estimated Frequencies for Minimization & Reduction	
		<i>Original RMS</i>	<i>RMS</i>	<i>RMS Improvement in Percentage</i>	<i>RMS</i>	<i>RMS Improvement in Percentage</i>
Cold	1	0.3261	0.1998	38.73%	0.1823	44.10%
	2	0.4846	0.3836	20.84%	0.3770	22.20%
	3	0.2474	0.1383	44.10%	0.1413	42.89%
	4	0.2720	0.1851	31.95%	0.1758	35.37%
	5	0.2945	0.1669	43.33%	0.1640	44.31%
	6	0.4892	0.3874	20.81%	0.3671	24.96%
	7	0.3386	0.2637	22.12%	0.2480	26.76%
U-Bend	8	0.2449	0.1998	18.42%	0.2016	17.68%
	9	0.3402	0.2856	16.05%	0.2654	21.99%
	10	0.3665	0.3028	17.38%	0.2967	19.05%
	11	0.3658	0.2625	28.24%	0.2689	26.49%
Hot	12	0.3028	0.2279	24.74%	0.2352	22.32%
	13	0.3613	0.2538	29.75%	0.2338	35.29%
	14	0.3840	0.2645	31.12%	0.2757	28.20%
	15	0.3228	0.2238	30.67%	0.2295	28.90%
	16	0.3791	0.3448	9.05%	0.3289	13.24%
	17	0.5439	0.4857	10.70%	0.4792	11.90%
	18	0.5350	0.4261	20.36%	0.4184	21.79%

## 6.5 Analysis of Estimated Sinusoidal Noise Reduction on Inserted Flaw Signals

In the previous sections, different aspects of the Iterative WMIpDFT were discussed, and the results from applying the algorithm to the collected eddy current testing (ECT) data were presented. Moreover, the effects of the noise reduction on the existing potential flaw peaks were analyzed.

From the results in the previous sections, it can be seen that the tube under examination has mainly two similar frequencies in the FS segments. One or two similar frequencies were observed among all the FS regions in the tubes that the algorithm was applied to. Furthermore, it is evident that even though the reduction of more sinusoids lead to a lower RMS, the flaw detection does not get improved as PAR decreases. This implies the flaw peaks get distorted. Additionally, it was concluded from the results that the iterative approach and minimization could improve frequency as well as amplitude and phase estimations.

In the following sections, the analysis of the reduction of the sinusoidal noise on the flaws that have been inserted in different parts of the FS regions of the same tube under examination (i.e. Tube 1) is discussed in both time domain and impedance plane.

### **6.5.1 Analysis of Inserted Flaws in Time Domain**

In the previous section, the analysis of the sinusoidal noise reduction was performed on potential flaw peaks whose peak-to-average ratio was greater than 6 dB such as the ones in Segments 2 and 17, which could have been caused by Manufacture's burnish mark (MBM) or loose parts.

However, in this section, an OD 40% deep fret, caused by flow-induced vibration, has been inserted, by the experts at CNL, at different free span regions in Tube 1 examined in the previous sections. The inserted flaws are shown in Figure 6.10.

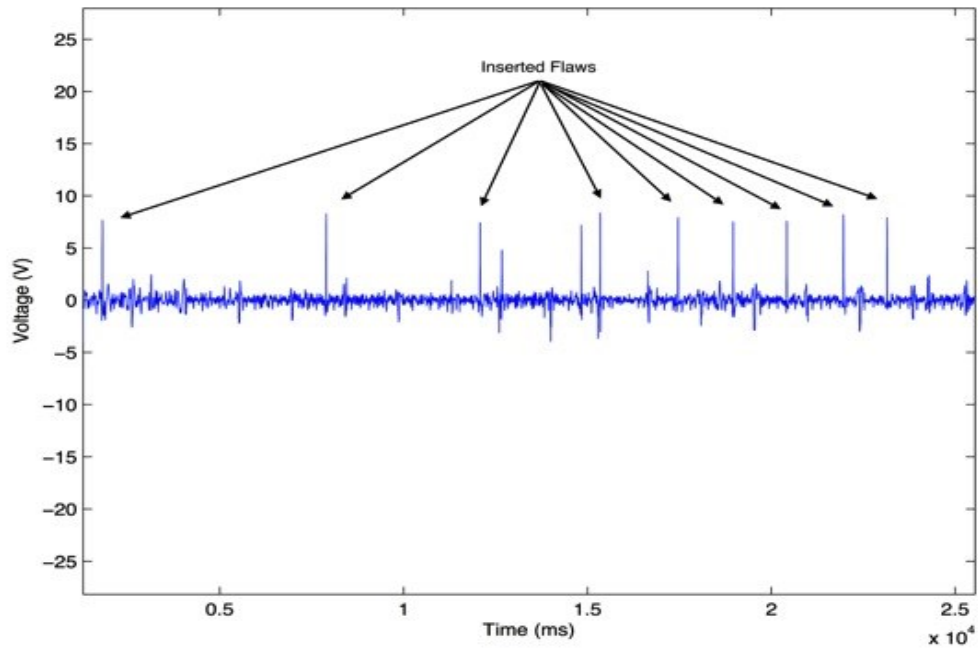


**Figure 6.10:** Inserted 40% outer diameter (OD) Flaws at different free span (FS) segments in Tube 1

The sinusoidal noise with 2 sinusoids is estimated using the proposed algorithm. The top plots in Figures 6.11 and 6.12 show the estimated sinusoidal noise along with the unfiltered signal of Segment 3 with the inserted flaw for the vertical and horizontal components respectively. Moreover, the bottom plots in Figures 6.11 and 6.12 show the sinusoidal noise reduced signals along with the unfiltered signal of the same segment for the vertical and horizontal components respectively.

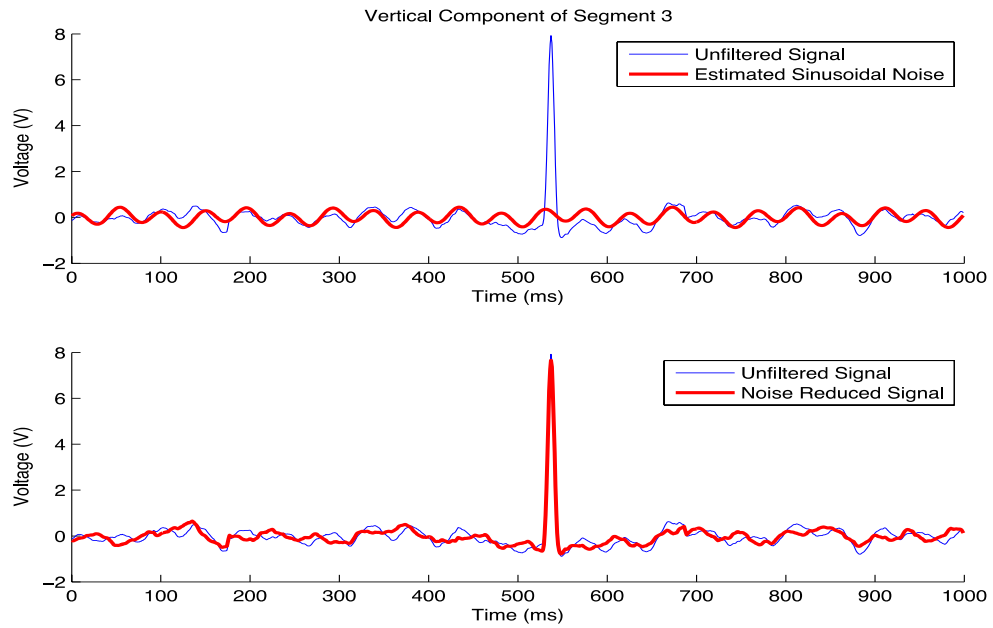


**Figure 6.11:** Estimated sinusoidal noise along with the unfiltered signal for Vertical Component of Segment 3

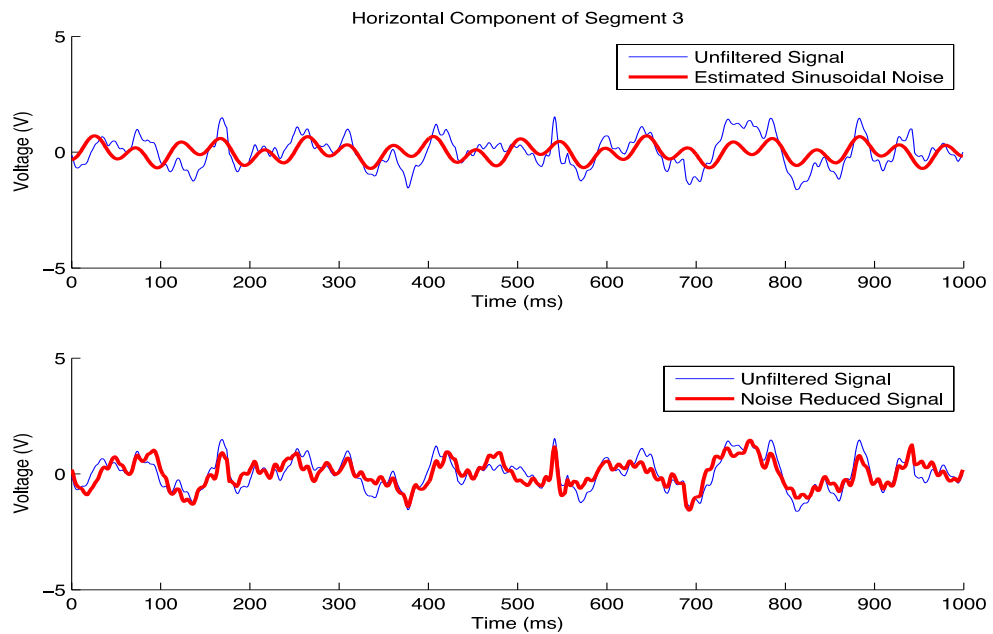


**Figure 6.12:** Estimated sinusoidal noise along with the unfiltered signal for Horizontal Component of Segment 3

The reduction of the sinusoidal noise after minimization, which re-estimates phase and amplitude, from the segments containing the flaws leads to the following RMS values shown in Table 6.15 for each flaw.

**Table 6.15:** RMS results before and after the reduction of noise signal of 2 sinusoids with minimization from segments containing inserted flaws in both horizontal and vertical components

<i>Segments With Inserted Flaws</i>	<i>Before Sinusoidal Noise Reduction</i>		<i>After Sinusoidal Noise Reduction</i>		<i>RMS Improvement in Percentage</i>	
	<i>Original RMS</i>		<i>RMS</i>			
	<i>Horizontal</i>	<i>Vertical</i>	<i>Horizontal</i>	<i>Vertical</i>	<i>Horizontal</i>	<i>Vertical</i>
3	0.6741	0.6809	0.5706	0.6378	15.36%	6.33%
4	0.6739	0.7163	0.5963	0.6786	11.52%	5.26%
5	0.5795	0.6674	0.563	0.624	2.85%	6.51%
6	0.8277	0.8027	0.658	0.7084	20.51%	11.75%
7	0.6979	0.7212	0.6896	0.6984	1.20%	3.16%
9	1.271	0.6869	1.1906	0.6552	6.33%	4.62%
11	1.0572	0.6976	1.031	0.6372	2.48%	8.65%
14	0.8959	0.7822	0.7488	0.6854	16.41%	12.37%
18	2.1789	0.8527	1.7363	0.7603	20.32%	10.84%

Table 6.15 reaffirms that the reduction of sinusoidal noise leads to lower RMS in both horizontal and vertical components. Moreover, Table 6.16 below indicates that the reduction of more estimated sinusoids can improve the RMS; however, the RMS improvement comes at the expense of having less PAR for the peak flaw as shown in Table 6.16 where the PAR decreases when the estimated sinusoidal noise consists of 3 sinusoids.

**Table 6.16:** RMS and PAR results before and after the reduction of noise signal of 2 sinusoids with minimization from segments containing inserted flaws in both horizontal and vertical components

Segment	Original RMS	RMS After Sinusoidal noise Reduction		Original PAR	PAR After Sinusoidal noise Reduction	
		2 Estimated Sinusoids	3 Estimated Sinusoids		2 Estimated Sinusoids	3 Estimated Sinusoids
3	0.6809	0.6378	0.6106	10.6559	10.7912	10.7956
4	0.7163	0.6786	0.6426	10.5782	10.6927	10.6452
5	0.6674	0.6240	0.6239	10.5514	10.7886	10.5138
6	0.8027	0.7084	0.6391	9.7275	9.9316	9.9891
7	0.7212	0.6984	0.6775	10.4176	10.5555	10.3654
9	0.6869	0.6552	0.6425	10.2080	10.2514	10.2038
11	0.6976	0.6372	0.6370	10.2736	10.5271	10.3119
14	0.7822	0.6854	0.6458	10.2596	10.5471	10.5410
18	0.8527	0.7603	0.7098	9.5525	9.9196	10.1177

Additionally, The PAR has increased in all segments after applying the proposed algorithm, which shows it could potentially increase the detection of flaws.

### 6.5.2 Analysis of Inserted Flaws in Impedance Plane

Although the analysis of peaks in the time domain is an important step towards identifying potential flaws, it is needed to analyze flaws in the impedance plane since the magnitude, and phase of the potential flaws could reveal vital information for characterization and classification. Therefore, in this section, the reduction of sinusoidal noise has been considered in the impedance plane to see if and how it could affect the potential flaws.

Figure 6.13 shows the 40% OD flaw that was inserted into different FS regions of Tube 1

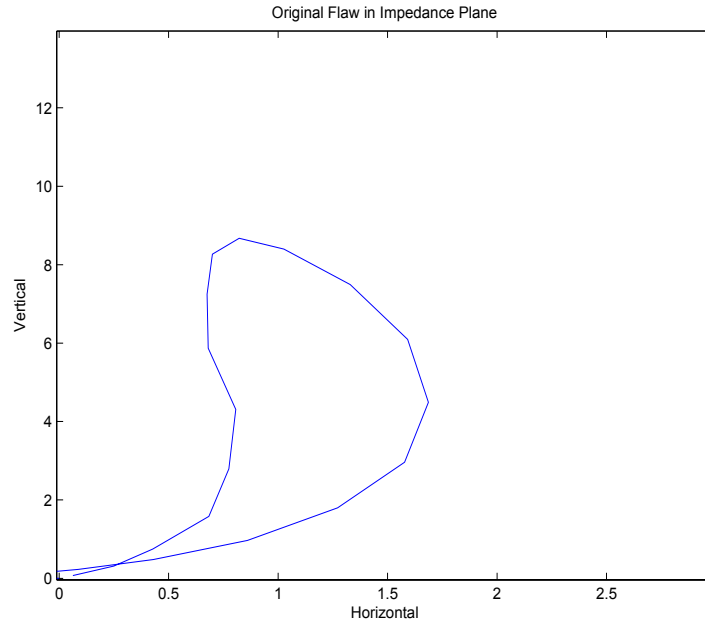


**Figure 6.13:** 40% OD flaw in impedance plane that has been inserted into different segments of the Tube 1

In this study, as both vertical and horizontal components experience the same sinusoidal noise, the same set of the frequencies estimated on the vertical component is applied to the horizontal component. However, the phase and amplitude of the sinusoids are re-estimated for the horizontal component using minimization.

The plots in Figure 6.14 show the 40% OD flaw before (in red) and after (in blue) insertion in Segments 3 and 9 of Tube 1. It can be clearly seen that the flaw has been distorted after insertion. Moreover, the flaws have been horizontally stretched which could potentially hinder flaw detection. Therefore, the proposed algorithm has been applied to see if the sinusoidal noise reduction can help reduce the distortion, and improve detection.

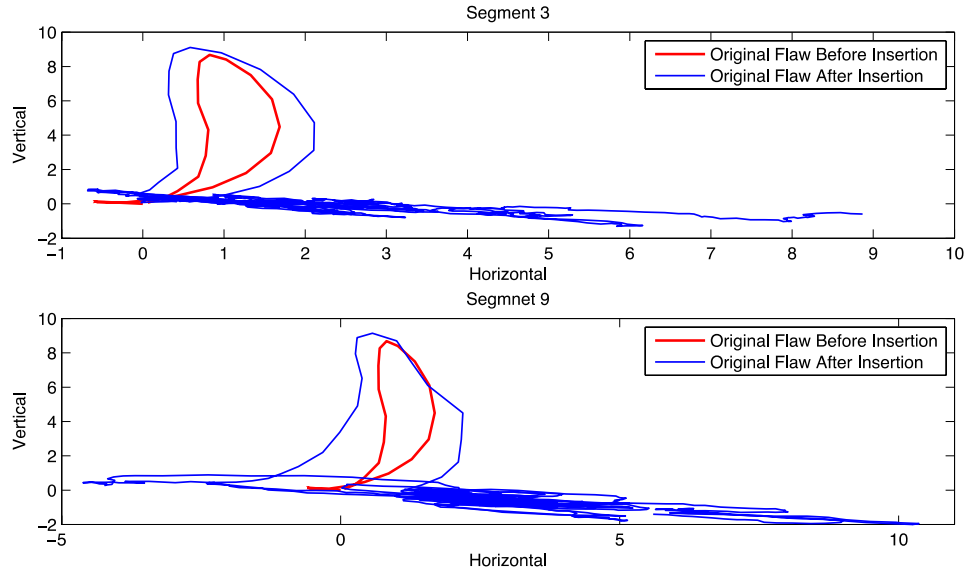


**Figure 6.14:** The inserted flaw in Segment 3 (top) and Segment 9 (bottom) along with the original flaw before insertion

Figure 6.15 shows the impedance plane plots of Segments 3 and 9 before (in blue) and after (in red) applying the proposed algorithm.

Generally, the flaw signal, which has been distorted due to insertion, should regain its original shape and size after applying a filter such as Iterative WMIpDFT. After the sinusoidal noise reduction, it can be observed from Figure 6.15 that the flaw signal has been improved, which will be discussed shortly, to represent the original shape of the flaw signal in Figure 6.13. The improvement was also observed in most of the segments with the inserted flaw. However, it is not clear how much the proposed algorithm has in anyway helped improving the distorted flaw signals in terms of phase and amplitude for characterization and classification. Therefore, it is difficult to draw conclusions based solely on the observations of the flaw signals before and after the noise reduction of the sinusoidal noise based on the available resources.

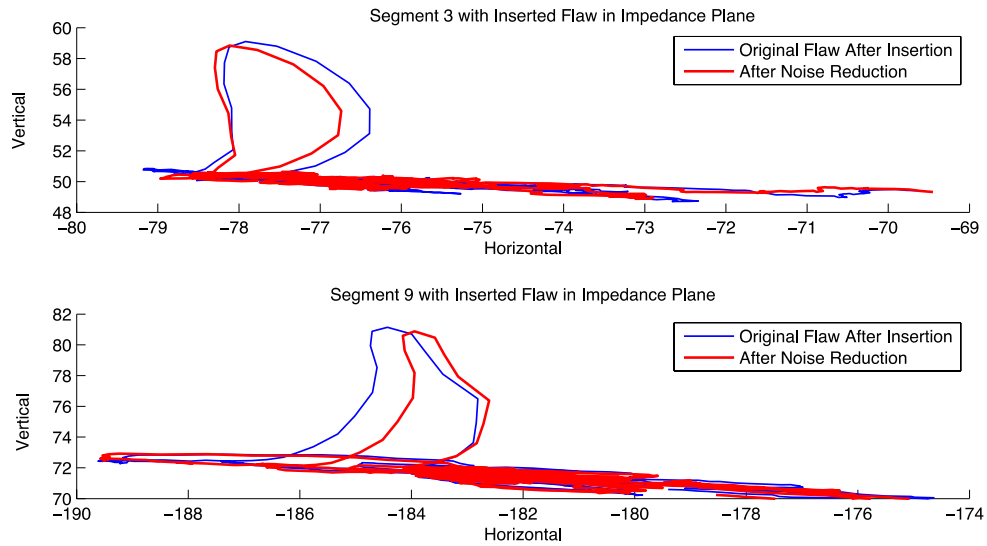


**Figure 6.15:** Plots of Impedance plane of Segments 3 and 9 before and after applying the proposed sinusoidal noise reduction algorithm

Nevertheless, one of the important aspects that can be analyzed in the impedance plane, and is visible in these impedance figures is the horizontal stretch noise which has been introduced into the flaw signals after insertion which can be observed in Figure 6.15. The horizontal stretch exists on the horizontal component, and is typically stemmed from lift-off or the presence of magnetite. Figure 6.16 shows the horizontal stretch that existed where the flaw was inserted in Segment 9. It can be seen how the horizontal stretch goes from -183 to -189, and back to the initial value for the duration of the signal. The vertical component also varies, but the variation is different from the horizontal component, which causes the signal to get distorted.

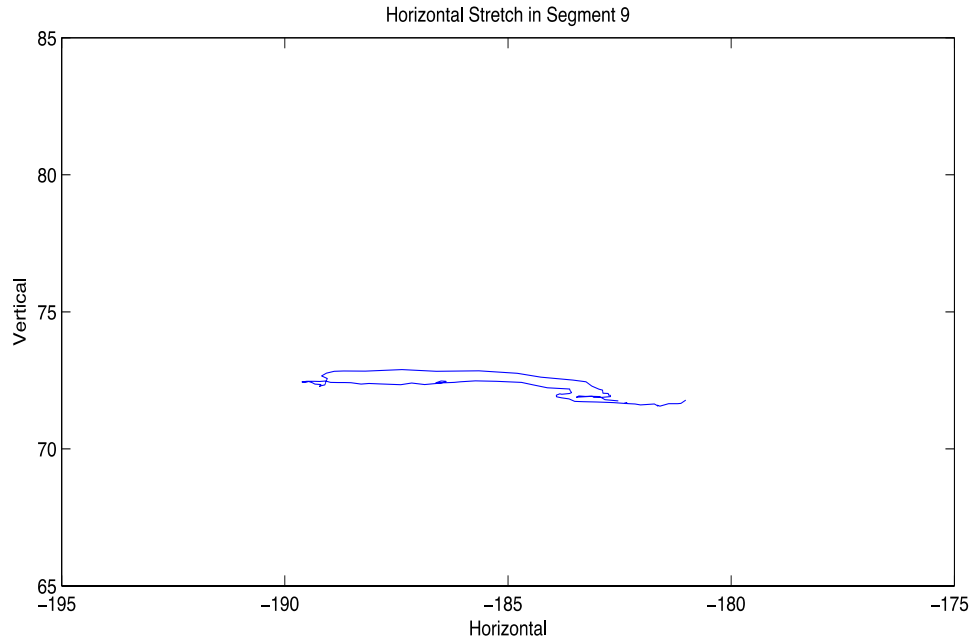


**Figure 6.16:** Horizontal Stretch in Segment 9 which introduces distortion in the flaw

Moreover, the horizontal stretch can lead to misdetection of flaws or inaccurate flaw characterization. Therefore, it is important to see if the sinusoidal noise reduction using the proposed algorithm has led to the reduction of the horizontal stretch.

From the plots in Figure 6.15 above, it is evident both of the flaws in Segments 3 and 9 have suffered from horizontal stretch which distorts the peak from its original shape. After applying the proposed algorithm, both of the segments can be observed to have their horizontal stretch minimized to closely match the original flaw.

The utilization of the proposed algorithm in the reduction of the horizontal stretch to represent its original shape more closely has also led to improvement or slight improvement in most other segments with the inserted flaws. However, in Segment 18, the noise reduction has increased the horizontal stretch in the flaw signal as shown in Figure 6.17.

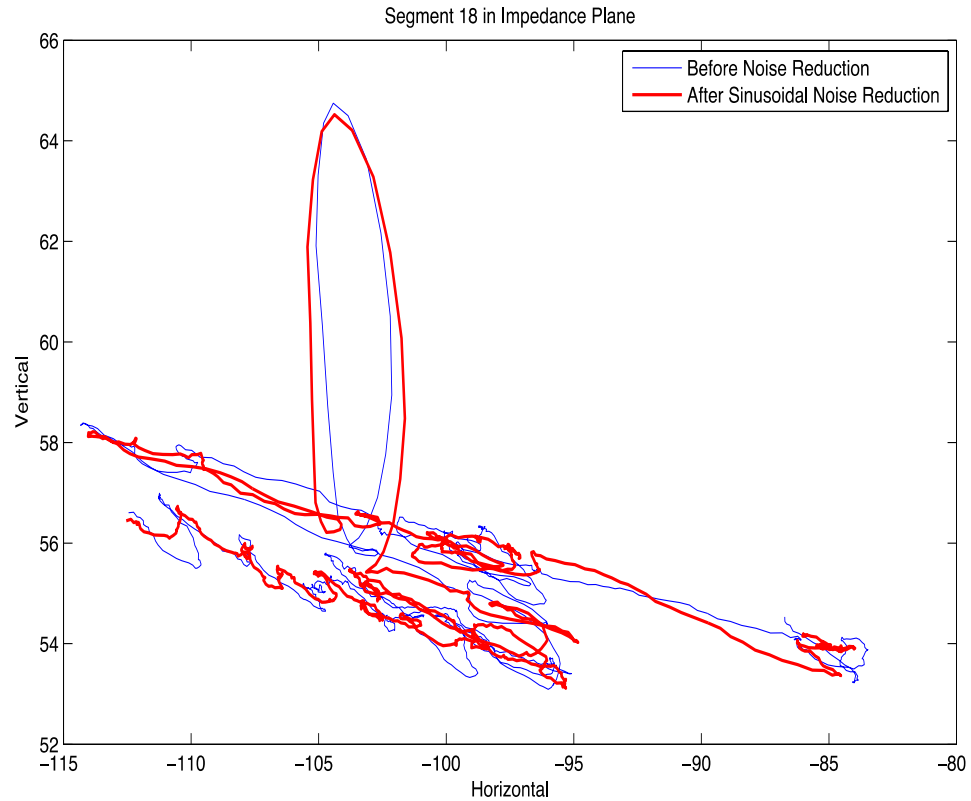


**Figure 6.17:** Plot of Impedance plane of Segments 18 before (in blue) and after (in red) applying the proposed sinusoidal noise reduction algorithm

Due to the increase in the horizontal stretch in Segment 18, another option was investigated to see if it could potentially be integrated into the proposed algorithm to minimize the stretch, and improve the flaw signal.

One of the techniques, which are used to improve the horizontal stretch, is to invert the phase of the horizontal noise component to match the vertical noise component. Figure 6.18 shows the phases for the vertical and horizontal noise component of the flaw signal in Segment 18.

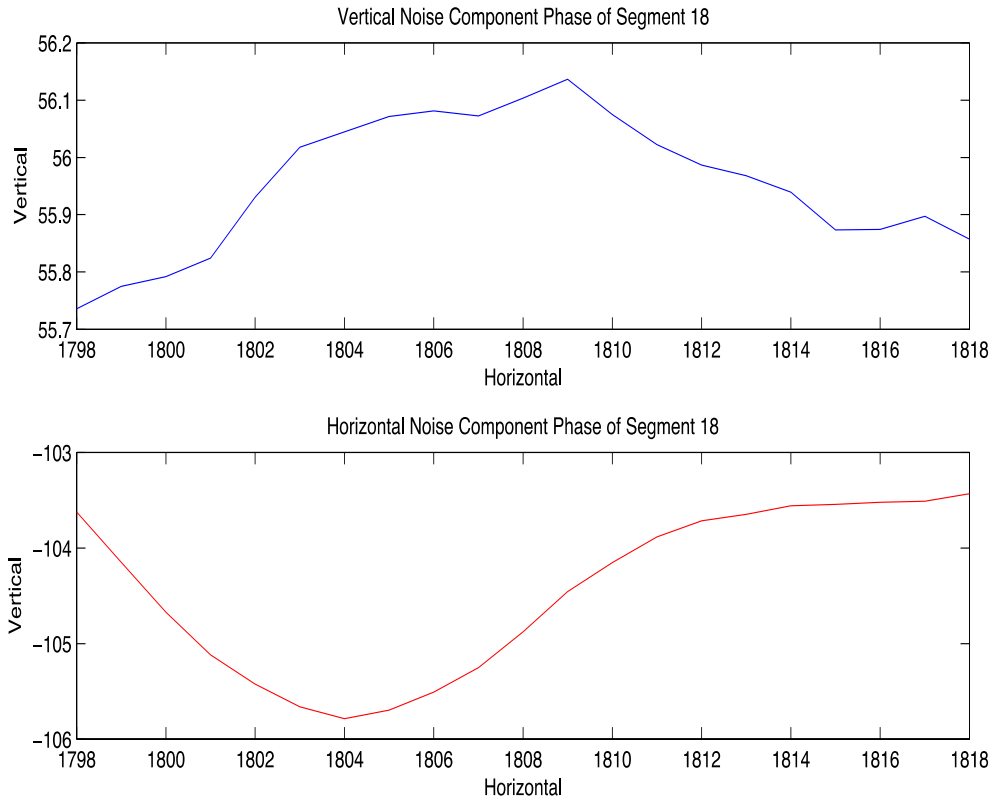


**Figure 6.18:** Phase of vertical and horizontal components of Segment 18

As it can be seen in Figure 6.18 that the phase of the two components are out of phase, and by inverting the horizontal component, they can be matched. After subtracting the flaw from the noise to invert the phase of the horizontal component, the shape of the inserted flaw in Segment 18 has much improved to represent the original flaw signal. This is evident in Figure 6.19, which shows the flaw signal after the phase inversion along with the flaw signal after insertion. The horizontal stretch has notably reduced after the phase inversion compared to the flaw after insertion.

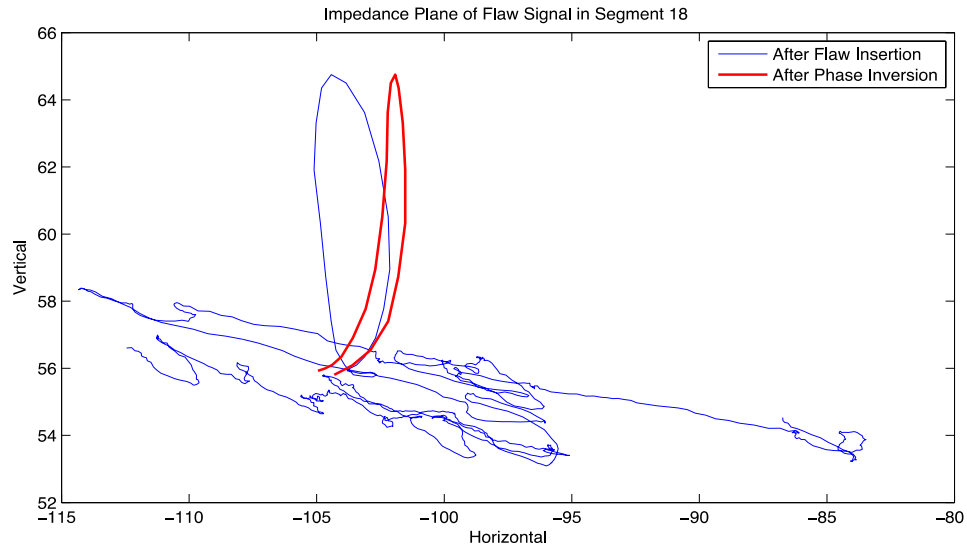


**Figure 6.19:** The impedance plane of Segment 8 after insertion the flaw in blue, and after phase inversion in red

The phase inversion perfectly works for Segment 18 even before applying the proposed algorithm. However, this was not seen, for instance, in Segment 3, where the phase inversion introduced more distortion in the flaw, and deviated the flaw from the original shape, which can be seen in Figure 6.20. Comparing the flaw in Segment 3 after the phase inversion with the original flaw in Figure 6.13 and the flaw after the sinusoidal noise reduction 6.15, it can be observed that the flaw has significantly been distorted.

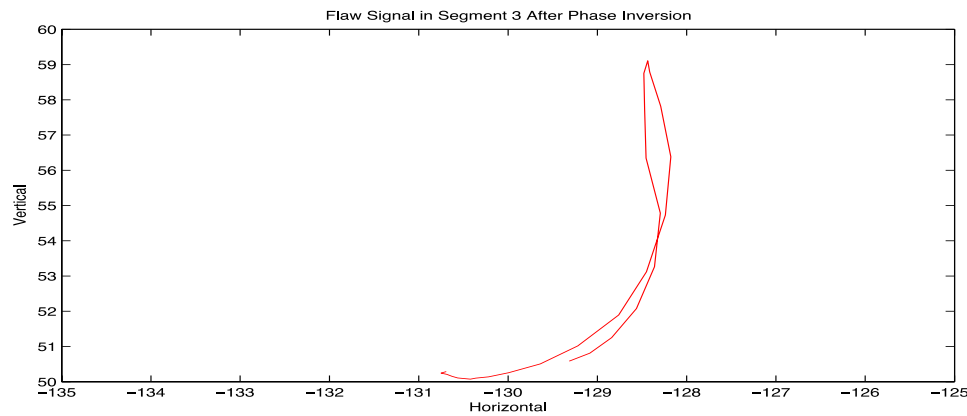


**Figure 6.20:** Impedance plane of the inserted flaw in Segment 3 after phase inversion

Nonetheless, the idea of using a similar technique to match the phases of the vertical and horizontal components was explored, especially for Segment 18, in order to check the possibility of reducing the horizontal stretch to regain the original shape of the inserted flaw signal after applying the Iterative WMIpDFT algorithm.

After applying the proposed algorithm, it was understood that the phase of the two components are less out of phase as shown in Figure 6.21 as opposed to Figure 6.18 which were completely out of phase. The phases of the components being less out of phase should have contributed, in the first place, to less distortion in the flaw signal for Segment 18 after filtering the data using the proposed algorithm. Conversely, this was not concluded from Figure 6.17.

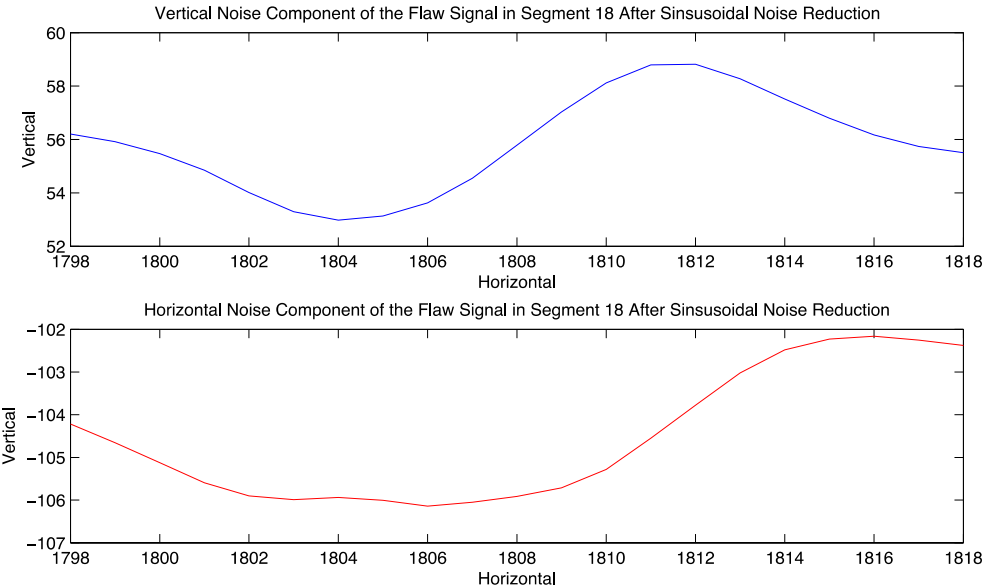


**Figure 6.21:** The phase of two components after sinusoidal noise reduction for Seg18

Moreover, attempts were made to shift the phases of the vertical and horizontal components to match one another after applying the sinusoidal noise. However, the matching

of the phases of the two components after applying the algorithm did not reduce the horizontal stretch in Segment 18, and it introduced further horizontal stretch. Therefore, matching the phase of the two horizontal and vertical components did not help improving the flaw signal after the sinusoidal noise reduction for Segment 18.

It has been shown that the proposed algorithm has improved the flaw signal in term of horizontal noise and regaining the shape of the original signal in most of the flaw signals in Tube 1. However, as a future study, it is important to further investigate to see if the proposed algorithm can be changed to help reducing horizontal noise in the flaws that have been affected due to this noise.

## **6.6 Comparison with Cyclic-MUSIC Algorithm**

In this section, the algorithm developed in this study is compared to the Cyclic-MUSIC algorithm in [3] in the time domain. The improvements made by the Iterative WMIpDFT algorithm are discussed with respect to the Cyclic-MUSIC algorithm.

In terms of frequency estimation, by looking at Segment 17 where there is a potential flaw peak, it can be seen that the frequencies estimated by the Cyclic-MUSIC algorithm does not include one of the similar frequencies in the range of 21 Hz that exist in all other segments in the same tube (i.e. Tube 1). However, when the peak is removed the frequency appears in the estimation. In the case of the Iterative WMIpDFT algorithm, the similar frequency appears without removing the peak, but the estimation can be improved by peak removal. Table 6.17 shows the comparison of the two sinusoidal estimation methods for Segment 17 without removing the peak.

**Table 6.17:** Frequency component comparison of the two sinusoidal estimation technique in case of non-periodic peaks. It can be seen that the proposed algorithm estimate frequencies such as 21.9 and 7.51 that have been similarly observed in other segments without removing peak in the segment

<i>Segment</i>	<i>Algorithm</i>	<i>Estimated Frequencies (Hz)</i>			
		<b>F1</b>	<b>F2</b>	<b>F3</b>	<b>F4</b>
<b>17</b>	<b>Cyclic-MUSIC</b>	7.69	16.82	13.43	0.08
	<b>Iterative WMIpDFT</b>	21.90	17.14	14.23	7.51

In terms of root mean square (RMS) of the data after removing the estimated sinusoidal noise of 4 sinusoids, the Iterative WMIpDFT leads to far better results than the Cyclic-MUSIC algorithm. That shows that Iterative WMIpDFT estimates sinusoidal parameters (i.e. frequency, amplitude and phase) more accurately, which in turn can improve the detection of flaw signals.

Moreover, the Cyclic-MUSIC algorithm, in some cases, leads to higher RMS, after subtraction of the sinusoidal noise, than the original eddy current data. This means that the reduction of the estimated sinusoidal noise distorts and adds more noise to the data. The following Table 6.18 contains the RMS results of the data with sinusoidal noise reduced for both of the algorithms. The estimated parameters of four sinusoids by the Cyclic-MUSIC algorithm are obtained from [3]. In both techniques, the sinusoids are estimated without removing non-periodic peaks that exist in some segments.

Table 6.18 clearly shows that Iterative WMIpDFT algorithm yields better RMS values in all the segments compared to the Cyclic-MUSIC algorithm.

**Table 6.18:** RMS comparison of Cyclic-MUSIC and Iterative WMIpDFT algorithms. The proposed algorithm in Column 4 shows lower RMS values based on estimated noise of 4 sinusoids

Segment	Original Data	RMS of Sinusoidal noise subtracted data	
		Cyclic-MUSIC Algorithm	Iterative WMIpDFT
<b>1</b>	0.3261	0.308	0.199
<b>2</b>	0.4846	0.4851	0.3683
<b>3</b>	0.2474	0.2342	0.1166
<b>4</b>	0.272	0.2882	0.1343
<b>5</b>	0.2945	0.2811	0.1418
<b>6</b>	0.4892	0.5138	0.3235
<b>7</b>	0.3386	0.3763	0.2352
<b>8</b>	0.2449	0.2358	0.1915
<b>9</b>	0.3402	0.3348	0.263
<b>10</b>	0.3665	0.4058	0.231
<b>11</b>	0.3658	0.3871	0.2233
<b>12</b>	0.3028	0.282	0.2072
<b>13</b>	0.3613	0.3079	0.2365
<b>14</b>	0.384	0.3837	0.2171
<b>15</b>	0.3228	0.3128	0.2321
<b>16</b>	0.3791	0.4075	0.3214
<b>17</b>	0.5439	0.5989	0.5531
<b>18</b>	0.535	0.654	0.3742

In terms of consistency between frequency estimation of different number of sinusoids, there is inconsistency in the Cyclic-MUSIC algorithm because of lacking an accurate model order. This means that, in almost all the segments, frequency estimations for 2 sinusoids are different than of those for 4 sinusoids. However, the Iterative WMIpDFT algorithm results in consistent frequency estimations regardless of the number of sinusoids. The inconsistency for selected segments in the case of the Cyclic-MUSIC algorithm.

## Chapter 7: Conclusion and Future Work

In this chapter, a conclusion has been provided along with a suggestion for future work in this project.

### 7.1 Conclusion

In this research, the details of the proposed algorithm, Iterative WMIpDFT, to accurately estimate the deterministic low frequency sinusoidal noise from the SG tubes ECT data provided by CNL, located in a CANDU nuclear plant, are discussed. Compared to most windowed interpolated DFT methods, WMIpDFT uses more than two interpolation points for improvement in the accuracy of parameter estimates. This technique also utilizes Rife-Vincent windows (generalization of the Hanning window), which helps reduce the spectral interference caused by frequency components. The higher number of interpolation points leads to reduction of systematic errors, which in turn improves parameter estimation.

In addition, it has been shown that the best estimated sinusoidal noise signals are acquired by WMIpDFT when a window order  $H$  of 2, which represents a Hanning window, and an interpolation point variable  $J$  of 1 (i.e. 3 interpolation points) are used.

The algorithm first was applied to the simulated data to estimate the parameters of the inserted sinusoidal waveforms. It was shown that the proposed algorithm leads to very small differences in terms of RMSE between the estimated and actual parameter values.

Furthermore, the proposed algorithm was applied to the vertical component to estimate low frequency sinusoidal noise, where most of the flaws exist, of the ECT data in the FS regions, which are located between the TSPs. It was shown, in the time domain, that the iterative and minimization components of the proposed algorithm as well as non-periodic peak

removal led to better estimation of sinusoidal noise parameter based on reduction in RMS. It was also shown averaging of estimated frequencies in each region (i.e. cold, hot or u-bend) could potentially improve the RMS.

Moreover, it was concluded that the proposed algorithm improved the PAR of the flaws, which could potentially facilitate the detection of flaws. It was also shown that the PAR for the flaws decreased as the number of estimated sinusoids of the noise signal increased even though the RMS improved.

In this research, the proposed algorithm was applied to the segments with the inserted 40% OD flaws to study the effect of this algorithm in the presence of actual flaws in the time domain as well as the impedance plane. It was again observed that the reduction of the estimated sinusoidal noise from both the vertical and horizontal components led to better RMS value and PAR in the segments with the inserted flaws in the time domain.

At the end of the research, the Iterative WMIpDFT algorithm was compared to the Cyclic-MUSIC algorithm proposed in [3] whose application is to estimate the sinusoidal noise from the same set of eddy current testing (ECT) data. It was shown that the Iterative WMIpDFT algorithm performs well when data contains non-periodic peaks. Also, it was concluded that, the estimated parameters of the sinusoidal noise by the Iterative WMIpDFT algorithm led to lower RMS compared to the Cyclic-MUSIC algorithm when the estimated sinusoidal noise signal was subtracted from the ECT data of the test tube. This potentially means that WMIpDFT leads to higher enhancement of flaw detection.

Moreover, the flaw, which suffered from horizontal stretch in the impedance plane after insertion, had its horizontal stretch reduced after applying the proposed algorithm in most of the segments by visually comparing the flaws after the insertion, and after applying

the algorithm. However, the horizontal noise in one of the segments was further stretched after applying the proposed algorithm. Therefore, it was attempted to incorporate a technique such as phase inversion into the algorithm to reduce the horizontal stretch in that particular segment by matching the phases of the vertical and horizontal components. It was seen that before applying the proposed algorithm, the phase matching of the two components notably reduced the horizontal stretch, but after applying the algorithm, the phase matching expanded the horizontal stretch.

In overall, the Iterative WMIpDFT algorithm developed in this research has produced promising results in term of estimating and reducing sinusoidal noise from the collected ECT data in the FS regions of the SG tubes.

## **7.2 Future Work**

In this study, the utilization of the proposed algorithm on the TSP regions was not explored. The TSP region is of high importance since many flaws such as cracks, thinning and fretting wear can be found in the region due to interaction between the tube and TSPs, and other factors. Therefore, reducing sinusoidal noise in this region helps the enhancement of flaw signals, and improves the detection of them.

In addition, the proposed algorithm's efficiency was mostly discussed in the time domain, and therefore, it is vital to extensively study the effect of the proposed algorithm on the flaws in the impedance plane in terms of phase and amplitude change. The phase and amplitude changes can greatly affect the characterization and classification of flaws in the impedance plane.

Furthermore, the issue of horizontal stretch noise, which could cause misdetection of flaws in the impedance plane, was briefly discussed after applying the proposed algorithm. An

attempt was made to reduce this noise in the segments, where the noise was further increased using the proposed algorithm, by applying known techniques such as matching the phases of the vertical and horizontal components of ECT data. However, this did not result in reducing the horizontal stretch noise. Therefore, the horizontal noise needs to be further investigated to see how tweaking the proposed algorithm can reduce it.

## Appendix A

### A.1 Estimated Sinusoidal Noise Parameters of Other Tubes

Estimated sinusoidal noise of Tube 2 for 2 sinusoids using Iterative WMIPDFT with RMS improvement after the subtraction of the estimated sinusoidal noise from the ECT data.

Region	Segment	Frequency (Hz)		Amplitude (V)		Phase (Radian)		RMS Improvement in Percentage
		F1	F2	A1	A2	P1	P2	
Cold	1	18.985	7.184	0.075	0.099	1.171	-3.349	8.46%
	2	19.114	7.058	0.108	0.053	-0.811	-0.419	17.47%
	3	19.076	8.973	0.097	0.042	1.740	-0.189	20.31%
	4	19.020	7.167	0.108	0.049	-0.353	2.040	30.11%
	5	19.821	8.928	0.082	0.149	0.018	-2.594	6.04%
	6	18.999	8.253	0.114	0.054	0.623	-2.143	17.33%
	7	19.203	7.874	0.033	0.048	-3.142	-0.742	5.26%
U-Bend	8	19.045	6.547	0.106	0.183	1.807	3.079	15.11%
	9	19.217	8.174	0.140	0.152	0.194	-0.058	9.29%
	10	18.839	9.143	0.136	0.016	0.161	1.162	4.12%
	11	19.326	0.000	0.087	0.000	1.713	0.000	7.82%
Hot	12	18.886	7.332	0.099	0.053	-2.905	1.805	25.19%
	13	18.762	6.960	0.099	0.049	-0.519	-0.012	18.39%
	14	18.787	8.678	0.096	0.060	1.299	3.205	14.88%
	15	18.848	9.020	0.114	0.010	-2.670	-2.872	19.71%
	16	19.107	7.325	0.104	0.070	0.092	-2.333	12.68%
	17	18.841	7.803	0.096	0.096	-1.480	0.483	17.80%
	18	18.689	7.986	0.053	0.135	-1.535	-3.182	5.07%

Estimated sinusoidal noise of Tube 3 for 2 sinusoids using Iterative WMIPDFT with RMS improvement after the subtraction of the estimated sinusoidal noise from the ECT data.

Region	Segment	Frequency (Hz)		Amplitude (V)		Phase (Radian)		RMS Improvement in Percentage
		F1	F2	A1	A2	P1	P2	
Cold	1	19.978	8.072	0.037	0.109	-2.214	3.416	6.55%
	2	19.618	8.274	0.146	0.074	-0.100	-1.982	13.31%
	3	19.691	8.077	0.154	0.037	-1.264	2.050	37.27%
	4	19.249	7.994	0.175	0.096	-2.085	2.945	24.05%
	5	19.656	0.000	0.111	0.000	2.660	0.000	4.33%
	6	20.007	8.053	0.110	0.105	-0.955	2.515	12.75%
	7	19.249	7.781	0.125	0.053	1.011	0.950	33.44%
U-Bend	8	19.181	9.182	0.114	0.032	1.285	-2.108	15.58%
	9	19.462	8.423	0.140	0.065	1.650	-3.772	6.89%
	10	19.731	7.890	0.130	0.080	3.782	5.414	8.53%
	11	19.714	6.997	0.126	0.149	3.991	1.696	19.22%
Hot	12	19.306	7.463	0.121	0.078	-4.026	-3.186	28.99%
	13	19.318	8.076	0.139	0.070	1.423	-1.869	25.87%
	14	19.527	7.026	0.090	0.149	0.223	-0.174	19.85%
	15	19.102	6.991	0.098	0.059	-0.853	3.920	15.48%
	16	19.166	8.545	0.101	0.019	-1.834	1.203	29.93%
	17	19.136	8.889	0.081	0.088	-3.116	1.718	11.20%
	18	17.831	8.859	0.094	0.132	-0.195	1.479	3.67%

Estimated sinusoidal noise of Tube 4 for 2 sinusoids using Iterative WMIPDFT with RMS improvement after the subtraction of the estimated sinusoidal noise from the ECT data.

Region	Segment	Frequency (Hz)		Amplitude (V)		Phase (Radian)		RMS Improvement in Percentage
		F1	F2	A1	A2	P1	P2	
Cold	1	17.960	6.677	0.030	0.054	-0.341	-0.785	2.63%
	2	19.781	8.084	0.082	0.070	0.646	0.188	10.39%
	3	19.631	7.943	0.109	0.080	3.262	-1.538	26.79%
	4	20.093	7.198	0.113	0.103	-0.348	-3.272	15.69%
	5	19.574	7.912	0.105	0.093	4.352	-1.278	14.32%
	6	19.634	8.148	0.089	0.037	2.152	-3.425	9.26%
	7	19.808	8.022	0.095	0.080	-0.783	1.367	15.40%
U-Bend	8	19.906	7.864	0.104	0.058	0.427	2.663	8.17%
	9	19.711	8.670	0.131	0.180	-2.028	3.975	8.38%
	10	19.204	8.360	0.043	0.096	2.857	-1.594	1.87%
	11	19.709	6.889	0.057	0.041	1.139	-0.393	2.95%
Hot	12	19.345	7.070	0.048	0.046	-0.744	0.216	8.42%
	13	19.969	8.789	0.039	0.036	2.901	0.610	5.89%
	14	20.056	8.210	0.034	0.062	-0.480	-1.095	7.02%
	15	0.000	7.132	0.000	0.079	0.000	3.122	2.15%
	16	19.709	8.125	0.069	0.068	2.417	-0.671	8.88%
	17	18.036	7.133	0.088	0.188	1.450	-0.961	5.22%
	18	19.962	8.759	0.110	0.074	1.814	-3.481	7.61%

Estimated sinusoidal noise of Tube 5 for 2 sinusoids using Iterative WMIPDFT with RMS improvement after the subtraction of the estimated sinusoidal noise from the ECT data.

Region	Segment	Frequency (Hz)		Amplitude (V)		Phase (Radian)		RMS Improvement in Percentage
		F1	F2	A1	A2	P1	P2	
Cold	1	19.378	9.352	0.169	0.027	-3.583	-2.790	11.21%
	2	19.353	7.221	0.203	0.073	-0.790	-1.507	18.61%
	3	19.302	7.929	0.153	0.073	-0.078	1.271	24.89%
	4	19.340	8.061	0.112	0.063	0.857	0.824	17.31%
	5	19.770	7.031	0.056	0.163	0.691	-2.263	9.08%
	6	19.293	7.978	0.097	0.088	-3.795	-1.117	22.44%
	7	19.373	8.025	0.078	0.066	-3.040	-1.910	11.96%
U-Bend	8	18.753	7.969	0.081	0.138	2.860	-2.199	4.14%
	9	21.316	9.029	0.032	0.053	1.238	0.426	0.46%
	10	0.000	7.930	0.000	0.047	0.000	-0.583	0.26%
	11	19.235	7.138	0.062	0.046	-1.243	1.116	0.92%
Hot	12	19.266	8.878	0.130	0.038	-2.158	-1.170	14.74%
	13	19.218	9.779	0.091	0.005	-0.675	3.371	5.56%
	14	19.208	7.912	0.186	0.036	-2.937	-2.526	38.61%
	15	19.074	7.709	0.185	0.102	-2.288	3.960	43.53%
	16	19.254	7.179	0.207	0.066	-3.038	-2.739	41.45%
	17	19.234	8.049	0.204	0.078	-2.242	-0.287	16.67%
	18	20.861	8.102	0.431	0.463	0.639	2.194	8.96%

## Bibliography

- [1] R. Lakhan and B. Lepine, "Advanced Processing of NDE Data for System Condition Monitoring and Assessment" presented at Carleton University Campus, Ottawa, Canada, 2011.
- [2] R. Lakhan, "Advanced Processing of NDE Data for System Condition Monitoring and Assessment" presented at Carleton University Campus, Ottawa, Canada, 2012.
- [3] H. Chahrour , "Sinusoidal Parameter Estimation and Application to Eddy Current NDT Data Records," Systems and Computer Engineering Department, Carleton University, Ottawa, Master of Applied Science (M.A.Sc.). thesis 2014.
- [4] Wm. J. Garland, Ed., *The Essential CANDU, A Textbook on the CANDU Nuclear Power Plant Technology*, University Network of Excellence in Nuclear Engineering (UNENE), ISBN 0-9730040. Retrieved from <https://www.unene.ca/education/candu-textbook> on June 1st, 2016
- [5] R.L. Tapping, Y.C. Lu, D.S. Mancey, and Z.H. Walker, "Assessing Long-Term Performance of CANDU® Out-of-Core Materials," *CNL Nuclear Review*, vol. 1, no. 1, pp. 5-11, June 2012.
- [6] R.L. Tapping, J. Nickerson, P. Spekkens, and C. Maruska, "CANDU Steam Generator Life Management," *Nuclear Engineering Design*, vol. 197, no. 1-2, pp. 213–223, March 2000.
- [7] A. L. Formigoni, L. A. N. M. Lopez, and D. K. S. Ting, "Diagnostic of Corrosion Defects in Steam Generator Tubes Using Advanced Signal Processing from Eddy Current Testing," in *International Nuclear Atlantic Conference*, Rio de Janeiro, 2009.
- [8] L. S. Rosado, P. M. Ramos, and M. Piedade, "Real-Time Processing of Multifrequency Eddy Currents Testing Signals: Design, Implementation, and Evaluation," *IEEE Transactions on Instrumentation and Measurement*, vol. 63, no. 5, May 2014.
- [9] P. J. Shull, *Nondestructive Evaluation: Theory, Techniques, and Applications*. Altoona, Pennsylvania, US: Marcel Dekker, Inc., 2002.
- [10] T. Takagi, H. Huang, H. Fukutomi , and J. Tani, "Numerical Evaluation of Correlation between Crack Size and Eddy Current Testing Signal by a Very Fast Simulator," *IEEE Transactions on Magnetics*, vol. 34, no. 5, September 1998.
- [11] V.N. Mittle and A. Mittal, *Basic Electrical Engineering*. Tata McGraw-Hill Education Pvt. Ltd., 2005.

- [12] J. Garcia-Martin, J. Gomez-Gill, and E. Vazquez-Sanchez, "Non-Destructive Techniques Based on Eddy Current Testing," *Sensors – Open Access Journal*, pp. 2525-2565, February 2011.
- [13] T. Stepinski, "Essential Parameters in Eddy Current Inspection," Dept. Signals and Systems, Uppsala University, Uppsala, Sweden, May 2000.
- [14] D. Jiles, *Introduction to the Principles of Materials Evaluation*. Cardiff, UK: Taylor and Francis Group, 2007.
- [15] G.Y. Tian, Z.X. Zhao, and R.W. Baines, "The research of inhomogeneity in eddy current sensors," *Sensors and Actuators A: Physical*, vol. 69, no. 2, pp. 148-151, August 1998.
- [16] Canadian General Standards Board, *Advanced Manual for : Eddy Current Test Method*, 1997.
- [17] B. Raj, T. Jayakumar, and M. Thavasimuthu, *Practical Non-destructive Testing*, 2nd ed. Kalpakkam, India: Woodhead Publishing, 2002.
- [18] J. Hansen, "The eddy current inspection method: Part 1. History and electrical theory," *OR Insight*, vol. 46, no. 5, pp. 279-281, April 2004.
- [19] K. Thulukkanam, *Heat Exchanger Design Handbook*, 2nd ed. Boca Raton, US: CRC Press, 2013.
- [20] L. Udpa, P. Ramuhalli, J. Benson, and S. Udpa, "Automated Analysis of Eddy Current Signals in Steam Generator Tube Inspection," in *Proceedings of the 16th WCNDT 2004 World Conference on NDT*, Montreal, December 2004.
- [21] A. Fahr, *Aeronautical Applications of Non-destructive Testing*. Lancaster, Pennsylvania, USA: DEStech Publications Inc., 2014.
- [22] R. Lakhan, "Bobbin Probe Data: Introduction" presented at Carleton University Campus, Ottawa, Canada, 2013.
- [23] S. Bakhtiari, D. S. Kupperman, and W.J. Shack. (2009, March) Assessment of noise level for eddy current inspection of steam generator tubes.
- [24] D. H. Hur, M. S. Choi , H. Shim, and O. Yoo, "Influence of signal-to-noise ratio on eddy current signals of cracks in steam generator tubes," *Nuclear Engineering and Technology*, vol. 46, no. 6, pp. 883-888, November 2014.

- [25] "Automated Analysis of Bobbin Coil Probe Eddy Current Data," Electric Power Research Institute (EPRI), Palo Alto, CA, 1002785, 2000.
- [26] M. Das , P. Ramuhalli , L. Udpa , and S. Udpa, "An Adaptive Wiener Filter Based Technique for Automated Detection of Defect Locations from Bobbin Coil Eddy Current Data," in *AIP Conference Proceedings*, vol. 615, Brunswick, 2002, pp. 639-646.
- [27] G. Chen, A. Yamaguchi , and K. Miya, "A Novel Signal Processing Technique for Eddy-Current Testing of Steam Generator Tubes," *IEEE Transactions on Magnetics*, vol. 34, no. 3, pp. 642-648, May 1998.
- [28] L.A.N.M. Lopez , D.K.S. Ting, and B.R. Upadhyaya, "Removing Eddy Current Probe Wobble Noise from Steam Generator Tubes Testing Using Wavelet Transform," *Progress in Nuclear Energy*, vol. 50, no. 7, pp. 828-835, September 2008.
- [29] V.K. Jain, W. L. Collins, and D. C. Davis, "High-Accuracy Analog Measurements via Interpolated FFT," *IEEE Transactions on Instrumentation and Measurement*, vol. IM-28, no. 2, 1979.
- [30] T. Grandke, "Interpolation Algorithms for Discrete Fourier Transforms of Weighted Signals," *IEEE Trans. Instrumentation and Measurement*, vol. 32, no. 2, pp. 350–355, 1983.
- [31] D. Belega and D. Dallet, "Choice of the Acquisition Parameters for Frequency Estimation of a Sine Wave by Interpolated DFT Method," *Computer Standards Interfaces*, vol. 31, no. 5, pp. 962–968, Sep. 2009.
- [32] D. Belega and D. Dallet, "Multipoint Interpolated DFT Method for Frequency Estimation," in *6<sup>th</sup> International Multi-Conference on Systems, Signals and Devices*, 2009.
- [33] D. Belega and D. Dallet, "Frequency Estimation via Weighted Multipoint Interpolated DFT," *IET Sci. Meas. Technol.*, pp. 1–8, 2008.
- [34] D. Agrez, "Weighted Multipoint Interpolated DFT to Improve Amplitude Estimation of Multifrequency Signal," *IEEE Transactions on Instrumentation and Measurement*, vol. 5, no. 2, pp. 287-292, April 2002.
- [35] D. Belega and D. Dallet, "Amplitude Estimation by a Multipoint Interpolated DFT Approach," *IEEE Transactions on Instrumentation Measurement*, vol. 58, no. 5, pp. 1316–1323, 2009.
- [36] D. Belega and D. Dallet, "Multi-frequency Signal Analysis by Interpolated DFT Method with Maximum Side-lobe Decay Windows," *Journal of the International Measurement Confederation*, vol. 42, no. 3, pp. 420–426, Apr. 2009.

- [37] D. Belega, D. Dallet, and D. Petri, "Accuracy of Sine Wave Frequency Estimation by Multipoint Interpolated DFT Approach," *IEEE Transactions on Instrumentation and Measurement*, vol. 59, no. 11, pp. 2808–2815, 2010.
- [38] D. Belega, D. Dallet, and D. Petri, "Uncertainty Analysis of the Normalized Frequency Estimation by Multipoint Interpolated DFT Approach," in *Proceedings of the IEEE Workshop on Advanced Methods for Uncertainty Estimation Measurement (AMUEM)*, 2009, pp. 6–7.
- [39] D. Belega, D. Dallet, and D. Stoiciu, "Choice of the Window Used in the Interpolated Discrete Fourier Transform Method," *Revue Roumaine des Sciences Techniques, Serie Electrotechnique et Energetique*, vol. 54, no. 4, pp. 365–374, 2009.
- [40] R. Lakhan, "Noise Investigation" presented at Carleton University Campus, Ottawa, Canada, 2013.